Technische Universität München

Fakultät für Medizin

Klinik und Poliklinik für Vaskuläre und Endovaskuläre Chirurgie

Klinikum rechts der Isar der Technischen Universität München

(Prof. Dr. Hans-Henning Eckstein)

Multiscale Imaging Approaches to Target Atherosclerosis

Almut Elisabeth Glinzer

Vollständiger Abdruck der von der Fakultät für Medizin der Technischen Universität München zur Erlangung des akademischen Grades eines

Doktors der Naturwissenschaften (Dr. rer. nat.)

genehmigten Dissertation.

Vorsitzender: Prof. Dr. Dr. Stefan Engelhardt

Prüfer der Dissertation:

1. Prof. Dr. Hans-Henning Eckstein
2. Prof. Dr. Hendrik Dietz
3. Prof. Dr. Michael Zimmer

Die Dissertation wurde am 29.03.2017 bei der Technischen Universität München eingereicht und durch die Fakultät für Medizin am 06.12.2017 angenommen.

Eidesstattliche Erklärung

Ich erkläre an Eides statt, dass ich die bei der promotionsführenden Einrichtung der Fakultät der Medizin der TUM zur Promotionsprüfung vorgelegte Arbeit mit dem Titel:

„Multiscale imaging approaches to target atherosclerosis"

in der Klinik und Poliklinik für Vaskuläre und Endovaskuläre Chirugie, Klinikum rechts der Isar der Technischen Universität München unter der Anleitung und Betreuung durch Prof. Dr. med. Hans-Henning Eckstein ohne sonstige Hilfe erstellt und bei der Abfassung nur die gemäß § 6 Abs. 6 und 7 Satz 2 angebotenen Hilfsmittel benutzt habe.

Ich habe keine Organisation eingeschaltet, die gegen Entgelt Betreuerinnen und Betreuer für die Anfertigung von Dissertationen sucht, oder die mir obliegenden Pflichten hinsichtlich der Prüfungsleistungen für mich ganz oder teilweise erledigt.

Ich habe die Dissertation in dieser oder ähnliche Form in keinem anderen Prüfungsverfahren als Prüfungsleitung vorgelegt.

Die Dissertation wurde an nachstehend aufgeführten Stellen auszugweise veröffentlicht:

> Targeting elastase for molecular imaging of early atherosclerotic lesions
>
> **Glinzer A**, Ma X, Prakash J, Kimm MA, Lohöfer F, Kosanke K, Pelisek J, Thon MP, Vorlova S, Heinze KG, Eckstein HH, Gee MW, Nitziachristos V, Zernecke A, Wildgruber M.
>
> Arterioscler Thromb Vasc Biol. 2017 Mar;37(3):525-533

Ich habe den angestrebten Doktorgrad noch nicht erworben und bin nicht in einem früheren Promotionsverfahren für den angestrebten Doktorgrad endgültig gescheitert.

Die öffentlich zugängliche Promotionsordnung der TUM ist mir bekannt, insbesondere habe ich die Bedeutung von § 28 (Nichtigkeit der Promotion) und § 29 (Entzug des Doktorgrades) zur Kenntnis genommen. Ich bin mir der Konsequenzen einer falschen Eidesstattlichen Erklärung bewusst.

Mit der Aufnahme meiner personenbezogenen Daten in die Alumni-Datei bei der TUM bin ich einverstanden.

Ort, Datum, Unterschrift

“Die Wissenschaft fängt eigentlich erst da an interessant zu werden, wo sie aufhört.”

Justus von Liebig – Chemische Briefe

I ABSTRACT

Atherosclerosis is an inflammatory disease of the vascular wall causing clinical sequelae such as myocardial infarction and stroke, the leading causes of death in the Western world. This work reveals new insights about the possibility how different imaging modalities can be used to gain a more dynamic understanding of atherosclerosis. To target biological activities in atherosclerotic plaques in vivo two different imaging approaches were performed, namely Fluorescence Molecular Tomography (FMT) combined with X-ray Computed Tomography (XCT) and Magnetic Resonance Imaging (MRI) with specific contrast agents, respectively. Furthermore, imaging data sets were applied to create a three-dimensional (3D) representation of the murine aortic arch based on reconstructed serial histological sections.

The first imaging approach aimed to target elastase, an effector molecule of neutrophils, in vivo and non-invasively during the course of early atherosclerosis using an elastase specific near infrared fluorescent imaging agent. This approach evidenced that FMT-XCT is suitable to detect elastase activity in early atherosclerotic lesion formation in an established mouse model. This imaging approach harbors potential to track specific aspects of pathophysiology of early atherosclerosis in experimental mouse models.

The second imaging approach employed a magnetic resonance contrast agent (Gadofluorine P) to target atherosclerotic plaque compositions based on amphiphilic interactions. Accumulation of the MRI agent was locally detected and quantified by matrix-assisted laser desorption/ionization imaging mass spectrometry after in vivo imaging. This validation tool is a promising application for spatially resolved quantification of MRI agents in atherosclerotic plaques.

Within the third approach a technical workflow was developed to create a 3D representation of the murine aortic arch based on reconstructed serial histological sections to visualize regions of plaque development and cellular composition. MR imaging followed by centerline calculation successfully supported 3D reconstruction similar to the original shape of the aortic arch, but showed limitations in regions of bifurcations. To consider preparation artifacts such as shrinkage and deformations the implementation of µCT was attempted.

In this work we successfully applied imaging modalities in the context of atherosclerosis. Each imaging approach provided additional benefit to enhance more insights into the pathobiology of atherosclerotic lesion development. The results of this work demonstrate the need of an interdisciplinary imaging approach of atherosclerosis in order to advance knowledge about this disease.

II ZUSAMMENFASSSUNG

Atherosklerose ist eine chronisch-entzündliche Gefäßerkrankung, die sich in Folgeerscheinungen wie Herzinfarkt und Schlaganfall manifestieren kann und somit für die häufigsten Todesursachen der westlichen Industrienationen verantwortlich ist.

In der vorliegenden Arbeit wurden verschiedene Bildgebungstechniken im Rahmen der Atherosklerose-Entstehung im Mausmodell angewendet. In den ersten beiden Teilen dieser Arbeit wurde die Fluoreszenz-Molekulartomographie (FMT) in Kombination mit der Computertomographie (CT) sowie die Magnet-Resonanz-Tomographie (MRT) mit jeweiligen Kontrastmitteln zur Darstellung biologischer Aktivitäten in atherosklerotischen Plaques genutzt. Außerdem wurden Bildgebungstechniken unterstützend eingesetzt, um ein Protokoll für eine dreidimensionale (3D) Rekonstruktion des Aortenbogens der Maus anhand von histologischen Schnittserien zu entwickeln.

Im ersten Teil dieser Arbeit wurde ein Kontrastmittel zur zielgerichteten Detektion der Elastase in einem Mausmodell der Atherosklerose untersucht. Neutrophile Granulozyten spielen in der Frühphase der Atheroskleroseentstehung eine wichtige Rolle und sezernieren dabei die Protease Elastase, welche mit dem Kontrastmittel detektiert werden kann. Mit einer Kombination von FMT und CT war es möglich, die Elastase in atherosklerotischen Plaques zu detektieren und somit frühe Stadien der Atherosklerose im Mausmodell zu visualisieren.

Im zweiten Teil der Arbeit wurde die Darstellung atherosklerotischer Plaques mittels MRT und Gadofluorine P, ein amphiphiles MRT-Kontrastmittel, im Mausmodell untersucht. Es wurde gezeigt, dass sich dieses in atherosklerotischen Plaques anreichert und somit zur MRT-gestützten Detektion genutzt werden kann. Außerdem war es möglich, das Kontrastmittel ex vivo mittels bildgebender Massenspektrometrie zu quantifizieren und ortsaufgelöst darzustellen.

In drittem Teil dieser Arbeit wurden Bildgebungstechniken unterstützend angewendet, um eine 3D Rekonstruktion des Aortenbogens der Maus anhand von histologischen Schnittserien möglich zu machen. Die Ausarbeitung des Protokolls zur 3D Rekonstruktion soll später zur räumlichen Darstellung atherosklerotischer Plaques sowie zellulärer Zusammensetzung genutzt werden. Durch die Einbindung der MRT-Technik in das Protokoll konnte eine sogenannte

Centerline aus dem Bildgebungsdatensatz berechnet werden. Die histologischen Bilder des Aortenbogens konnten anschließend auf diese Centerline adjustiert werden, wodurch eine 3D Rekonstruktion des Aortenbogens möglich war, mit Limitationen im Bereich der Gefäßabzweigungen. Außerdem wurde versucht, die Anwendung von µ-CT Messungen in das Protokoll zu integrieren, um Gewebe-Artefakte durch die histologische Aufarbeitung berücksichtigen zu können.

Die vorliegende Arbeit zeigt, dass verschiedene Bildgebungstechniken spezifische Einblicke in die Entwicklung und Beurteilung atherosklerotischer Plaques im Mausmodell ermöglichen. Durch den interdisziplinären Einsatz von Bildgebungstechniken kann das Wissen über die Atherosklerose-Entstehung erweitert werden.

III ABBREVIATIONS

Abbreviation	
2D	Two-dimensional
3D	Three-dimensional
APC	Allophycocyanin
APOE	Apolipoprotein E
$APOE^{-/-}$	Apolipoprotein E deficient
BSA	Bovine serum albumin
CCD	Charge-coupled device
CD	Cluster of differentiation
DAPI	4',6-diamidino-2-phenylindole
ECG	Electrocardiography
EvG	Elastica-van-Gieson
fMLP	N-Formyl-Met-Leu-Phe
FMT	Fluorescence molecular tomography
FMT-XCT	Fluorescence molecular tomography combined with X-ray computed tomography
FOV	Field of view
FSC	Forward side scatter
g	Gravity
Gd	Gadolinium
Gd-DTPA	Gadolinium-Diethylenetriaminepentacetate
h	Hours
H&E	Haematoxylin and eosin
HFD	High fat diet
IC_{50}	Half maximal inhibitory concentration
ICP-MS	Inductive coupled plasma mass spectrometry
IMS	Imaging mass spectrometry
kg	Kilogramm
kV	Kilovolt
LA-ICP-MS	Laser-ablation inductive coupled plasma mass spectrometry
LDL	Low density lipoprotein
LDLR	Low density lipoprotein receptor
$LDLR^{-/-}$	Low density lipoprotein receptor deficient
MALDI	Matrix-assisted-laser desorption/ionization
MALDI-IMS	Matrix-assisted-laser desorption/ionization combined with imaging mass spectrometry
min	Minutes
ml	Milliliter
mmol	Millimol
MMP	Matrix metalloprotease
MRI	Magnetic resonance imaging
ms	Milliseconds
mT/m	Millitesla/Meter
NE	Neutrophil Elastase
NET	Neutrophil extracellular trap
NIRF	Near-infrared fluorescence

nm	Nanometer
PBS	Phosphate buffered saline
PMA	Phorbol-12-myristate 13-acetate
R_1	Relaxation rate
r_1	Relaxivity
ROI	Region of interest
s	Seconds
SD	Standard deviation
SSC	Sideward scatter
T	Tesla
T1	Relaxation time
TE	Echo time
TOF	Time of flight
TR	Repetition time
TRIS	Tris(hydroxymethyl)-aminomethan
VCAM 1	Vascular cell adhesion molecule 1
XCT	X-ray computed tomography
µA	Microampere
µCT	Micro-Computed tomography
µl	Microliter
µM	Micromolar
µm	Micrometer

1 INTRODUCTION

1.1 Atherosclerosis

Cardiovascular disease is the most common cause of mortality in the industrialized world and represents 31% of all global deaths[1]. Atherosclerosis, the underlying cause of cardiovascular disease, is regarded as a chronic inflammatory disease of the arterial wall, manifesting in cardiovascular events such as myocardial infarction or stroke. Hyperlipidemia, hypertension and cigarette smoking are the most common risk factors of atherosclerosis[2, 3].

The word atherosclerosis derives from two Greek words: “Athero” (gruel) and “sclerosis” (hardness) and is a morphological description of atherosclerosis. The term was first introduced 1833 by Jean Lobstein[4]. Behind this description a complex pathophysiological process is hidden, which has been investigated and analyzed over the last century up to now. In the middle of the 19th century Rudolf Virchow and Carl von Rotikansky proposed converse aspects of plaque formation in humans. Both, Rotikansky and Virchow, postulated cellular inflammatory changes in the vessel wall as a reason of atherosclerosis. But Virchow considered them as primary and Rotikansky as secondary in nature[4]. Rotikansky assumed a primary injury of the endothelium caused through trauma. At the beginning of the 20th century Nikolaj N. Anitschkow elucidated the role of cholesterol in the pathogenesis of atherosclerosis[5]. In the 1970s Russel Ross refined Rotikansky’s view and postulated the “response to injury” hypothesis. Damage due to e.g. mechanical injury to the vessel wall initiates the development of atherosclerosis[6-8]. Additionally, Steinberg et al. corroborated retention and oxidative modification of low-density lipoproteins (LDL) in the arterial wall as a trigger of the disease[9].

Nowadays it is commonly accepted that atherosclerosis is an inflammatory disease but nevertheless the underlying causes for imbalance of endothelial function and lipid retention remain elusive. Atherosclerosis is an umbrella term for complex processes taking place in the arterial wall resulting in clinical events and leading to death. Within the next paragraph the pathomechanism of atherosclerosis is summarized.

The arterial wall consists of three layers: the tunica intima, the tunica media and tunica adventitia. The intima is the innermost tunica of the arterial vessel. It is composed of the endothelium, which has direct contact to the blood flow and a subendothelial layer, which forms the internal elastic lamina. The media is next to follow. Smooth muscle cells and elastic tissue are localized in this layer. The adventitia is the outermost layer and contains predominantly collagen fibers. Damage or dysfunction of the endothelium is considered as a critical event triggering atherosclerosis, leading to an increased permeability for substances, such as low-density lipoproteins, and an increased adhesiveness for leukocytes (Figure 1A). Within the arterial intima, lipoproteins undergo oxidative modifications and are internalized by monocytes, which differentiate into macrophage foam cells. Foam cell accumulations appear as early fatty streaks. The local inflammatory response is furthermore sustained by activation of smooth muscle cells and invasion of additional immune cells, which thickens the arterial wall. Macrophages release various cytokines and mediators supporting the inflammatory cascade (Figure 1B).

A mature atherosclerotic plaque is formed surrounded by smooth muscle cells, which form the fibrous cap. Additionally, calcification of the intima and media can occur. The vessel and thus the blood flow are narrowed through plaque formation (Figure 1C). Atherosclerosis-prone regions are located at branching points of the arterial tree. Over time, the plaque converts to an unstable phenotype caused by matrix degradation and apoptosis of immune cells. Subsequently, the plaque consists of pro-thrombotic material. The fibrous cap becomes thinner and is prone to rupture. If plaque rupture occurs the debris provokes the coagulation cascade and the formation of a thrombus (Figure 1D). Thrombus formation occludes the artery and thereby causing clinical manifestations like myocardial infarction or stroke[10].

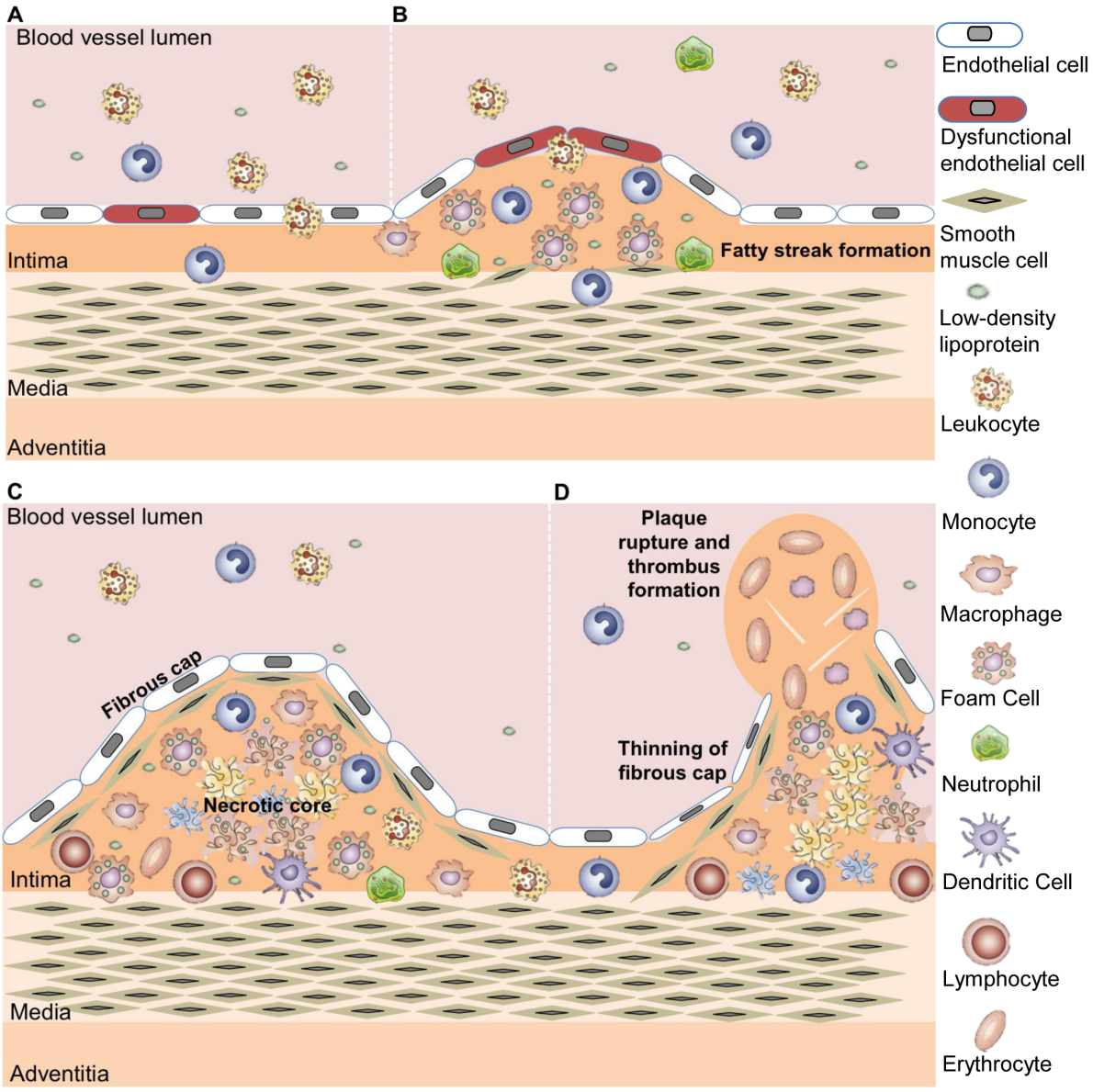

Figure 1 Illustrated development and progression of atherosclerosis. (A) Atherosclerosis develops in the arterial vessel wall, consisting of intima, media, and adventitia. Dysfunction or damage to the endothelium leads to increased permeability and recruits leukocytes. (B) Monocytes engulf lipoproteins, differentiate to macrophages and fatty streaks are formed. Neutrophils are recruited. Smooth muscle cells and other inflammatory cells are activated. (C) Macrophages and other plaque cells undergo apoptosis forming a necrotic core. A fibrous cap consisting of matrix and smooth muscle cells is formed. (D) Matrix degradation by proteases leads to thinning of the fibrous cap creating a potentially unstable plaque. Plaque rupture can occur followed by release of debris activating the coagulation cascade and thrombus formation. Arterial occlusion or embolism is the reason for myocardial infarction or stroke. Idea based on Weber et al.[10].

1.1.1 Endothelial Dysfunction and Hemodynamic Forces

The entrance gate for inflammatory cells and lipids is the vascular endothelium. Under non-diseased conditions it acts as a barrier between the circulation and the vessel wall. The endothelium controls the passage of fluid, macromolecules and inflammatory cells[11, 12]. Different metabolic functions take place within the endothelium to coordinate vasoactivity and to maintain fluidity of blood[13]. Additionally, hemodynamic forces of the blood flow influence the endothelium and activate flow-sensitive proteins or modulate gene expression and thereby atherogenic or athero-protective pathways[14]. Mechanotransducers are expressed, which convert physical stress into biochemical signals[15-17].

Atherosclerosis develops in nonrandom patterns of arterial branching points and areas of altered hemodynamics. In humans as well as in animal models lesions are observed at characteristic regions that experience disturbances in fluid flow and low endothelial shear stress[18, 19]. In mice characteristic regions of plaque development are found in the aortic arch (Figure 2).

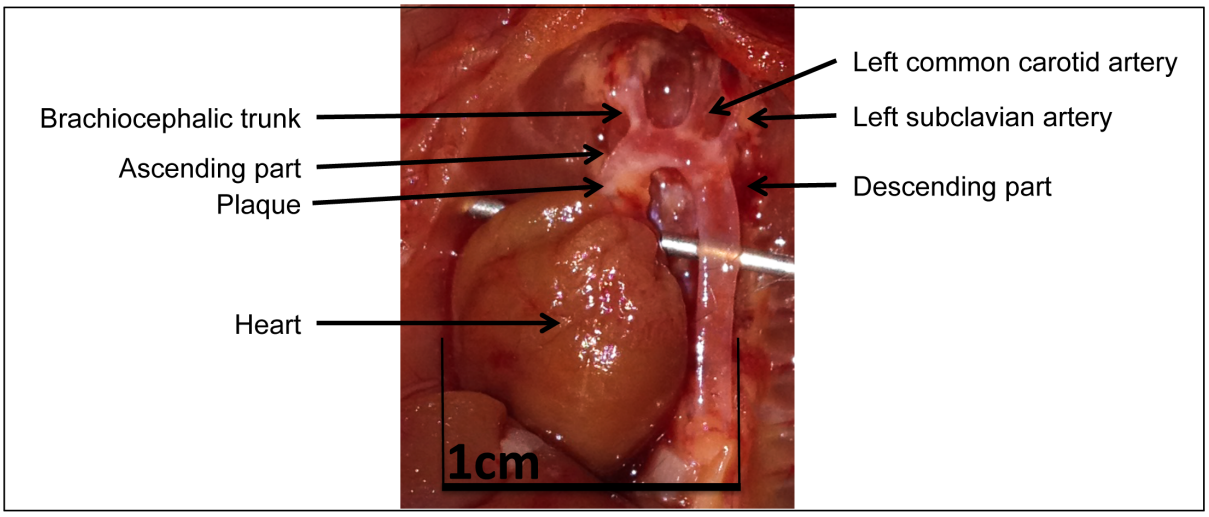

Figure 2 Image of murine aortic arch. Characteristic regions of plaque development are found in the aortic arch. Plaques develop at branching points of the arterial tree. White spots reflect plaques.

Lesion-prone areas are exposed to disturbed laminar flow patterns with low shear stress. Fluid shear stress is the frictional force per unit area from flowing blood that acts on endothelial cells.

Chappell et al. showed that oscillatory shear stress stimulates the expression adhesion molecules such as vascular cell adhesion molecule 1 (VCAM 1) supporting the adhesion and migration of mononuclear cells into the intima initiating inflammation[20].

Regions with unidirectional laminar or pulsatile blood flow and high shear stress are resistant to plaque formation due to expression of athero-protective genes[17, 21].
Endothelial dysfunction is one result of hemodynamic forces acting on endothelial cells.

1.1.2 Lipoprotein Retention and Modification

Hyperlipidemia is associated with cardiovascular diseases and is a key risk factor of atherosclerosis. Elevated plasma cholesterol levels, in particular of LDL, contribute to atheroprogression due to retention and modification within the arterial wall[22].
Circulating lipids are stored and transported in lipoproteins for metabolisation. The lipoprotein particles consist of phospholipids, cholesterol, and apoproteins. Triglyceride-fats and cholesteryl esters are carried inside the lipoprotein and are protected from water by a phospholipid monolayer and apoproteins.
Lipoproteins are classified by their density. High-density lipoproteins transport cholesterol to liver for disposal or recycling. They have anti-inflammatory, anti-atherosclerotic and endothelial protective effects. LDL particles deliver cholesterol to cells for membrane or steroid synthesis. The low-density lipoprotein receptor (LDLR) is expressed for uptake of LDL in cells or liver[23]. Chylomicrons and very low-density lipoproteins contain apolipoprotein E (APOE) as a structural component, which serves as ligand for receptors for clearance[24].
Due to endothelial dysfunction high levels of LDLs lead to a concentration-dependent accumulation of LDLs within the arterial wall. They are trapped in the extracellular matrix of the subendothelial space. In the early 1990s researchers demonstrated that cells of the arterial wall secrete oxidative waste products, which modify LDLs[25]. Oxidized LDLs induce an inflammatory reaction leading to further endothelial dysfunction, upregulation of adhesion molecules, and the recruitment and adhesion of monocytes.

1.1.3 Inflammatory Cells of Atherosclerosis

Atherosclerosis is a highly complex disease progressing over decades in the human arterial system. The inflammatory cells involved in the pathogenesis are part of the innate and adaptive immune response[10, 26, 27].
The immune system consists of two interplaying defense reactions: the innate immune response and the adaptive immune response. The innate immune response, also known as the non-specific or in-born immunity, is the first line defense in the

body. The function of the innate system is the recruitment of immune cells to the site of infection through cytokines, the removal of foreign substances by specialized leukocytes and activation of the adaptive immune system by antigen presentation.
The innate immune cells compromise monocytes differentiating into macrophages, granulocytes (neutrophil, basophil, eosinophil), dendritic cells, and mast cells.
The adaptive immune response is highly specific to a particular pathogen compared to the innate immune response. It consists of specialized cells defending pathogens and establishing an immunological memory. The adaptive immune response is carried out by lymphocytes: Bone marrow derived B cells and thymus derived T cells. The induction time of innate and adaptive immune response differs. The latter is days to decades compared to a fast response of the innate immune system (hours to days)[28].
Atherosclerotic lesions are dominated by macrophages and to a lesser extent also lymphocytes. Recent studies further highlighted the impact of other cell types like neutrophils and dendritic cells in lesion development[26]. The complexity of inflammatory cells involved in the pathogenesis of atherosclerosis will be addressed in this chapter. The role of monocytes and lymphocytes is shortly explained; afterwards the involvement of neutrophils. The given information will only cover some aspects of the current state of research about atherosclerosis.

1.1.3.1 Role of Monocytes in Atherosclerosis

Protagonists of atherosclerosis are macrophages derived from monocytes, which are effector cells of the innate immune response[29]. Macrophages represent with 40% the majority of cells in atherosclerotic plaques in humans[30, 31]. Myeloid progenitor cells are produced in the bone marrow and develop into monocytes. They circulate in the bloodstream followed by migration to inflamed tissue where they differentiate into macrophages. Different subsets of blood monocytes and functional polarization of macrophages were identified in humans and mice[32]. A detailed discussion of the complexity of different subsets of monocytes and macrophages and their involvement in atherosclerosis is reviewed elsewhere. The main aspects how monocytes are involved in the initiation and progression of atherosclerosis are subject of this paragraph.
The main principle of macrophages consists of phagocytosis of pathogens, antigen presentation and cytokine production for further stimulation of the immune response.

The presence of monocytes in atherosclerotic lesion was shown in humans and rabbits in the early 1990s[33, 34]. It was shown that hyperlipidemia, a risk factor of atherosclerosis, increased the production of bone marrow monocytes in animal models of atherosclerosis[35, 36].

Furthermore the spleen was identified as a reservoir for monocytes proving that mobilized monocytes in atherosclerotic lesions mainly originate from spleen[37].

Dysfunction of the endothelium combined with hemodynamic forces trigger endothelial cells to express adhesion molecules and chemokines. Subsequently, monocytes transmigrate through the endothelium in several steps. The most important upregulated endothelial adhesion molecules are E- and P-Selectin as well as VCAM 1, which are found in atherosclerotic lesion[38]. Deficiency of the mentioned adhesion molecules protects against atherosclerosis in apolipoprotein E knockout mouse models[39, 40].

Additionally, chemokine-receptor interactions are crucial for trafficking of monocytes due to their chemotactic effects. Soehnlein et al. showed that C-C chemokine receptor type 1 and 5 are essential in the recruitment of monocytes[41].

After tissue invasion monocytes initiate an early immune response and differentiate into macrophages. Modified lipoproteins are internalized by macrophages by scavenger receptors and phagocytosis. Foam cell formation takes places, which is characteristic for early plaque formation and further plaque growth. Macrophages release growth factors and cytokines triggering lesion progression and cell recruitment. On the one hand lipoproteins are degraded in macrophages, but on the other also processed by the endosomal pathway for antigen presentation[42], thus initiating the adaptive immune response (Chapter 1.1.3.2).

Macrophages are present in all stages of atherosclerosis. In later stages they contribute to plaque rupture by production and secretion of various proteases that promote degradation of the plaque[43].

1.1.3.2 Role of Lymphocytes in Atherosclerosis

As indicated above macrophages act as antigen presenting cells and can recruit lymphocytes, especially T cells, into atherosclerotic lesions.

T cells are part of the adaptive immune response. They mature in the thymus and are recruited to sites of inflammation where they recognize foreign antigens presented to them. There are several subsets of T cells with specific functions for cell mediated

immune response and stimulation of B cells to produce antibodies against the antigen.

T cells represent 10% to 20% of cell population in human plaques[30]. Modified lipoproteins are internalized and processed in macrophages for antigen presentation. T cells enter the plaque and interact with antigen presenting macrophages, which represent the linking of innate and adaptive immune response[28, 31]. After activation and proliferation T cells secrete cytokines, which prime macrophages for further activation. In addition smooth muscle cells and endothelial cells are activated to promote the inflammatory process[42].

Several studies about cytokines, not only secreted by T cells, have been conducted during the last decade. Pro- and anti-inflammatory cytokines have been identified regulating mononuclear cell recruiting to atherosclerotic lesions and supporting the inflammatory process[44, 45]. A complex cascade of pathways initiated by inflammatory cells is involved in atherogenesis showing their relevance for atherosclerotic vascular disease and further research.

1.1.3.3 Role of Neutrophils in Atherosclerosis

Besides macrophages that are considered key players in the formation of atherosclerotic lesions, it was shown in the last years that neutrophils also play an important role in atherosclerosis, in particular during early stages of lesion formation[46-49]. As part of the innate immune system, neutrophils are usually recruited for first line defense against invading pathogens. Neutrophils are produced in the bone marrow and are recruited up on inflammatory stimuli. Elimination of pathogens is achieved by different killing mechanisms. Neutrophil-specific effector molecules are released by degranulation, such as myeloperoxidase, neutrophil elastase (NE), cathepsin G and proteinase 3[50]. Additionally, neutrophil specific pathogen elimination is accomplished by releasing neutrophil extracellular traps (NET). Neutrophils and their effector molecules have been identified in murine and human atherosclerotic plaques by immunohistochemistry, fluorescence techniques (flow cytometry) and confocal microscopy[46, 48, 49, 51-53]. Neutrophil detection in atherosclerotic plaque is a challenging task due to the short life span and rapid functional turnover of neutrophils[54]. Functionally, it has been demonstrated that neutrophils accumulate within atherosclerotic vessels in particular during early plaque formation and secret preformed granule proteins, which may instruct recruitment and activation of other

inflammatory cells to promote atherosclerotic lesion formation[55]. Depletion of neutrophils in an atherosclerotic mouse model proved the contribution of neutrophils in atherosclerotic lesion development[56]. It was shown in mice and human studies that peripheral counts of neutrophils correlate with plaque size[56-58]. Compared to macrophages and T cells, neutrophils reside only a short time in atherosclerotic lesions[59].

Neutrophil recruitment and trafficking through the endothelium is similar to monocyte extravasation and is regulated by adhesion molecules[60].

Neutrophil specific-effector molecules are stored in four compartments: the primary granules (azurophilic granules), secondary granules (specific granules), and tertiary granules as well as secretory vesicles as presented in Table 1[50, 61].

Table 1 Neutrophil specific-effector molecules. Neutrophils discharge different sets of granules and deliver multiple anti-microbial molecules. The granule subsets are additionally differentiated by their tendency to undergo phagocytosis. Secretory granules are more readily exocytosed than tertiary granules and so on. CD, cluster of differentiation; CR, complement receptor. Based on Nathan et al. [50] and Pham et al.[61].

Increasing tendency for exocytosis →

Primary Granules (Azurophilic Granules)	Secondary Granules (Specific Granules)	Tertiary Granules (Gelatinase Granules)	Secretory Granules
• Neutrophil elastase • Myeloperoxidase • Cathepsin G • Proteinase 3 • Azurocidin • Bacterial permeability-increasing protein • Defensins	• Lactoferrin • Cathelicidin • Lysozyme • Collagenase • Leukolysin • Matrix metalloproteinase 9	• Gelatinase • Leukolysin • Lysozyme	• CR 1 • CR 3 • CD14 • CD16

During extravasation of neutrophils from the blood stream granules are released to enhance degradation of microorganism, monocyte and dendritic cell recruitment, cytokine release, and thereby the inflammatory process[55, 61, 62].

A number of granule proteins were localized in human atherosclerotic lesions by immunohistochemistry[63-66]. But, they were also co-localized with endothelial cells, macrophages, and smooth muscle cells due to potential uptake of granule proteins. Additionally, elevated plasma levels of myeloperoxidase and matrix metalloproteases 9 (MMP) correlated with coronary artery disease in humans[67].

Neutrophils exhibit a special mechanism to trap pathogens. By undergoing a specific cell death, neutrophils can release NETs thus immobilizing pathogens. NETs consist

of decondensed chromatin containing granule proteins neutrophil elastase and myeloperoxidase[68, 69]. Recently NETs were found within arteries of atherosclerotic mice[70, 71]. Investigating the interplay between macrophages and neutrophils, NETs were shown to prime macrophages for cytokine release, boosting the inflammatory process and promoting atherosclerotic lesion formation in mice[72]. Furthermore it was shown that NETs are present in human plaques, but if the interplay between macrophages and neutrophils in mice can be translated to patients and the clinic remains elusive[73, 74].

1.2 Mouse Models of Atherosclerosis

Research about atherosclerosis, especially plaque development and underlying cellular and molecular processes, is mainly carried out in animal models. Pathophysiological processes are mimicked in animal models and more or less comparable lesions to humans are developed. Atherosclerotic studies in monkeys, pigs, rabbits, and mice have been conducted to gain more insights in plaque formation[75]. Nevertheless, the most utilized model to study atherosclerosis is the mouse. Since more than two decades different mouse models of atherosclerosis have been created by genetic manipulation with molecular techniques[76-79]. Mice strains offer advantages of easy breeding, short generation times, and large litter size. Low-density lipoproteins are assigned as the principle risk factor of atherosclerosis[22]. Inducing atherosclerosis in mice was achieved by alteration of lipid metabolism and deficiency of either APOE gene or LDLR gene. Paigen et al. proposed a pro-atherogenic diet developing hyperlipidemia and lesion formation in inbred strains but without correlation to plasma lipid levels[80].

Zhang et al. as well as Plump et al. introduced the APOE deficient (*APOE*$^{-/-}$) mice in 1992[76, 77]. The LDL-receptor deficient (*LDLR*$^{-/-}$) mouse strain was described one year later by Ishibashi et al.[78]. Both established mouse models are based on a common inbred laboratory mouse strain (C57BL/6). The genetically modification causes the development of severe hypercholesterolemia by feeding a high fat diet (HFD) and thus plaque formation in the vascular tree of the aorta.

Comparing plaque development of mice to humans, both develop plaques in regions of vasculature with low or oscillating wall shear stress[81]. Nevertheless, a major drawback of both murine mouse models is the lack of spontaneous plaque rupture

and thrombosis[82] leading to myocardial infarction or stroke, which is the clinical risk in humans. Recently, the causal connection between plaque rupture and myocardial infarction was shown in a hyperlipidemic mouse model and thus imitating human coronary artery disease[83].

A discussed disadvantage of APOE deficient mice is the dissimilarity of the lipoprotein profile to those in humans[84]. The cholesterol level of APOE deficient mice is higher in the lipoprotein fraction of very low-density lipoproteins. But in humans cholesterol is mainly carried by LDL particles, which is seen in the *LDLR*$^{-/-}$ knockout mouse model. Furthermore, familial hyperlipidemia involves mutations in the LDLR gene in humans[23]. To mimic a lipoprotein profile similar to humans the following experiments in this thesis were conducted with the *LDLR*$^{-/-}$ knockout mouse model.

1.3 Imaging Modalities to Target and Visualize Atherosclerosis

Imaging modalities, such as computed tomography or magnetic resonance imaging, have been further developed and applied over the years. Nowadays non-invasive molecular imaging techniques are state of the art in preclinical research for investigation of underlying biological processes and monitoring of drug treatment in vivo. Moreover they support knowledge about disease progression and can be translated for prediction of clinical events in humans. Molecular imaging can be defined as the application of specialized imaging devices used alone or in combination with targeted imaging agents to visualize biological processes over time[85].

In Figure 3 an overview is given about molecular imaging technologies used in preclinical and clinical settings in the context of atherosclerosis.

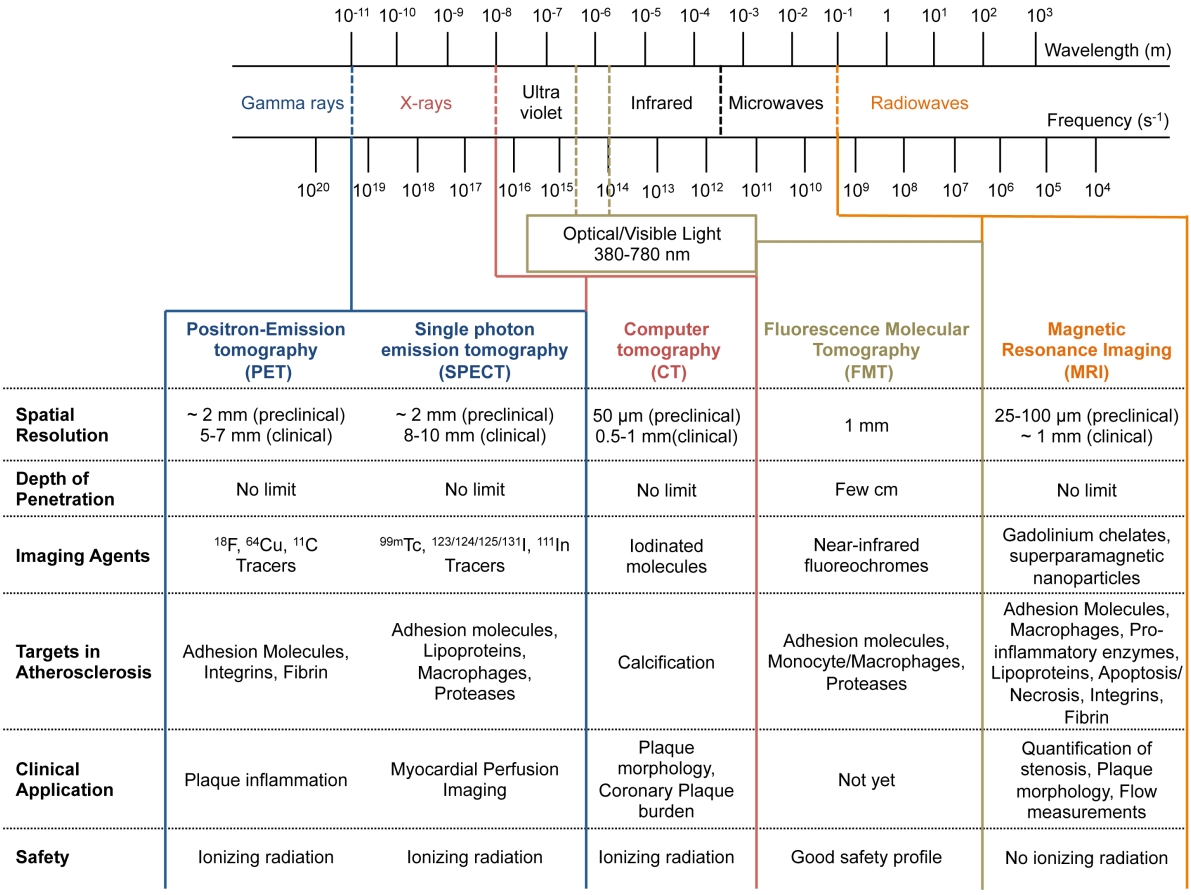

	Positron-Emission tomography (PET)	Single photon emission tomography (SPECT)	Computer tomography (CT)	Fluorescence Molecular Tomography (FMT)	Magnetic Resonance Imaging (MRI)
Spatial Resolution	~ 2 mm (preclinical) 5-7 mm (clinical)	~ 2 mm (preclinical) 8-10 mm (clinical)	50 µm (preclinical) 0.5-1 mm(clinical)	1 mm	25-100 µm (preclinical) ~ 1 mm (clinical)
Depth of Penetration	No limit	No limit	No limit	Few cm	No limit
Imaging Agents	^{18}F, ^{64}Cu, ^{11}C Tracers	^{99m}Tc, $^{123/124/125/131}$I, ^{111}In Tracers	Iodinated molecules	Near-infrared fluoreochromes	Gadolinium chelates, superparamagnetic nanoparticles
Targets in Atherosclerosis	Adhesion Molecules, Integrins, Fibrin	Adhesion molecules, Lipoproteins, Macrophages, Proteases	Calcification	Adhesion molecules, Monocyte/Macrophages, Proteases	Adhesion Molecules, Macrophages, Pro-inflammatory enzymes, Lipoproteins, Apoptosis/ Necrosis, Integrins, Fibrin
Clinical Application	Plaque inflammation	Myocardial Perfusion Imaging	Plaque morphology, Coronary Plaque burden	Not yet	Quantification of stenosis, Plaque morphology, Flow measurements
Safety	Ionizing radiation	Ionizing radiation	Ionizing radiation	Good safety profile	No ionizing radiation

Figure 3 Overview of key molecular imaging technologies. Imaging technologies are based on electromagnetic radiation consisting of electromagnetic waves. Electromagnetic waves are characterized by their wavelength or frequency and classified in: radio, microwave, infrared, visible, ultraviolet, X-rays, and gamma rays. Imaging modalities used in atherosclerosis research are mapped onto the electromagnetic spectrum. Each imaging modality is displayed with their advantages and limitations in the context of atherosclerosis. Idea based James et al.[85] and Wildgruber et al.[86].

Different imaging modalities have been used and adopted for atherosclerotic research and clinical application[86].

In this work different approaches of imaging modalities are used to address biological processes during plaque formation. In the following paragraphs two imaging modalities, namely fluorescence molecular tomography (FMT) combined with X-ray computed tomography (XCT) and magnetic resonance imaging (MRI), are explained and presented in the context of atherosclerosis.

In addition an introduction is given about three-dimensional (3D) representation based on reconstructed serial histological sections. Histological reconstruction can be used to visualize diseased tissue on a cellular level.

1.3.1 Fluorescence Molecular Tomography Combined with Computed Tomography

The combination of optical imaging by employing fluorescent light and X-ray attenuation is used within this thesis. First of all the basic principles of XCT and FMT are reviewed followed by their implications for studying atherosclerosis.

Computed tomography (imaging by sections) is based on X-ray attenuation of a scanned subject resulting in a three-dimensional anatomical image. X-ray source and detector are placed on opposite sides and rotating around the subject (Figure 4).

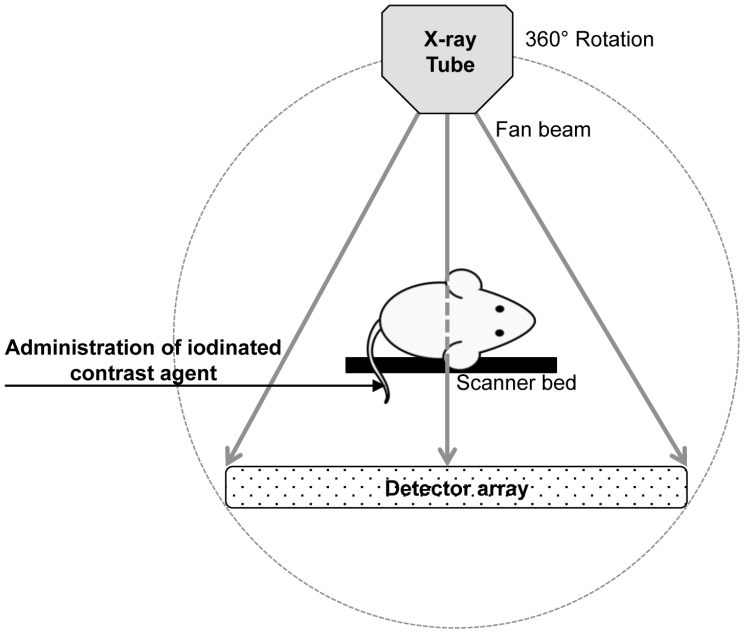

Figure 4 Schematic illustration of X-ray computed tomography. An iodinated contrast agent is injected to the subject (in this case a mouse). The X-ray source and the detector rotate in 360° around the subject. Idea based on James et al.[85].

The attenuation of the tissue is measured and is displayed on the Hounsfield scale.
For soft tissue contrast enhancement contrast agents with iodine or barium sulfate are used. Advantages of XCT imaging are high spatial resolution, cost-effectiveness and fast acquisition times[86]. Nevertheless, it is restricted to anatomical information and the disadvantageous exposure to radiation[85].
XCT can be used to target calcification of atherosclerotic plaques, which can be detected without contrast agent. Iodine contrast agents support the detection of non-calcified plaques in humans[87]. Macrophages were detected in atherosclerotic plaques of rabbits using a contrast agent with iodinated nanoparticles[88].
Nevertheless, XCT as stand-alone device is only useful for morphological data acquisition based on tomographic images. In combination with other imaging modalities XCT provides anatomical references for better localization of biological processes.

Visible light in the wavelength range 380 – 780 nm of the electromagnetic spectrum is used for microscopic techniques for hundreds of years. A further development for cellular biology was fluorescent microscopy to visualize molecular events in cells or ex vivo with fluorescent-reporters or fluorescent-tagged molecules[85]. Based on this, macroscopic optical imaging modalities, such as bioluminescence and fluorescence imaging, were developed. They offer the possibility to image living animals non-invasively.
Fluorescent molecular tomography is based on passing light through biological tissue in the near-infrared spectrum (650 – 900 nm). In preclinical animal research near infrared fluorescent (NIRF) imaging agents or fluorescently labeled reporters are injected to resolve fluorescent distribution in vivo non-invasively and thereby quantify and visualize cellular and molecular events[85, 89]. Disease progression can easily be tracked as well as monitoring of drug therapies.
The setup of fluorescent molecular tomography consists of a filtered laser light source and a charge-coupled device (CCD) camera for detection of emitted light placed on opposite sides of the scanned object. The illumination is made in the excitation's wavelength of the injected fluorophor (Figure 5).

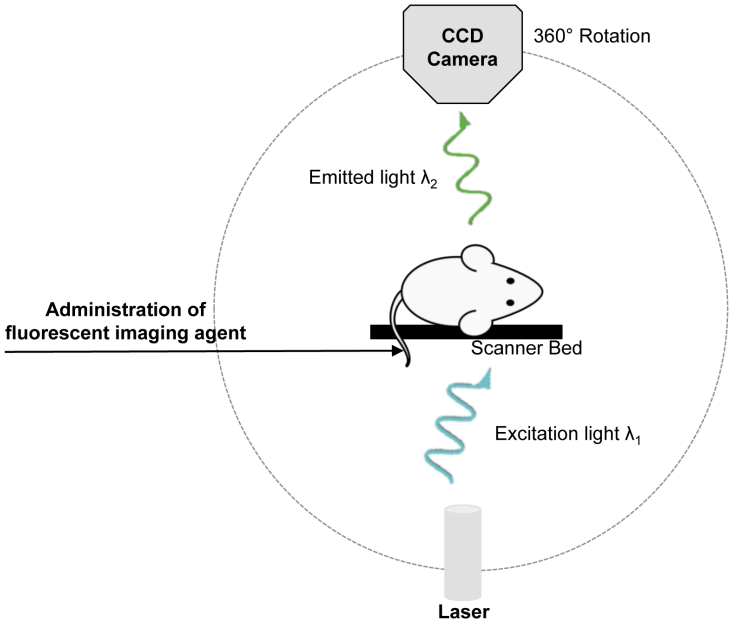

Figure 5 Schematic illustration of fluorescence molecular tomography. The NIRF imaging agent is administered and the appropriate wavelength is used to excite the fluorophor. The emitted light is detected with a CCD camera. Idea based on James et al.[85].

FMT offers a highly sensitive three-dimensional detection of fluorescent contrast agent in a depth of several centimeters. Tissue autofluorescence of hemoglobin and other molecules is the lowest in the spectrum above 650 nm. Thus, the contrast to noise ratio is improved. Other advantages of FMT imaging are cost-effectiveness and absence of radiation[85, 86]. Due to the fact that the penetration depth of FMT is limited clinical translation is restricted.

Optical tomography reconstruction of FMT imaging is challenged by light scattering and attenuation and thus precise quantification and localization. To improve FMT performance a hybrid system for simultaneous fluorescence molecular tomography and X-ray computed tomography (FMT-XCT) was developed, which improves accurate co-registration. XCT offers anatomical information, which can be merged with molecular data obtained with FMT. The system is based on a 360° rotating gantry of X-ray source-detector and an orthogonally mounted laser source and a CCD camera[90-92]. The setup of a hybrid FMT-XCT system is shown in Figure 6.

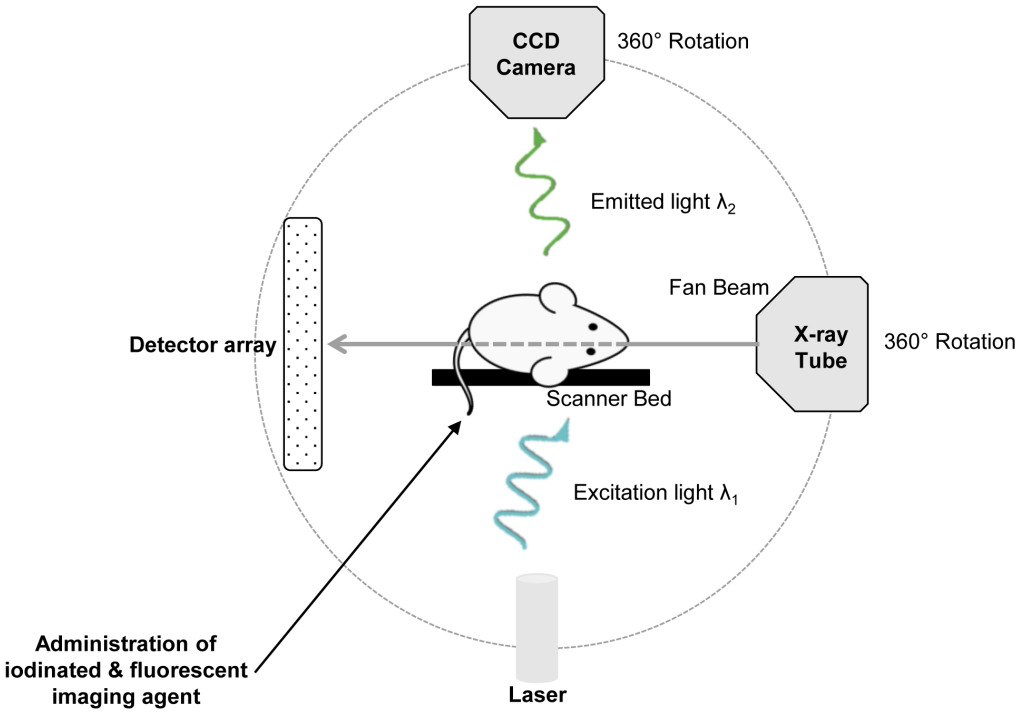

Figure 6 Schematic illustration of hybrid FMT-XCT system. The hybrid FMT-XCT combines FMT and XCT imaging modalities. After an excitation-emission scan with an injected fluorophore, a XCT scan is applied to acquire anatomical information. The hybrid system is rotating 360° around the subject.

FMT-XCT improves the imaging reconstruction accuracy by introducing the XCT prior to the FMT inversion[93].

Three different kinds of NIRF probes (the word probe is synonymous to imaging agent) are used for FMT imaging in animal models:

- Unspecific fluorescent probes, which are distributed in different compartments of the body or serve as blood pool agents in the vasculature.
- Fluorescent probes with a specific target, resulting in an antigen-antibody reaction.
- Activatable probes, which are activated by enzymatic reactions before emitting a fluorescent signal. Activatable probes consist of quenched fluorophores in the inactive state and are also called “smart probes”[94, 95].

Fluorescence molecular imaging combined with X-ray computed tomography has emerged as a powerful tool in preclinical atherosclerosis research, as it can target multiple biological aspects of the disease by using high-affinity ligands labeled with near-infrared-fluorochromes that are directed towards key cellular and molecular players of atherosclerosis[91, 96-102].

In later stages of plaque development a fibrous cap is formed overlying the lipid core. Inflammatory cells, especially macrophages produce inflammatory proteinases. Proteolysis and degradation of extracellular matrix takes place, thereby supporting

thinning and rupture of the fibrous cap. In particular, MMP action in macrophages have been visualized using an activatable near-infrared imaging agent in atherosclerotic mice[99]. In addition, ex vivo NIRF imaging of MMP activity was shown to be successful in human carotid endarterectomy specimens[103].
Further, cathepsin B protease activity in atherosclerotic lesion in mice was detected with so called “smart” probes. Macrophages were identified as the main source of proteases[87, 96, 102]. The recently published studies in preclinical atherosclerotic research using NIRF imaging agents mainly focused on later stages of plaque development. Early plaque development was not yet addressed with this imaging modality.

Alongside the in vivo detection of fluorescent biodistribution and localization, ex vivo quantification is essential for probe verification. Sarantopoulos et al. developed a multispectral epi-illumination cryoslicing imaging method for this purpose[104]. After in vivo FMT-XCT imaging the animals are euthanized and prepared for whole-body cryoslicing and the fluorescence distribution is captured ex vivo. Additionally, immunofluorescence staining or immunohistochemistry can be applied to whole-body cryosections for further analyses[104].

1.3.2 Magnetic Resonance Imaging

Another imaging modality, which is frequently used for plaque imaging, is MRI. MRI uses a powerful magnetic field in conjunction with radiofrequency pulses to visualize internal structures and soft tissue morphology of the body[85].
Atomic nuclei change their behavior if they are placed in magnetic fields. They act as magnetic dipoles and align parallel or anti-parallel with the magnetic field. The natural abundance of hydrogen nuclei (^{1}H) in form of tissue water molecules is the principle of magnetic resonance imaging.
A MRI scanner consists of a superconducting magnet generating a homogenous magnetic field, gradient coils creating variations in the magnetic field and a radiofrequency coil generating a pulse to alter the alignment of magnetic dipoles (Figure 7).

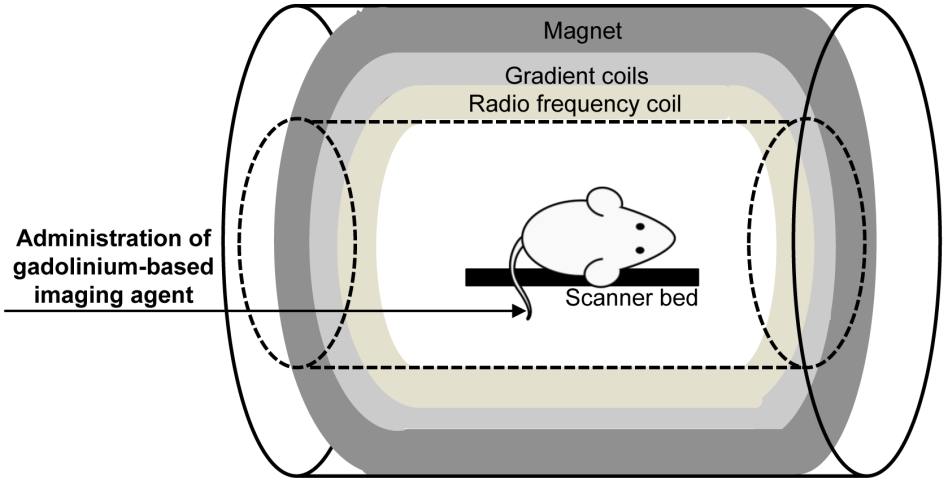

Figure 7 Schematic illustration of MRI scanner. After administration of a gadolinium-based or superparamagnetic iron oxide contrast agent, a MRI specific sequence is applied to scan the subject. The MRI scanner consists of a magnet, gradient coils and a radiofrequency coil. Idea based on James et al.[85].

In response to changes in the magnetic field and of the radiofrequency, a signal is generated by the ability of atomic nuclei to return to the initial alignment in the magnetic field (= relaxation). This can be transformed into a representative image. Two relaxation forms occur: longitudinal (T1 relaxation) and transverse (T2 relaxation) relaxation. Each tissue has a characteristic relaxation time resulting in differences of contrast in the representative image. Enhancement of contrast is achieved with contrast agents by shortening T1 and/or T2 values of the tissue. Subsequently, MR sequences can address T1 or T2 relaxation. MRI combines key advantages of non-invasive imaging: anatomical and molecular imaging with high spatial resolution, non-ionizing, unlimited penetration death, soft tissue contrast and clinical utility for patient imaging and monitoring over time[85, 86, 105, 106].

Imaging agents containing either gadolinium (Gd) chelates[107] or superparamagnetic iron oxide particles are used to increase signal intensity[108]. The application of gadolinium-based contrast agents with T1 weighted sequences result in increased T1 relaxation improving signal intensity. Gadolinium chelates cause nearby protons to relax much faster than usual[106]. Superparamagnetic iron oxide nanonparticles are classified upon their size. Depending on their size they have different effects on T1 and T2 weighted sequences. Large superparamagnetic iron oxide particles have a stronger effect on T2 relaxation compared to smaller particles which effect stronger T1 relaxation[109].

Several approaches of molecular MRI of atherosclerosis have been developed over the years, which mainly address biological activity during plaque formation. To

demonstrate endothelial dysfunction targeted iron nanoparticles have been used to visualize activated and inflamed endothelium, for example VCAM 1, in the aortic root of atherosclerotic mice[110]. Gadofosveset, a gadolinium-based contrast agent, was successfully used to track changes in endothelial permeability in atherosclerotic mice and patients with carotid artery disease[111, 112].

Macrophages are key players of plaque formation. Non-invasive macrophage imaging in experimental models of atherosclerosis and in humans was achieved with superparamagnetic iron oxide particles. The nanoparticles are phagocytized by macrophages in the plaque and thereby induce signal enhancement of atherosclerotic aortas[113-115]. Plaque composition is further characterized by high lipid content. The contrast agent Gadofluorine M, containing a lipophilic, macrocyclic chelate of gadolinium, was used to assess plaque imaging. This agent accumulates in fibrous lipid-rich parts of atherosclerotic plaques in rabbits due to its chemical properties binding to collagens, proteoglycans, and tenascin[116, 117]. Degradation of extracellular matrix occurs in advanced plaque stages. An elastin specific gadolinium-based MR contrast agent was recently published to image vessel wall remodeling in animal models[118]. Elastin is a major wall component. The immature precursor of elastin, tropoelastin, is present in macrophage-rich plaque regions. The elastin specific contrast agent was further developed for specific binding to tropoelastin. Currently experiments with animals and ex vivo human carotid samples have been conducted with this tropoelastin specific contrast agent implicating a more precise imaging approach (data not published, René Botnar, King's College London). Proteolytic enzymes, such as MMP, can further support the formation of vulnerable plaques, prone to rapture. Lancelot et al. and Hyafil et al. imaged MMP activity with a gadolinium chelate conjugated to a MMP inhibitor[119, 120].

However, to accurately quantify the MRI signal of MRI agents tracking molecular and cellular processes, these must be analyzed and verified ex vivo. The in vivo signal is determined by the local chemical environment and compartmentalization of the agent. Consequently, precise tissue quantification and spatially resolved localization of gadolinium-based contrast agents remains challenging due to nonlinear correlation of the in vivo signal with the actual tissue concentration ex vivo. Matrix-assisted laser desorption/ionization imaging mass spectrometry (MALDI-IMS) offers a new possibility to spatially resolve quantification of MRI agents in tissue sections, which will be further addressed in this thesis[121]. Mass spectrometry, in combination with

liquid chromatography, is routinely used in diagnostic medicine and offers high sensitivity and molecular specificity. Barkhausen et al. were the first who quantified gadolinium concentrations in atherosclerotic plaques with inductively coupled plasma mass spectroscopy (ICP-MS)[122]. ICP-MS is a powerful tool to determine concentrations of elements in tissue after digestion[123].

Furthermore a combination of MALDI combined with imaging mass spectrometry was developed to detect and quantify molecules on ex vivo tissue[124]. This MALDI-IMS technology has been applied and validated to detect gadolinium-based contrast agents in mouse liver[125]. Aichler et al. proved that various gadolinium compounds were identified ex vivo with MALDI-IMS in the infarct scar after experimental murine myocardial infarction after in vivo application. They showed for the first time that MALDI-IMS is able to spatially resolve and quantify contrast agent distribution and thus is used to confirm the in vivo imaging signal[121].

Over the last decade technical progress in the molecular imaging field was made to visualize biological processes underlying the pathogenesis of atherosclerosis. The overall goal of preclinical imaging research is the translation of knowledge to the clinic with the overall goal to prevent and predict clinical outcomes such as myocardial infarction or stroke.

1.3.3 Three-Dimensional Reconstruction Based on Serial Histological Sections

Visualization of cells and tissue by using light microscopic techniques contribute to the analysis of molecular and biological processes to gain further insights in pathological features for hundreds of years[126]. Preclinical molecular imaging modalities as described above focus on living subjects to track biological processes over time. A snapshot for accurate description and characterization of tissue morphology and cellular content ex vivo is achieved by histological methods. Histology is defined as the study of microscopic anatomy of cells or tissue using staining techniques combined with light microscopy. Therefore, the tissue is removed or dissected followed by chemical fixation, dehydration steps, embedding for sectioning, sectioning, and mounting on microscope slides. Staining is employed to enhance contrast and to visualize tissue morphology and cells.

Imaging techniques such as micro-computed tomography (µCT), microscopic magnetic resonance imaging and confocal laser scanning microscopy can produce

3D imaging reconstructions in high resolution[127]. Histological sections of conventional histology represent a two-dimensional (2D) view on healthy and diseased tissue with precise information about tissue structure and cellular composition. Nevertheless, many pathological conditions have a spatial and functional relationship such as atherosclerosis[128]. Thus, 3D reconstruction of tissue at microscopic resolution has evolved over the years to enhance knowledge about biological and pathological processes[129].

To achieve 3D reconstruction based on histological images of serial histological sections, some aspects have to be considered: After sample collection, formalin fixation and dehydration for paraffin embedding, the biological material of interest is serially sectioned, with a defined thickness of each slice, followed by histological staining and digitization performed with a light microscope to generate the 2D histological imaging data set.

The challenging part of 3D reconstruction is the registration and alignment of the 2D histological imaging data set to a 3D reconstruction. During the acquisition workflow, from sample collection to image generation, several deformations emerge and the overall structure is disassembled exacerbating the reconstruction. Histological preparation and fixation causes global 3D deformation and shrinkage in situ. Fixation of the tissue and loss of fluids, e.g. removing blood in vessels, induces shrinkage of the tissue. Due to mechanical forces of e.g. scissors and forceps the tissue can additionally be deformed. Dauguet et al. defined these deformations as “primary deformations” because they arise first in the workflow[130].

During the cutting process with the microtome, slice specific 2D deformations occur as a result of shearing and tearing[130]. Mounting the tissue section on the microscope slide causes changes in the original geometry by rotation and translation of the section (misalignment of sections). In addition, slices can get lost during the cutting process. Deformations appearing within and after the cutting process are called “secondary deformations”[130]. “Primary and secondary deformations” hamper the 3D reconstruction of histological sections. The literature describes different approaches of alignment and registration algorithm for reassembling a 3D volume and geometric correction of distortion.

Malandain et al. introduced the so-called *banana problem:* a 3D curved object cannot be reconstructed from cross sections without any additional information. Implementing supplementary data into the reconstruction can reduce the deviation of

the true, anatomical shape[131]. Either a registration between consecutive sections is made or reference points are used for alignment[132-134]. Therefore, internal features of the tissue are used or fiducial markers are introduced into the tissue block[135]. Furthermore, histological sections could be co-registered to external reference images prepared with 3D in vivo imaging or 2D block-face images acquired during sectioning[130, 136-138].

3D histological reconstructions are mainly described in the area of neuroscience. A 3D reconstruction based on histological sections of human atherosclerotic carotid plaques combined with in vivo imaging was published by Groen et al.[139]. They present a multiscale registration approach of human histological images to in vivo and ex vivo high resolution imaging techniques to compensate deformations as described above. Nevertheless, a crucial step in the published protocol setup was the correction of the vessel angulation by using imaging techniques for registration.

Histological reconstruction of the murine aortic arch could offer deeper insights into atherosclerosis and information on spatial and functional relationships of plaque development and regional cell distributions.

1.4 Aim of this Thesis

Atherosclerotic lesion formation is a complex biological progress driven by hemodynamics forces, which is not yet fully understood. Imaging technologies are applied in cardiovascular research to better understand disease mechanism and to test new treatments. A potential translation to the clinic in order to predict cardiovascular risk is the long-term goal.

In this thesis different imaging approaches are used with the aim to target and visualize atherosclerosis:

The first approach aims to identify a method to detect early atherosclerotic lesions, which are associated with neutrophil infiltration. It is based on imaging of increased enzymatic activity within the plaque, respectively elastase activity - a neutrophil serine protease. We therefore hypothesized that elastase-targeted imaging could be used for in vivo detection of early atherosclerosis. A NIRF imaging agent specific for elastase secreted by neutrophils was first evaluated in vitro, followed by in vivo analyses in the *LDLR*$^{-/-}$ atherosclerotic mouse model with FMT-XCT and ex vivo verification.

Furthermore, imaging and visualization of more developed atherosclerotic lesions is addressed within our second approach. We hypothesized that Gadofluorine P could be used as a plaque-targeting MR contrast agent to address components of the extracellular matrix, respectively plaque composition, in the course of atherosclerosis in *LDLR*$^{-/-}$ mice. Furthermore, we postulated that MALDI-IMS is a suitable method to quantify gadolinium chelates within atherosclerotic plaques ex vivo. After relaxivity measurements of the contrast agent, in vivo kinetics in atherosclerotic *LDLR*$^{-/-}$ mice were conducted. Afterwards Gadofluorine P is applied in the course of atherosclerosis followed by ex vivo quantification with MALDI-IMS.

While in the above approaches we focused on defined biological activities within the plaque the third approach deals with the application of imaging modalities to create a 3D representation of the murine aortic arch. This can be achieved with 3D reconstruction of serial histological sections to visualize regions of plaque development and regional distribution of different cell types. The assessment of an

experimental workflow how serial histological sections of the murine aortic arch, respectively images, can be reconstructed to a 3D object with the support of imaging modalities is the aim of the third approach.

2 MATERIAL & METHODS

2.1 Imaging Agents for Targeting Atherosclerosis

Different imaging agents are used to target atherosclerosis: A NIRF imaging agent is used for targeting enzymatic activity in atherosclerotic plaques. A MR imaging agent is used to target contrast agent interaction with extracellular matrix components in atherosclerotic plaques. In addition, a non-targeted clinically applied MR imaging agent is used for contrast enhanced imaging of the aortic arch.

2.1.1 Elastase Targeted Fluorescence Molecular Imaging

To target neutrophils, respectively the granule enzyme elastase, with fluorescence molecular imaging the contrast agent Neutrophil Elastase 680 FAST™ (NEV11169, Perkin Elmer, Waltham, USA) was used. The contrast agent acts as a substrate for NE and consists of a dedicated peptide sequence (PMAVVQSVP) with two VivoTag-S680 fluorochromes. The fluorochromes are self-quenched and become highly fluorescent after cleavage by neutrophil elastase (Figure 8). This preclinical imaging agent emits light in the near infrared spectrum (excitation 675 nm / emission 693 nm). The blood half-life is 4 hours (h) and it is cleared by renal excretion. The agent is injected intravenously with a dose of 4 nmol/ 25g mouse. Imaging is conducted 4h post injection[140].

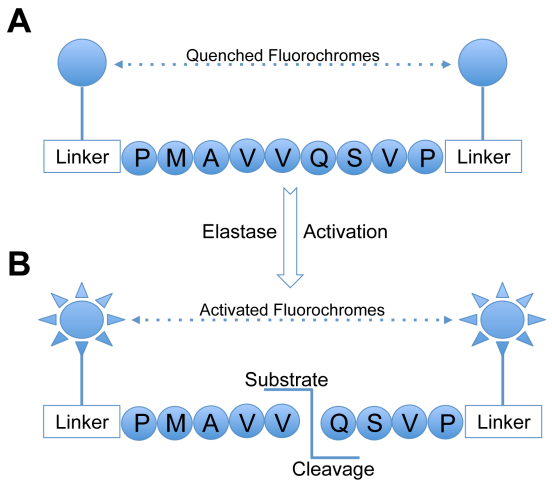

Figure 8 Chemical design of neutrophil elastase imaging agent. (A) A peptide sequence is conjugated to two VivoTag-S680 fluorochromes. Due to spatial proximity the fluorophores are quenched. (B) After cleavage of the peptide by NE the fluorophores become highly fluorescent. Abbreviations of amino acids: Alanine – A; Glutamine – Q; Methionine – M; Proline – P; Serine – S; Valine – V. Idea based on Kossodo et al.[140].

2.1.2 Plaque Targeted Magnetic Resonance Imaging

For plaque targeted magnetic resonance imaging the contrast agent Gadofluorine P (invivoContrast GmbH, Berlin, Germany) was used. This MRI imaging agent belongs to the family of gadolinium-based contrast agents. It is amphiphilic with a molecular weight of 1322.17 g/mol. Due to the chemical structure it forms micelles in aqueous solutions (Figure 9A). The amphiphilic agent adsorbs to proteins and filaments of the extracellular matrix due to different surface charges[117, 141]. Plasma protein binding is more than 90%, resulting in a plasma half-life in rats of about 2 h[142]. The excretion of Gadofluorine P is biliary.

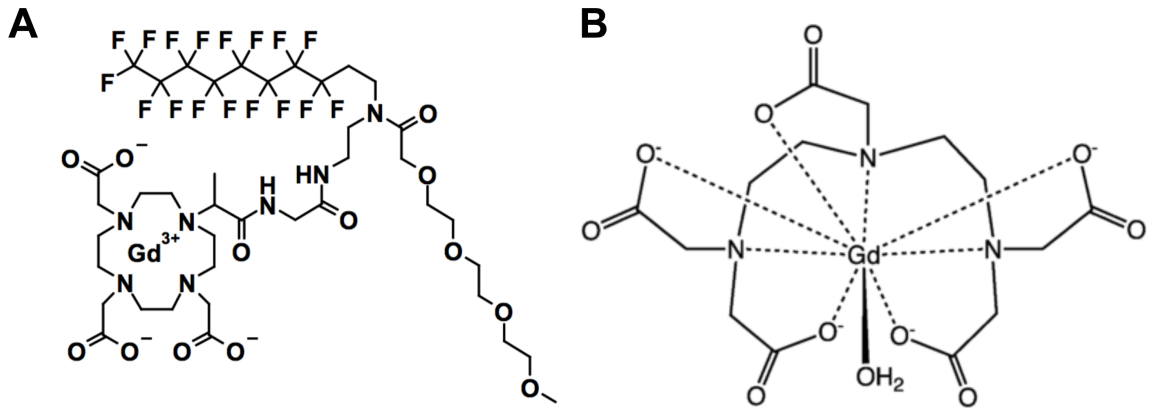

Figure 9 Chemical structures of MRI contrast agents. (A) Gadofluorine P. (B) Gd-DTPA

2.1.3 Contrast Enhanced Imaging of the Aortic Arch

The MRI contrast agent Magnevist® (further referred to as Gd-DTPA: Gadolinium-Diethylenetriaminepentacetate, Bayer Schering) is used for contrast enhanced imaging of the aortic arch. Contrast enhanced imaging of the aortic arch supports the workflow in order to create a 3D reconstruction of serial histological sections. Gd-DTPA is a gadolinium-based MRI agent, respectively (Figure 9B). Due to its paramagnetic properties, the T1 relaxation rate of blood is reduced resulting in contrast enhancement. For contrast enhanced imaging 0.6 mmol/kg are intravenously injected into the tail vein of $LDLR^{-/-}$ mice.

2.2 In vitro Evaluation of Imaging Agents

2.2.1 Evaluation of Neutrophil Elastase FAST™ 680

The enzyme elastase is stored in granules of neutrophils. Murine and human neutrophils are isolated followed by stimulation and incubation with the NIRF agent to prove if the fluorescent imaging agent is specifically cleaved by elastase. Additionally, blocking experiments are performed to demonstrate specificity of the contrast agent.

2.2.1.1 Isolation of Murine Neutrophils

Mouse bone marrow is a reservoir for neutrophils. To isolate and purify neutrophils from mouse bone marrow, healthy *LDLR*$^{-/-}$ mice were euthanized. Femur and tibiae were removed, the remaining skin and muscles were pulled off and the femur was separated from the tibia at the knee joint. The end of the bones was cut off using a scalpel.

With a 26 gauge needle and a 10 ml syringe filled with 10 ml of 1% bovine serum albumin (A7906 - Sigma Aldrich, St. Louis, USA) in phosphate buffered saline (1% BSA/PBS) each bone was flushed from both ends of the bone shafts into a 50 ml falcon tube. The single cell suspension was passed through a Falcon® 70 µm cell strainer (BD Biosciences, Bedford, USA).

For cell counting trypan blue (T8154, Sigma Aldrich, St. Louis, USA) was used. Trypan blue differentiates between live and dead cells. The trypan blue dye passes through cell membrane of dead cells, but not through intact cell membranes.

For counting a cell aliquot was 1:1 diluted with trypan blue and the viable cells were counted using a Neubauer improved haemocytometer. Each square was counted and the mean cell count was calculated. To calculate the total cell number the following formula was used:

N (cells/ml)= mean cell count x 10 000 x dilution factor x volume

Subsequently, the bone marrow cell suspension was centrifuged (500 g, 10 min) and the cell pellet was resuspended in 1% BSA/PBS with a final concentration of $10x10^6$ cells/ml.

2.2.1.2 Separation of Neutrophils by Density Gradient Centrifugation

To separate neutrophils the bone marrow cell suspension was processed by density gradient centrifugation. The density gradient was prepared in a 15 ml falcon tube. First, 5 ml Histopaque®-1119 (11191, Sigma Aldrich, St. Louis, USA, density 1.119 g/ml) was placed in a falcon tube. Secondly, 3 ml Histopaque®-1077 (10771, Sigma-Aldrich, St. Louis, USA, density 1.077 g/ml) was overlaid on Histopaque®-1119. The final step is the overlay of the bone marrow cell suspension on top of Histopaque®-1077 as shown in Figure 10. Depending on the cell count 2-5 ml of bone marrow cell suspension was overlaid.

The density gradient centrifugation was started with 700 g for 30 minutes (min) and without break. After centrifugation mononuclear cells were collected with a pipette at the upper layer of Histopaque®-1077. Neutrophils were collected at the visible interface of both Histopaque® layers (Figure 10).

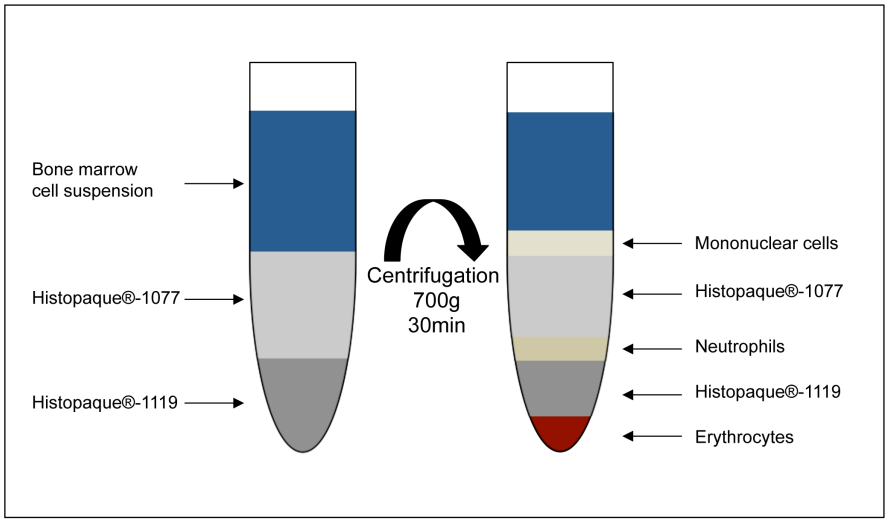

Figure 10 Separation of neutrophils by density gradient centrifugation. After density gradient centrifugation the neutrophil cell layer is easily visible in the interface between Histopaque®-1077 and Histopaque®-1119.

Each cell suspension, mononuclear cells and neutrophils, were transferred into a new 15 ml falcon tube and were washed two times with 5 ml 1% BSA/PBS. After resuspension in the volume, which was laid on the density gradient, cells were counted.

One part of the bone marrow cell suspension was kept for flow cytometry analysis. Therefore, a red blood cell lysis is necessary. The bone marrow cell suspension was resuspended in 3 ml red blood cell lysis buffer (420301, Biolegend, San Diego, USA).

The lysis was stopped after 15 min by adding the double amount of 1% BSA/PBS. The cells were washed twice with 1% BSA/PBS and counted.

2.2.1.3 Isolation of Human Neutrophils

Human neutrophils were isolated from venous blood of healthy volunteers. Venous blood was collected in heparin tubes. To obtain neutrophil cell suspensions, whole blood was diluted 1:1 with 1% BSA/PBS and 6 ml were laid over the Histopaque®-1119 and Histopaque®-1077 density gradient and processed as described above. After collecting neutrophils, the cell suspension was washed two times with 1% BSA/PBS, and a red blood cell lysis was conducted (see chapter 2.2.1.2).

2.2.1.4 Flow Cytometric Analysis of Cell Suspensions

Flow cytometry is a methodology to characterize cells by size, granularity, and protein expression. The cell suspension is hydrodynamically passed through a nozzle. In this way cells pass a set of laser beams one cell at a time. Each cell scatters light, which is detected by detectors: the forward side scatter (FSC) for cell size and the sideward scatter (SSC) for granularity of cells.

Additionally, the emission of light by laser-activated fluorochromes is detected. Fluorescence-labeled antibodies are used to examine and distinguish different cell populations by expression of different cell markers. The measured signal is converted into digital information and can be visualized and analyzed with specific software such as BD FACS-Diva™ (BD Bioscience, Bedford, USA) and FlowJo™ (Tree Star Inc, Ashland, USA).

The emission spectra of fluorochromes overlap partially. Therefore, a compensation of overlaps must be conducted by measuring single stains of each fluorophore used. For surface cell marker staining up to 50.000 cells of each cell suspension were resuspended with 1% BSA/PBS including the listed fluorescence-conjugated antibodies (Table 2). The mixture was incubated for 20 min on ice. After one washing cycle with 1% BSA/PBS the cells were characterized with a FACS Canto II flow cytometer and followed by data analysis with FlowJo™ v10.1r5.

Table 2 Fluorescence conjugated antibodies for flow cytometry.

Specificity	Clone	Source	Working Dilution
CD45-APC-Cy7	30-F11	BD Bioscience, Bedford, USA	1:500
CD11b-V500	M1/70	BD Bioscience, Bedford, USA	1:100
Ly6G-V450	1A8	BD Bioscience, Bedford, USA	1:100

2.2.1.5 In vitro Activation of Neutrophil Elastase FAST™ 680 Agent

After isolation and purification of human and mouse neutrophils, in vitro activation experiments of the NIRF agent Neutrophil Elastase FAST™ 680 were performed to determine cleavage kinetics, sensitivity, and specificity of the probe. Experiments were carried out in 96-well plates with black sides and bottom in 100 µl/well at 37 °C for both, human and mouse neutrophils. For dose-response experiments 50.000 cells/well were lysed with 0.01% Triton X (Triton X100, Sigma Aldrich, St. Louis, USA) and incubated with different concentrations (0.5 µM, 1 µM, 5 µM, 10 µM) of Neutrophil Elastase FAST™ 680. The fluorescent intensity was monitored at several time points at excitation/emission wavelengths of 663/690 nm using a fluorescence plate reader (Infinite® M1000 pro, TECAN, Männedorf, Switzerland). To analyze probe cleavage kinetics, the Michaelis constant (K_m) was calculated using the Michaelis-Menten equation under consideration of determined reaction rates under different substrate concentrations, and half maximal inhibitory concentration (IC_{50}) of Sivelestat was determined.

To prove how specific the probe is cleaved by elastase, blocking experiments were additionally conducted with Sivelestat (S7198, Sigma-Aldrich, St. Louis, USA). For blocking experiments 50.000 cells/ml were lysed with 0.01% Triton X and incubated with different concentrations of Sivelestat (0.01 nM - 2000 nM) for 30 min. Afterwards 5 µM of the NIRF agent was added and processed as described above.

For stimulation experiments, 100.000 cells/well were treated with Phorbol-12-myristate 13-acetate (PMA) in combination with Ionomycin as stimulation agent or N-Formyl-Met-Leu-Phe (fMLP) as stimulation agent. Used concentrations are described in Table 3. Each stimulation set up was incubated with 5 µM Neutrophil Elastase FAST™ 680. The fluorescent intensity was measured over a timeframe of 1.5 h.

Table 3 Composition of neutrophil stimulation.

Stimulation agent	Source	Stock Solution	Final Concentration
Phorbol-12-myristate 13-acetate (PMA)	P8139 Sigma-Aldrich, St. Louis, USA	1 mg/ml	0.5 µg/ml, 1µg/ml
Ionomycin	I0634 Sigma-Aldrich,St. Louis, USA	1 mg/ml	
N-Formyl-Met-Leu-Phe (fMLP)	F3506 Sigma-Aldrich,St. Louis, USA	1 mg/ml	1 µg/ml, 10 µg/ml

For each experiment the fluorescent intensity of the non-activated NIRF agent was measured and defined as background intensity. The background intensity is subtracted of the fluorescent intensity afterwards.

2.2.2 Evaluation of Magnetic Resonance Contrast Agents

MR imaging agents are characterized by their relaxivity. The relaxivity of a contrast agent is the ability to change the relaxation rate of a nearby water proton spin as a function of concentration. The relaxivity of a contrast agent depends on the field strength, the temperature and the solution (i.e. saline, plasma) in which the agent is dissolved.

Relaxivity measurements were performed for Gadofluorine P and Gd-DTPA in 0.9% saline solution (B. Braun, Melsungen, Germany) and human blood serum. For each MRI contrast agent final concentrations of 0.1 mM, 0.5 mM and 1.0 mM in saline and serum were obtained by serial dilution. T1 values of each sample were measured at field strengths of 1, 3 and 7 Tesla (T).

Measurements at 1 Tesla were conducted in a solid state nuclear magnetic resonance spectrometer (Spinsolve® Carbon, Magritek, Aachen, Germany). Prior to starting the measurements, a shim of the magnetic field was performed and the samples were left to equilibrate to the bore temperature, which was 28.5 °C. Proton-spectra were acquired after adjusting the repetition times and number of repetitions

individually to each concentration in order to determine T1 values. Repetition times were between 7 and 15 seconds (s). Obtained spectra were analyzed with MestReNova® (MestReLab Research, Santiago de Compostela, Spain), followed by performing a peak fitting and T1 values were calculated based on the fitted curve.

3 T measurements were performed at a clinical imaging system (Ingenia 3.0T; Philips Healthcare, Best, Netherlands) with a modified Look-Locker inversion recovery sequence using the following parameters: Field of view (FOV) 140 x 140 mm, matrix 112 x 112, slice thickness 3 mm, repetition time (TR) 5.0 ms, flip angle 5°. The measurement was conducted at 22°C.

Measurements at 7 T were performed on a small animal scanner (Discovery™ MR901, GE Healthcare, Chalfont St. Giles, United Kingdom) with a Look Locker sequence. Specific sequence parameters were as followed: FOV 30 x 30 mm, matrix 128 x 128 (in-plane resolution 234 µm), slice thickness 1 mm, TR/TE 5.1 ms/1.3 ms, flip angle 8°. For T1 estimation Look-Locker data analysis was performed using an open-source software tool for the generation of relaxation time maps in (MRmap v1.4) [143]. T1 images were calculated from DICOM source images based on a 3-parameter Levenberg-Marquardt curve fitting procedure with a correction for read-out-induced attenuation of the relaxation curve[144].
Samples were measured three times and a mean of T1 values for each concentration was calculated followed by calculation of the relaxation rate R_1 (1/T1). After plotting R_1 values of different concentrations the slope was calculated, which represents the relaxivity r_1.

2.3 In vivo Animal Experiments

For all experiments *LDLR*$^{-/-}$ *mice* (B6.129S7-Ldlrtm1Her/J, obtained from The Jackson Laboratory) were used. At the age of 14 to 15-weeks *LDLR*$^{-/-}$ mice were placed on a western type high fat diet (21% fat, 0.15% Cholesterol, 19.5% Casein; Altromin, Lage, Germany) for 4-25 weeks, depending on the experimental setup. *LDLR*$^{-/-}$ mice fed a normal chow served as control group.
All animal experiments were approved by local authorities (55.2.1.54-2532-115-13, Regierung von Oberbayern, Munich, Germany) in accordance with the German animal protection law.

2.3.1 Fluorescence Molecular Imaging Protocol

To target elastase activity with fluorescence molecular imaging *LDLR*$^{-/-}$ mice were placed for 4, 8 or 12 weeks on HFD. *LDLR*$^{-/-}$ mice fed a normal chow served as control group. Before each imaging time point (0, 4, 8, 12 weeks of HFD) the chest was shaved followed by chemically depilation (Veet®, Reckitt Benckiser, Heidelberg, Germany) as the fur is significantly absorbing and scattering the NIRF light. 100 µl of Neutrophil Elastase 680 FAST™ was injected via tail vein injection (4 nmol/100µl) 4h prior to imaging. To improve segmentation of the chest XCT images, an intravascular CT contrast agent (ExiTron nano 12000™, Miltenyi Biotec, Bergisch Gladbach, Germany) was immediately injected (100 µl/25g mouse) before scanning. Mice were anesthetized by isoflurane inhalation (isoflurane 1.5–2.5% vol, plus 2 L O_2) during the imaging measurement.

All mice were imaged using a FMT-XCT hybrid imaging system as described in chapter 1.3.1. These measurements were conducted in collaboration with Xiaopeng Ma, Institute of Biological and Medical Imaging, Helmholtz Zentrum München, Germany. Xiaopeng Ma performed the measurements and analyses.

The system combines two imaging modalities, namely FMT and XCT, for imaging small animal disease models. Co-registered XCT images with high resolution can provide anatomical information for FMT, which improves the FMT three-dimensional functional and molecular reconstruction performance in a fundamental way[93]. For data acquisition, each mouse was first illuminated by a 680 nm laser in a 360° trans-illumination mode. Excitation and emission images were both acquired at 20 equally spaced gantry locations by using a scientific CCD camera cooled at -80°C with two different sets of filters placed in front of it (one for excitation and one for emission). Around 30 different positions of laser illumination in the region of interest (ROI) were calculated automatically by first-acquired white light reference images at each gantry location. Furthermore, the mouse was scanned by using the integrated XCT system, which collected projections with a field of view of 360°. The current and energy of the X-ray tube was 450 µA and 80 kV. After FMT-XCT data acquisition, three-dimensional fluorophore distribution was reconstructed by using sparse linear equations and sparse least squares methods and XCT anatomical information as prior[145]. Anatomical images were reconstructed by filtered back projection method and then semi-automatically segmented based on the gray-scale slices. Different

optical parameters (absorption coefficients and scattering coefficients) were assigned to different organs for every mouse. Then, FMT inversion was performed iteratively to locate the fluorescent distribution. To quantify and statistically analyze the FMT reconstruction, mean values of the ROI of fluorescence intensities (around 5 slices, 1 mm interval) were calculated afterwards.
After each imaging time point mice were euthanized for further ex vivo analysis as described in chapter 2.4.

2.3.2 Magnetic Resonance Imaging Protocol

Magnetic resonance imaging was performed on a horizontal bore 7 T small animal scanner (Discovery™ MR901, GE Healthcare, Chalfont St. Giles, United Kingdom) equipped with a 300 mT/m standard high-field gradient system and a 72 mm inner diameter $^{1}H/^{13}C$ quadrature birdcage resonator (Rapid Biomedical®, Rimpar, Germany). The birdcage resonator was only used for transmission while signals were received by a 2-channel surface coil placed around the heart.

2.3.2.1 Imaging Protocol for Plaque targeting

To target aortic plaques over time with Gadofluorine P and MR imaging *LDLR*$^{-/-}$ mice were placed on HFD for 4, 10, 15 and 20 weeks. Image acquisition was performed after each time point of HFD. A kinetic study was conducted after 20 weeks of HFD to define the peak of enhancement. For imaging procedures mice were anesthetized by general inhalation anesthesia (isoflurane 1.5–2.5% vol, plus 2 L O_2).

Image acquisition was performed under free-breathing conditions and with prospective electrocardiography (ECG) triggering using a small animal monitoring and gating system (Rapid Biomedical®, Rimpar, Germany). Electrodes for detection of the ECG signal were placed at the front paws. During imaging the animal core temperature was maintained at 38 °C using an MR-compatible air-heating system. After acquisition of standard scout scans, slices were planed in line with the aortic arch and perpendicular to the aortic root to perform imaging scans. Gadofluorine P was injected intravenously at a dose of 0.2 mmol/kg body weight via the tail vein. A T1 weighted inversion recovery sequence was performed immediately after contrast agent injection for anatomical depiction and to proof successfully contrast agent injection. Therefore, a segmented inversion-recovery fast gradient echo sequence was performed using the following parameters: FOV 30 x 30 mm, matrix 192 x 192

(in-plane resolution 156 µm), slice thickness 1 mm, TR 7.6 ms, echo time (TE) 3.1 ms, flip angle 60°, 4 lines/RR interval, 2 scans. Delay after inversion was set to 350 ms. Cardiac gating was set to give an effective TR of 1 s from one inversion to the next. Consequently, single-slice T1 mapping was applied in the same slice geometry used before to quantify accumulation of Gadofluorine P[146]. T1 mapping was performed at different time points for the kinetic study and thus 30 min after contrast agent injection for each time point of HFD. Therefore, an inversion prepared prospectively ECG-gated CINE Look-Locker sequence was used. Immediately after the ECG-trigger signal, it applies a non-selective adiabatic inversion pulse, which is followed by a fast spoiled gradient echo segmented k-space acquisition. Depending on the heart rate 2–3 RR intervals were used for signal acquisition while 2–3 intervals were left for T1 relaxation leading to an effective TR of ~3 s from one inversion to the next. Specific sequence parameters are as follows: FOV 30 x 30 mm, matrix 128 x 128 (in-plane resolution 234 µm), slice thickness 1 mm, TR/TE 5.1 ms/1.3 ms, flip angle 8°, 4 lines/RR interval, 4 scans, total scan time 15 min.

For T1 estimation Look-Locker data analysis was performed using an open-source software tool for the generation of relaxation time maps (MRmap v1.4)[143]. T1 images were calculated from DICOM source images based on a 3-parameter Levenberg-Marquardt curve fitting procedure with a correction for read-out-induced attenuation of the relaxation curve[144].

After completion of the imaging study mice of each group were euthanized and the aortas were excised, snap frozen in liquid nitrogen and prepared for further analysis.

2.3.2.2 Protocol for Contrast Enhanced Imaging of the Aortic Arch

Contrast enhanced imaging of the aortic arch provides information about the anatomical shape of the aortic arch, which are necessary to develop a 3D reconstruction of serial histological sections. Image acquisition was conducted with healthy *LDLR*$^{-/-}$ mice. For imaging procedures mice were anesthetized by general inhalation anesthesia (isoflurane 1.5–2.5% vol, plus 2 L O_2). Image acquisition was performed under free-breathing conditions and with ECG triggering using a small animal monitoring and gating system (Rapid Biomedical®, Rimpar, Germany). Electrodes for detection of the ECG signal were placed at the front paws.

During imaging the animal core temperature was maintained at 38 °C using an MR-compatible air-heating system.

After acquisition of standard scout scans, axial slices were planned covering the heart and aortic arch region to perform angiography. Gd-DTPA was injected at a dose of 0.1 mmol/kg body weight via the tail vein and imaging was started immediately after injection. For angiography assessment, a 3D segmented inversion-recovery fast gradient echo sequence was performed using the following parameters: FOV 30 x 30 mm, matrix 512 x 512, in-plane resolution 59 µm, slice thickness 0.25 mm, TR/TE 8.38ms/1.972 ms, flip angle 25°, 2 scans.
After imaging mice were euthanized and the aortic arch including heart was perfusion-fixed and harvested as described in 2.4.4.1.

2.4 Ex vivo Analyses

2.4.1 Whole-body Cryosectioning

To localize and further characterize the in vivo imaged fluorescent signal of the NIRF elastase agent whole-body cryosectioning was performed. This method provides slice images of the mouse body in the same orientation (transverse plane) as FMT-XCT data acquisition. The anatomy of the mouse as well as the NIRF reagent distribution in the mouse body is shown.
After each time point of HFD, mice were euthanized and frozen at -80 °C. For cryoslicing, the mouse torso was embedded in a 25:1 mixture of Optimal Cutting Temperature medium and India Ink. Cryoslice imaging of the mice was performed using a multispectral imaging system combined with a cryomicrotome[104]. Transversal slices of the thorax 150 µm apart were acquired. After each slice a planar colored image and planar fluorescence image (excitation 680 nm) were taken using a filtered white light source and a sensitive CCD camera. Xiaopeng Ma, Institute of Biological and Medical Imaging, Helmholtz Zentrum München, Germany performed the analyses of cryoslice images afterwards.

2.4.2 Fluorescence Microscopy of Cryosections

To confirm that the fluorescence signal originates from the arterial wall fluorescence microscopy of cryosections was performed. Furthermore, the precise localization of the elastase-targeted NIRF imaging agent within the arterial wall can be assessed.

After whole-body cryosectioning, the cryoslices (with a thickness of 10 µm) of the ascending aorta and the aortic arch were placed on adhesive-glass slides (SuperFrost plus, Thermo Fisher Scientific, Waltham, USA). Cell nuclei were counterstained with 4',6-diamidino-2-phenylindole (DAPI) and embedded in ProLong Gold (Thermo Fisher Scientific, Waltham, USA). Sections were imaged using a fluorescence microscopy using appropriate filters (Cy5.5 filter and DAPI) or brightfield (ZEISS Axio Imager 2, ZEISS ZEN analysis software, Jena, Germany).

2.4.3 Matrix-assisted Laser Desorption/Ionization Imaging Mass Spectrometry

MALDI-IMS offers new possibilities to assess spatially resolved quantification of MRI contrast agent directly in the tissue following in vivo application[121]. Detection and quantification optimization for Gadofluorine P was performed as described previously[147].

After imaging *LDLR*$^{-/-}$ mice with the MR contrast agent Gadofluorine P (Chapter 2.1.2) the aorta connected to the heart was shortly perfused with PBS, excised and snap frozen in liquid nitrogen.

Sectioning and MALDI-IMS experiments as well as analysis was carried out at Research Unit Analytical Pathology, Institute of Pathology, Helmholtz Zentrum München and was performed by Katharina Huber.

Transversal cryosections (12 µm thickness) of the aortic root connected to the aortic arch were prepared and mounted onto conductive Indium-Tin-Oxide glass slides (Bruker Daltonik GmbH, Bremen, Germany), which were pre-coated with 1:1 Poly-L-Lysine (P8920, Sigma-Aldrich, St. Louis, MO, USA) and 0.1% Nonidet™ P-40 (21-3277 SAJ, Sigma-Aldrich, St. Louis, MO, USA).

To quantify Gadofluorine P accumulation in atherosclerotic plaques a standard curve of the contrast agent was prepared additionally on each slide. For this purpose liver cryosections of mice, without Gadofluorine P injection, were mounted on the Indium-Tin-Oxide slides. 0.5 µl of serially diluted Gadofluorine P concentrations ranging from 0.5 to 0.01 mg/ml were spotted on each liver. To obtain digital images for coregistration, aortic root sections were dried at room temperature and scanned using a flatbed scanner.

Matrix solution, composed of 7 g/l cyano-4-hydroxycinnamic acid (C2020, Sigma-Aldrich, St Louis, MO, USA) in 70% methanol and 0.2% trifluoroacetic acid (Applied

Biosystems™, Darmstadt, Germany), was applied using ImagePrep™ spray device (Bruker Daltonik GmbH, Bremen, Germany).

MALDI time of flight (TOF) imaging measurements were carried out at a spatial resolution of 70 µm using an Ultraflex III MALDI TOF mass spectrometer (Bruker Daltonik GmbH, Bremen, Germany) in positive reflector mode with a sampling rate of 1.0 GS/s. A total of 200 laser shots were accumulated for each position measured. For data generation, the software packages FlexImaging 4.0® and FlexControl 3.0® (Bruker Daltonik GmbH, Bremen, Germany) were used.

After mass spectrometry measurements, matrix was removed with 70% ethanol and sections were stained with Elastica-van-Gieson (EvG) staining (Morphisto® Evolutionsforschung und Anwendung GmbH, Frankfurt am Main, Germany) according to the manufacturer´s protocol. The stained tissue slides were scanned using a digital slide scanning system (MIRAX DESK, ZEISS MicroImaging GmbH, Jena, Germany). Images were imported to FlexImaging 4.0® software (Bruker Daltonik GmbH, Bremen, Germany) and merged with the mass spectrometry datasets.

2.4.4 Tissue Preparation of Isolated Organs

2.4.4.1 Tissue Fixation and Paraffin Embedding

For histological analyses of atherosclerotic plaques in situ perfusion and fixation must be performed.

After euthanizing the mouse, the abdomen was opened and an intracardiac puncture into the left ventricle was made to withdraw blood. To release the perfusate the right atrium was cut off. Afterwards perfusion was made with a 26 gauge needle and 10 ml syringe filled with PBS until all blood was removed. This procedure was repeated for fixation with 4% Formalin for at least 5 min. Subsequently, the aortic arch (including brachiocephalic artery, left carotid artery and left subclavian artery) fixed to the heart was dissected by cleaning of extraneous fat. Additionally, liver and spleen were harvested. The harvested organs were postfixed in 4% Formalin over night. Each tissue was then dehydrated through a series of graded ethanol solutions to displace water and then infiltrate with paraffin. Therefore, the heart and aortic arch are placed in a small biopsy capsule covered with filter paper. The biopsy capsule is transferred to the processing cassettes. With this construction the lumen of the vessel will be

conserved. A tissue processor of the Institute of Pathology, Klinikum Rechts der Isar, München was used for dehydration process and paraffinization.

Two different approaches were used for embedding of the aortic arch to produce histological sections. In order to quantify the progression of atherosclerosis and localize neutrophils in atherosclerotic plaques the heart and the aortic arch were separated in 3 parts: the heart for sectioning the aortic root, the ascending part of the aortic arch including the brachiocephalic artery, the arch including the left carotid artery and the left subclavian artery. Each vessel part was embedded in paraffin in a way to achieve cross sections of the vessel.
To develop a 3D reconstruction of the aortic arch based on serial histological sections the heart was removed and the whole aortic arch including the bifurcations was embedded in paraffin.

2.4.4.2 Micro-computed Tomography of the Aortic Arch Embedded in Paraffin

Deformations and shrinkages of the aortic arch occur during tissue preparation, especially during fixation and dissecting of the aortic arch. Imaging of the aortic arch embedded in paraffin with micro-computed tomography provides detailed information about the occurred deformations for precise 3D reconstruction of the aortic arch based on histological images.
All measurements were carried out at TUM Institute of Medical Engineering / Chair for Biomedical Physics E17, Department of Physics, Technische Universität München. Jonathan Schock kindly performed the imaging scans.

Versa XRM-500™ (ZEISS X-ray microscopy, Pleasanton, CA, USA), an X-ray microscope imaging system with spatial resolution in the micrometer scale, was used to perform imaging of the paraffin block including the murine aortic arch.
The system, consisting of an X-ray tube, a sample stage and a detector unit, has an additional optical stage, allowing different magnifications of the scintillator screen onto the CCD.

The µCT measurement was made in air, without further filtering, with a 4.0x objective and the parameters listed in the following table (Table 4).

Table 4 Parameters for µCT measurement.

Projections	Energy source (kV)	Power (W)	Exposure (s)	Resolution (µm/Voxel)	Time of measurement (h)
1601	60	4.5	40	2.3576	14

The distance between source and sample was 80.00 mm and between sample and detector 35.00 mm.

2.4.4.3 Sectioning

Sectioning was conducted at a Leica Microtome (RM 2255, Leica Biosystems, Nussloch, Germany) using microtome blades A35 (FEATHER Safety Razor, Osaka, Japan).

For histochemical staining SuperFrost® slides (Menzel GmbH, Braunschweig, Germany) were used. Slices were sectioned with a thickness of 5 µm slice.

Menzel Superfrost Ultra Plus® slides (VWR International, Darmstadt, Germany) coated with Poly-L-Lysine in order to prevent detachment of the tissue section were used for immunohistochemical staining (Neutrophil staining). These slides were pretreated with 0.1% Poly-L-Lysine solution (P8920, Sigma-Aldrich, St Louis, MO, USA) and then incubated overnight at 56 °C for 1 h. Slices for neutrophil staining were sectioned with a thickness of 2.5 µm, 25 µm apart.

2.4.5 Histo- and Immunohistochemistry

After sectioning slices placed on glass slides were dried at 56 °C over night.

For deparaffinization the slides were incubated in xylene for 20 min, followed by isopropanol for 20 min, 96% ethanol for 10 min, 70% ethanol for 10 min, and distilled water for 10 min. Consequently, the slides were processed for staining.

2.4.5.1 Haematoxylin and Eosin Staining

Haematoxylin and eosin (H&E) staining is an overview staining to visualize nuclei, cytoplasm and extracellular tissue. Haematoxylin stains nuclei blue, and the counterstain is made with eosin staining cytoplasm and extracellular tissue in red to pink.

After deparaffinization the slides were incubated with Mayer's haematoxylin for 5-10 min at room temperature. Followed by washing in tap water for 10 min. Afterwards they were incubated with acidified eosin for 5 min and rinsed briefly in tap water and then in ascending alcohol series (70% ethanol, 96% ethanol, isopropanol) followed by xylene.

The slides were mounted with hydrophobic mounting medium (CS703, DAKO, Glostrup, Denmark) and covered with cover slips (Thermo Scientific™ Cover Slips, Thickness 1, Thermo Fisher Scientific, Waltham, USA).

2.4.5.2 Neutrophil Staining

To analyze neutrophil cell count in atherosclerotic plaques immunohistochemical staining protocols were used. The immunochemical procedures carried out in the present protocol were performed with the labeled streptavidin-biotin immunohistochemistry kit (LSAB®2 System-HRP, K0675, Dako, Hamburg, Germany) following the instructions of the manufacturer.

All washing steps in the following protocol were made with Tris(hydroxymethyl)-aminomethan (TRIS) buffer. A stock solution of TRIS buffer (10x) was prepared by adding 60.5 g Trizma® base (T1503, Sigma-Aldrich, St. Louis, USA) and 90 g NaCl (S3014, Sigma-Aldrich, St. Louis, USA) in 1 L distilled water, and adjusting the pH to 7.6 with HCl. TRIS buffer (1x) was then prepared by 1:10 diluting the stock solution (10x) in distilled water. All following steps were performed at room temperature and according to the manufacturer instructions.

After deparaffinization the slides were placed in destilled water. For antigen retrieval sections were then immersed in citrate buffer (2.1 g citric acid monohydrate; 100243, Merck Chemicals GmbH, Darmstadt, Germany) in 1000 ml distilled water; pH 6) and cooked for 7 min in a pressure cooker. After a washing cycle with TRIS buffer (1x) for 3x2 min the endogenous peroxidase was blocked. The slides were treated and incubated for 15 min with 0.3% hydrogen peroxide (30% Hydrogen Peroxid, 107209, Merck Chemicals GmbH, Darmstadt, Germany) and then rinsed with TRIS buffer (1x). Thereafter, the slides were incubated for one hour with Anti-Ly6G antibody (1:200; Purified Rat anti-Mouse Ly6G, Clone 1A8, 551459, BD Biosciences, Bedford, USA). During this procedure, all slides were kept in a humidified chamber, followed by another wash with TRIS buffer (1x) for 3x2 min. Subsequently, all slides were incubated with biotinylated secondary antibody (1:200; Rabbit anti-Rat, E0468, Dako,

Denmark) for 30 min. After washing for 3x2 min all slides were incubated with streptavidin-peroxidase for another 25 minutes, and then followed by rinsing in TRIS buffer (1x) for 3x2 min, respectively. Finally, the chromogenic solution was prepared from 15 µl 3,3'-diaminobenzidine and 750 µl horseradish peroxidase substrate. After incubation for 3-5 min with the chromogen, samples were counterstained with haematoxylin for 20-30 s. Subsequently, dehydration in alcohol series was performed (70% ethanol, 96% ethanol, isopropanol) followed by xylene. Finally, slides were mounted with Dako mounting medium and covered with appropriate cover slips (Thermo Scientific™ Cover Slips, Thickness 1, Thermo Fisher Scientific Gerhard Menzel, Braunschweig Germany).

Mouse spleen tissue was used as positive control for neutrophil staining and processed as described above.

2.4.5.3 Digitization and Morphometry

After staining procedures, all slides were evaluated by microscopy. Digital images were obtained using a microscope (Leica DM 4000 B, Leica Biosystems, Nussloch, Germany) with different magnifications (1.25x, 5x, 10x, 20x, 40x) and Leica Application Suite V4.5 software.

The number of positive stained neutrophils was counted on each section. To quantify the extent of atherosclerosis progression all slides were analyzed by morphometry. The plaque area was measured for each section using the open source software ImageJ[148]. Subsequently, the number of neutrophils per plaque area was calculated.

2.5 Statistical Analysis

Data are represented as mean ± standard deviation (SD). Comparisons over time were analyzed by one-way Analysis of Variance (ANOVA) followed by Bonferroni post-tests for multiple comparisons using GraphPad Prism® Software 6.0 (GraphPad Software, Inc., California, USA). Differences with p-values < 0.05 were considered to be statistically significant.

3 RESULTS

3.1 Outline

This outline will give an overview about the experimental setup carried out in this thesis to gain more insights how imaging approaches can be used to target and visualize atherosclerosis.

The first approach will describe experiments how FMT-XCT imaging can be applied to target elastase, secreted by neutrophils, in atherosclerotic plaques. The NIRF imaging agent, Neutrophil Elastase FAST 680, was first characterized in vitro. Subsequently, an in vivo study with atherosclerotic mice was conducted followed by ex vivo analyses to localize and confirm source of the imaging signal.
The second approach explores how the MR imaging agent, Gadofluorine P, can be used to target atherosclerotic plaques. After the MR imaging agent was characterized by relaxivity measurements, a kinetic study in vivo was performed to define the imaging time point after contrast agent injection. Furthermore, contrast agent accumulation in the course of atherosclerosis was analyzed. To clarify and quantify contrast agent accumulation in atherosclerotic plaques MALDI-IMS was performed.

While these approaches deal with imaging of specific cellular and molecular aspects of atherosclerotic plaques, the third approach examines the application of imaging modalities to create a 3D representation of the murine aortic arch based on serial histological sections. This can be used to visualize the spatial and functional relationship of plaque development and regional cell distributions. Developing an experimental workflow how serial histological sections of the murine aortic arch, respectively images, can be reconstructed to a 3D object was the first step to this goal. The development of the workflow was revised considering technical limitations and was optimized by including imaging modalities such as MRI and CT. The design and development of the workflow was established with healthy mice. The translation to atherosclerotic aortic arches including staining for plaque composition and thereby visualization of functional and cellular relationship of atherosclerosis would be the longtime goal of the presented preliminary results.

3.2 Imaging of Elastase Activity in Murine Atherosclerotic Plaques

This imaging approach aimed to assess an elastase specific, enzymatically activatable contrast agent in a mouse model of atherosclerosis to detect early atherosclerosis with FMT-XCT. The NIRF agent can be activated by neutrophil elastase that is usually stored in neutrophil cytoplasmic granules. As proof of principle in vitro experiments were conducted to determine sensitivity and specificity of the probe. Therefore, neutrophils were isolated and lysed or stimulated, followed by incubation with the contrast agent and measuring of fluorescence intensity. Additionally, blocking experiments were conducted to prove specificity. Subsequently, the probe was evaluated in vivo.

LDLR$^{-/-}$ mice fed a HFD for 4, 8 or 12 weeks were injected with the contrast agent and imaged with FMT-XCT. Mice without atherosclerosis injected with the agent served as control group. Atherosclerotic mice that did not receive the imaging agent were used to control for autofluorescence. After each imaging time point (0, 4, 8, 12 weeks of HFD), mice were euthanized for ex vivo analyses. To confirm the localization of the fluorescence signal ex vivo, cryoslicing was performed along with fluorescence microscopy. Afterwards, histological analysis was performed for the assessment of neutrophils within atherosclerotic lesions.

3.2.1 Elastase Targeted Imaging Agent is Activated by Isolated Neutrophils

We first tested activation of the elastase-specific NIRF agent by neutrophils. Murine neutrophils were isolated from bone marrow and characterized by multi-color flow cytometry. Isolated neutrophils were identified as $CD11b^+Ly6G^+$ cells within $CD45^+$ leukocytes and reached a purity of more than 90% (Figure 11A).

Activation of different concentrations of the NIRF agent by lysed neutrophils was analyzed. Concentration dependent increase of emitted fluorescence was observed over time, using both murine and human neutrophils, corresponding to K_m values of 7.3 µmol/l and 11.2 µmol/l, respectively (Figure 11B, C). Additionally, specificity of the imaging agent was tested by conducting blocking experiments using the selective elastase inhibitor Sivelestat[149] with both mouse and human neutrophils. Dose-response curves after inhibition with different concentrations of Sivelestat are shown in Figure 11D, E. The effectiveness of Sivelestat is shown in inhibition curves (Figure 11F, G) with IC_{50} values of 0.9 nM and 48 nM for murine and human neutrophils, respectively[150].

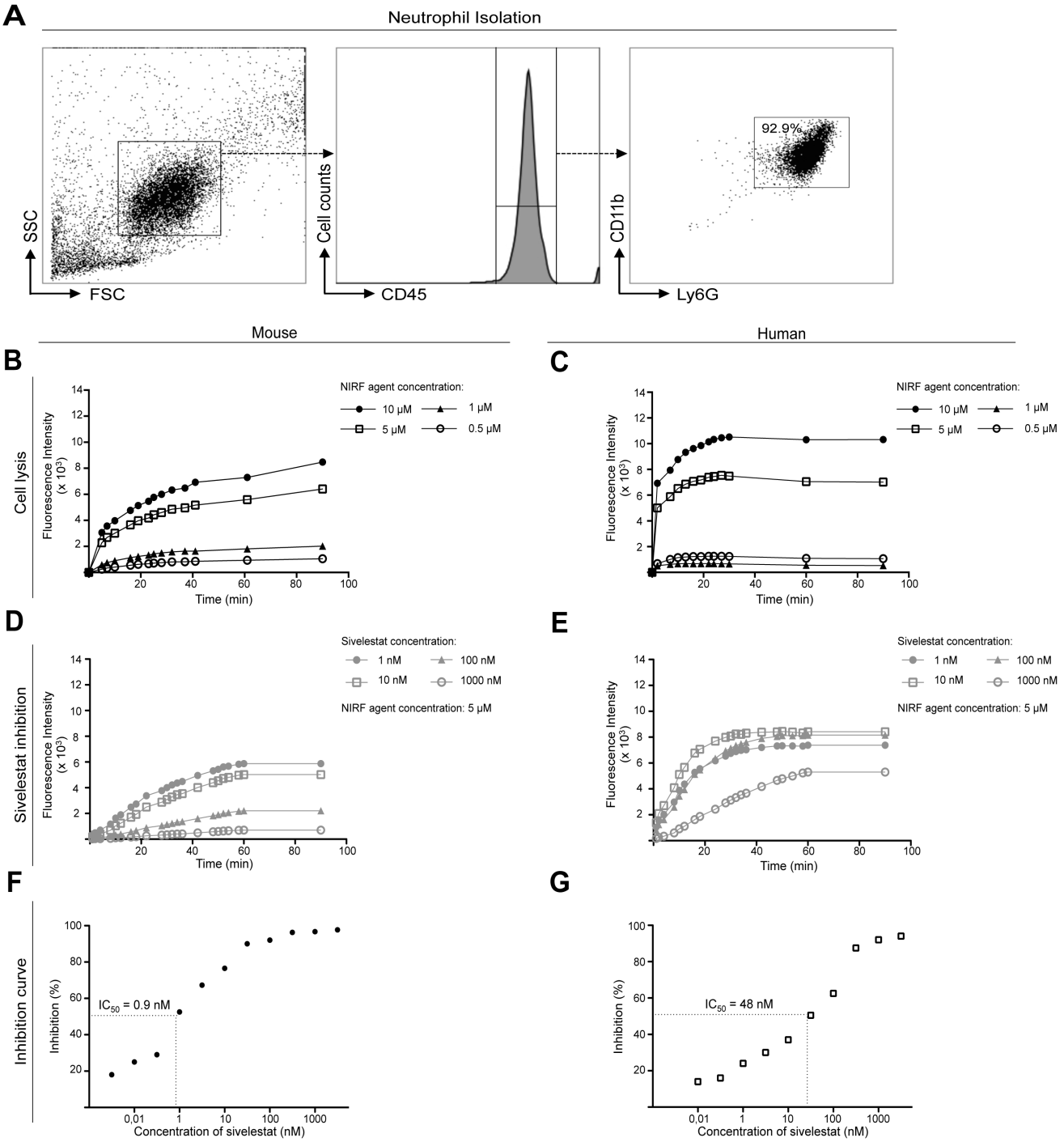

Figure 11 Neutrophil Elastase 680 FAST™ agent is activated by murine and human neutrophils.
(A) Characterization of neutrophils isolated from murine bone marrow by multi-color flow cytometry. Representative gatings are shown. Neutrophils were identified upon their appearance in the FSC-SSC (left panel), staining for CD45 (central panel), and for Ly6G and CD11b (right panel). (B-C) Fluorescence intensity (in arbitrary units) of isolated neutrophils incubated with the NIRF agent. Murine and human neutrophils were lysed with 0.01% Triton X and incubated with different concentrations of the NIRF imaging agent showing a concentration dependency. (D-G) Inhibition experiments with the inhibitor Sivelestat demonstrate specificity of the imaging agent. Enzyme activity after incubation with different concentration of Sivelestat was measured over time (D, E) and the resulting blocking curves are presented (F, G). Previously published in Glinzer et al.[150].

In vivo, intracytoplasmatic granules are released from neutrophils upon stimulation. Therefore, activation of the elastase-targeting NIRF agent by neutrophils stimulated with different concentrations of PMA/Ionomycin or fMLP was assessed (Figure 12 A-D). Indeed, the probe was rapidly activated by PMA/Ionomycin-stimulated murine neutrophils in a concentration-dependent manner (Figure 12A), while fMLP-activation of murine neutrophils showed less potent activation of the fluorescent probe (Figure 12C). No activation of the probe was detected in unstimulated neutrophils (Figure 12 A, C). Human neutrophils activated with PMA/Ionomycin generated a fluorescent intensity that was twice as high when compared to murine neutrophils. fMLP challenging of human neutrophils only marginally increased the fluorescence intensity of the activated probe when compared to non-activated neutrophils, which served as a control (Figure 12D). Of note, already non-activated control human neutrophils showed a mild increase of emitted fluorescence when incubated with the NIRF agent over time, which may reflect low levels of spontaneous activation (Figure 12B)[150].

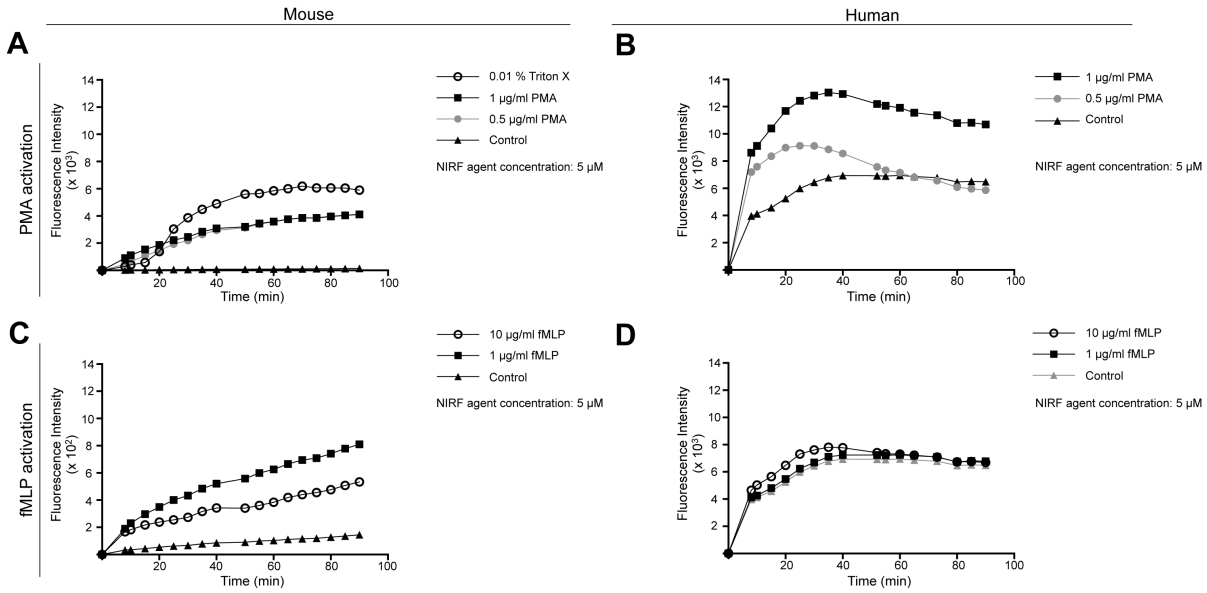

Figure 12 Elastase release after neutrophil stimulation. Intact cells were stimulated with PMA/Ionomycin (A, B) or fMLP (C,D), and incubated with 5 µM of the NIRF imaging agent. To compare cell lysis and stimulation, the emitted fluorescence of Triton X lysed cells is shown for PMA activation of murine neutrophils (A). Previously published in Glinzer et al.[150].

Taken together, the evaluated elastase-targeted fluorescent agent shows specificity and can be activated by exposure to both murine and human neutrophil contents after lysis as well as by activated neutrophils in a concentration dependent manner.

3.2.2 In vivo FMT-XCT of Elastase Activity in Atherosclerotic *LDLR*$^{-/-}$ Mice

The ability of the fluorescent agent to be cleaved and activated in vivo was investigated in atherosclerosis prone *LDLR*$^{-/-}$ mice that develop early atherosclerotic lesions in the aortic root and aorta within 4 weeks after start of a HFD. Mice were put on a HFD for 4, 8 or 12 weeks. At each time point, mice were injected with Neutrophil Elastase 680 FAST™ and imaged by hybrid FMT-XCT. An increased fluorescence signal was observed in atherosclerotic mice after injection with the elastase-targeted NIRF agent, and hybrid contrast-enhanced X-ray CT enabled co-localization of the fluorescence signal predominantly to the aortic root and arch. Control mice without atherosclerosis showed only weak and unspecific fluorescence signal after injection with the probe (Figure 13A). The mean fluorescence intensity, calculated for the ROI (root and aortic arch), peaked at 4 weeks of HFD and decreased slightly at 8 and 12 weeks of HFD compared to control mice without atherosclerosis (Figure 13B). Statistical analysis showed a significant difference between 0 vs. 4 weeks of HFD ($p= 0.0007$) and 0 vs. 8 weeks of HFD ($p= 0.0428$). To rule out a major contribution of autofluorescence to this signal, mice were additionally imaged after 4 weeks of HFD without injection of the NIRF contrast agent. However, captured autofluorescence in these mice proved to be negligible (Figure 13B). Furthermore, mice injected with the NIRF agent before the initiation of HFD, without any atherosclerosis, showed only moderate background fluorescence, attributable to unspecific activation within the circulation (Figure 13B)[150].

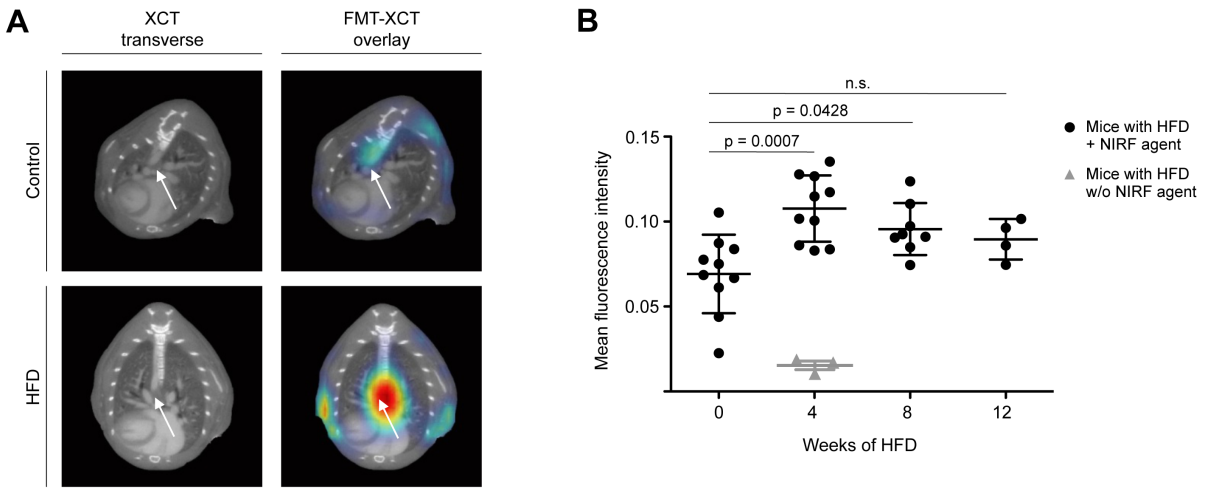

Figure 13 In vivo FMT-XCT of elastase activity in the course of atherosclerosis. (A) In vivo FMT-XCT imaging of control (*LDLR*$^{-/-}$ on normal chow) and atherosclerotic mice (*LDLR*$^{-/-}$on HFD). XCT images (left) depict anatomical information. FMT images (right) demonstrating elastase activity in vivo 4 h after injection with the NIRF imaging agent. (B) The mean value of the fluorescence intensity of the ROI was calculated for each time point, as indicated. Grey colored dot plot represents autofluorescence in atherosclerotic mice after 4 weeks of HFD, not injected with the NIRF agent (p<0.05). Previously published in Glinzer et al.[150].

These data indicate that elastase activity can be detected with the elastase-targeting NIRF agent in the region of the aortic root and arch. Nevertheless, the origin of the fluorescent signal must be clarified, which is achieved with the following experiments.

3.2.3 Confirmation of Fluorescence Elastase Signal in the Aortic Arch

To confirm that the fluorescent signal emitted from the elastase-targeted NIRF agent originates from the aorta of atherosclerotic mice, whole body cryoslicing was performed, which provides an increased spatial resolution (20µm) of the emitted fluorescence compared to in-vivo FMT. Representative cryo-images of the arch of control and atherosclerotic mice injected with the NIRF agent are shown, as well as images of mice not injected with the probe depicting background autofluorescence (Figure 14A). Fluorescent ratios of the aortic arch were calculated for each time point. Similar to results obtained in vivo, signal intensities in these areas increased after initiating of HFD and peaked at 4 weeks, and decreased in the later course of atherosclerosis (Figure 14B) (0 vs. 4 weeks HFD p= 0.0286, 0 vs. 8 weeks HFD p= 0.0498). Autofluorescence intensities of mice at 4 weeks of HFD not injected with the NIRF agent were again low (Figure 14B).

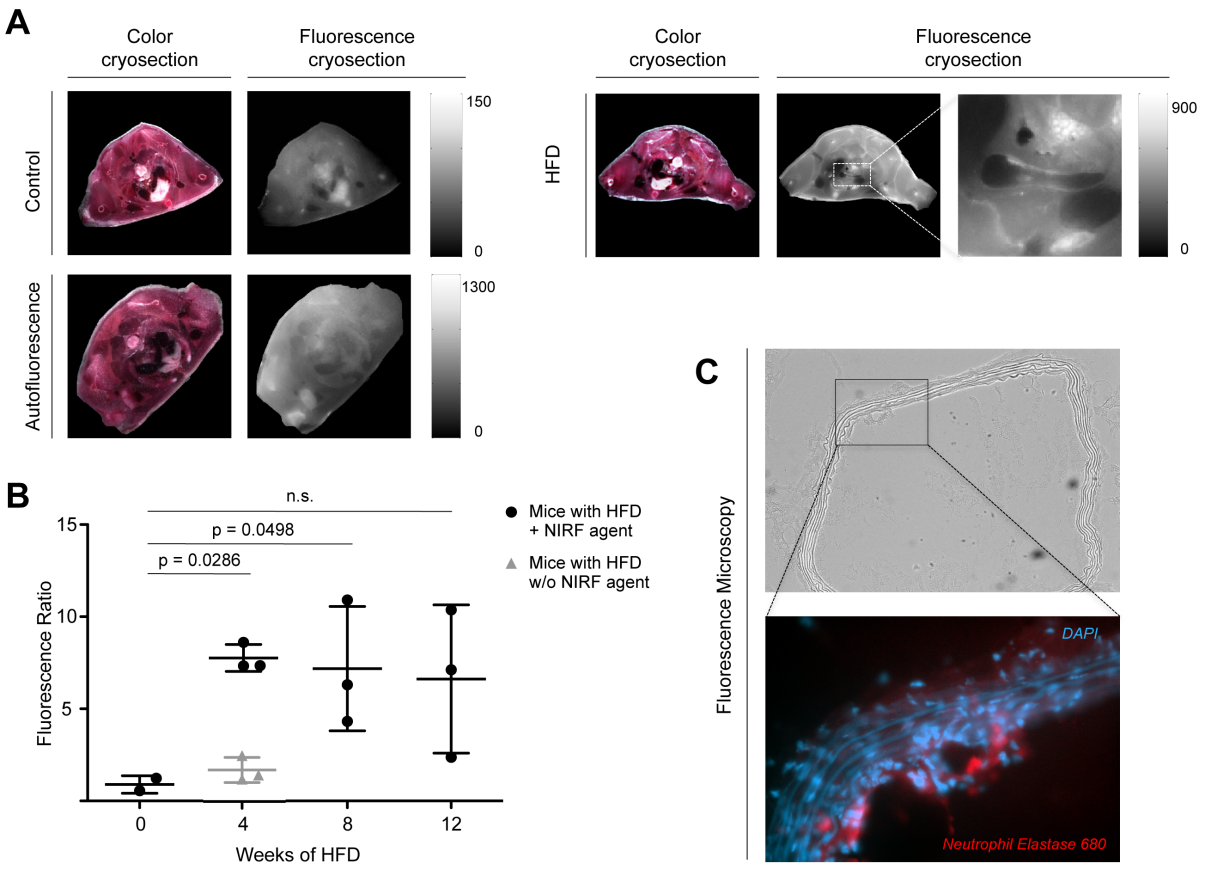

Figure 14 Fluorescence imaging of NIRF imaging agent in whole body cryosections of atherosclerotic mice. (A) Representative images of cryosections in the plane of the aortic arch of control (*LDLR*$^{-/-}$ on normal chow) and atherosclerotic mice (*LDLR*$^{-/-}$ on HFD) as well as autofluorescence of atherosclerotic mice (mice 4 weeks on HFD not injected with the probe) are shown. (B) Fluorescence ratio of cryosections calculated of the ROI (aortic arch). Grey colored dot plot represents autofluorescence in atherosclerotic mice after 4 weeks of HFD, not injected with the NIRF agent ($p<0.05$). (C) Localization of activated NIRF imaging agent in the endothelial cell layer of the ascending aorta. In the top panel, a brightfield image of the atherosclerotic vessel is shown. In the bottom panel a high magnification of the plaque is shown. The activated imaging agent is represented in red, nuclei are counterstained with DAPI (blue). Previously published in Glinzer et al.[150].

To further investigate the exact location of the fluorescent signal of the elastase-targeting NIRF agent within the arterial wall, fluorescent microscopy was used. Increased signals in the near infrared light spectrum (680 nm) were localized to the endothelial cell layer of the ascending aorta and to regions of bifurcation along the aortic arch (Figure 14C). In addition, intense signal of the elastase-targeting NIRF agent was detected within plaque regions[150].

Fluorescence imaging of NIRF imaging agent in whole body cryosections of atherosclerotic mice confirmed that the in vivo measured signal is located in atherosclerotic plaques of the aortic arch. To elucidate if neutrophils, as source of

elastase, are responsible for the measured fluorescent signal in vivo and ex vivo histological analyses were subsequently examined.

3.2.4 Histological Analyses of Plaque Size and Neutrophil Count

To quantify the progression of atherosclerosis, plaque area was measured in histological sections of the aortic root and aortic arch. Plaque size increased over time in both regions (Figure 15A-B). To further localize neutrophils in atherosclerotic lesions, immunohistochemical staining of Ly6G was performed. $Ly6G^+$ neutrophils were located in both the atherosclerotic plaques in the aortic sinus as well as in lesions of the aortic arch (Figure 15C-D). The number of neutrophils per plaque area was increased at 4 and 8 weeks of HFD in the aortic root, and lower at 12 weeks of HFD. In the aortic arch, number of neutrophils peaked at 4 weeks of HFD, followed by a decline in the further course of the study. Frequencies of neutrophils were higher in the aortic arch region compared the aortic root (Figure 15A-B).

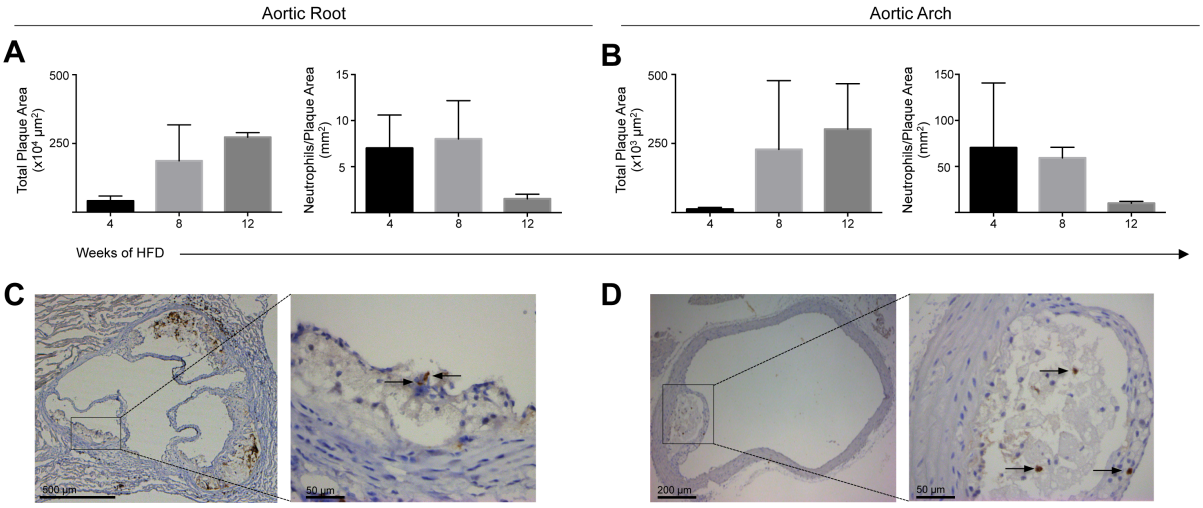

Figure 15 Detection of neutrophils in atherosclerotic plaques. (A-B) Quantification of total plaque area and number of neutrophils/plaque area in aortic root sections (A) and aortic arch sections (B). Graph shows mean ± SD (n=3 mice per group). (C-D) Representative immunostaining of Ly6G-positive neutrophils (indicated by arrows) in sections of the aortic root (C) and aortic arch (D). The cells are counterstained with haematoxylin, showing cell nuclei in blue. Previously published in Glinzer et al.[150].

Histological analysis proved the presence of advanced plaques in the course of atherosclerosis. Furthermore, neutrophils are located in atherosclerotic plaques in the aortic root and arch[150].

The first imaging approach was used to target the biological activity of a cell specific enzyme within atherosclerotic plaques. A NIRF imaging agent was applied, which is specific for elastase secreted by neutrophils and is detected in early atherosclerotic lesions.

The next imaging approach will illustrate how a magnetic resonance imaging agent can be used to target atherosclerotic plaques by addressing components of the extracellular matrix.

3.3 Combined Magnetic Resonance Imaging and Matrix-assisted Laser Desorption/Ionization Imaging Mass Spectrometry of Atherosclerotic Plaques

This approach aimed to assess if Gadofluorine P can be used as a plaque-targeting MR contrast agent to target components of the extracellular matrix, respectively plaque composition, and if MALDI-IMS is a suitable method to quantify gadolinium chelates within atherosclerotic plaques ex vivo. Relaxivity experiments were conducted first to determine the specific relaxivity of Gadofluorine P dependent on different field strengths. Afterwards in vivo experiments were established. Therefore, a kinetic study with atherosclerotic mice was performed to conclude the time point of peak enhancement. Subsequently, *LDLR*$^{-/-}$ mice fed a HFD for 4, 10, 15 and 20 weeks were injected with the contrast agent and imaged at the 7 T MRI scanner. After each imaging time point mice were euthanized for ex vivo analysis. MALDI-IMS was used to confirm accumulation of the contrast agent in atherosclerotic plaques.

3.3.1 Relaxivity of Gadofluorine P at Different Field Strengths

Contrast agents can be evaluated by their relaxivity r_1. The relaxivity represents how the relaxation rate (R_1) of a solution changes as a function of contrast agent concentration, temperature, pH, field strength and solvent. To obtain the relaxivity r_1 different concentration of Gadofluorine P in saline buffered aqueous solution and human serum were measured at field strengths of 1,3 and 7 T. Human serum was included as dissolving agent as Gadofluorine contrast agents show a strong albumin binding in the circulation. Gd-DTPA, which is commonly used in clinics, was used as a comparison to Gadofluorine P.

First of all, the relaxation rate R_1 was assessed for all field strengths of each concentration in both solutions, saline buffered aqueous solution (NaCl) and human serum. The R_1 values for both contrast agents are shown for all field strengths in Figure 16. The R_1 values at all field strength for Gd-DTPA increase with higher gadolinium concentration in aqueous solution and serum, but almost no impact of the field strength on the R_1 values are seen (Figure 16A).

The concentration-dependent manner is also observed for Gadofluorine P. Nevertheless, the field strength influences the relaxation rate. The relaxation rate for each gadolinium concentration is higher compared to Gd-DTPA, the highest relaxation rate is observed at 1 T (Figure 16).

The relaxivity r_1 is reflected by the slope of the relaxation rate at different concentrations. Plotting the relaxivities of Gd-DTPA demonstrate that no relevant differences in r_1 relaxivity at different field strengths are seen (4.2073 $mM^{-1}s^{-1}$ at 1 T, 4.0810 $mM^{-1}s^{-1}$ at 3 T, 3.8172 $mM^{-1}s^{-1}$ at 7 T) between aqueous solution and human serum (Figure 16).

Relaxivity values of Gadoflourine P showed a strong field strength dependency (17.0047 $mM^{-1}s^{-1}$ at 1T, 7.6484 $mM^{-1}s^{-1}$ at 3T, 6.0225$mM^{-1}s^{-1}$ at 7T in serum), but no differences were seen between aqueous solution and human serum (Figure 16).

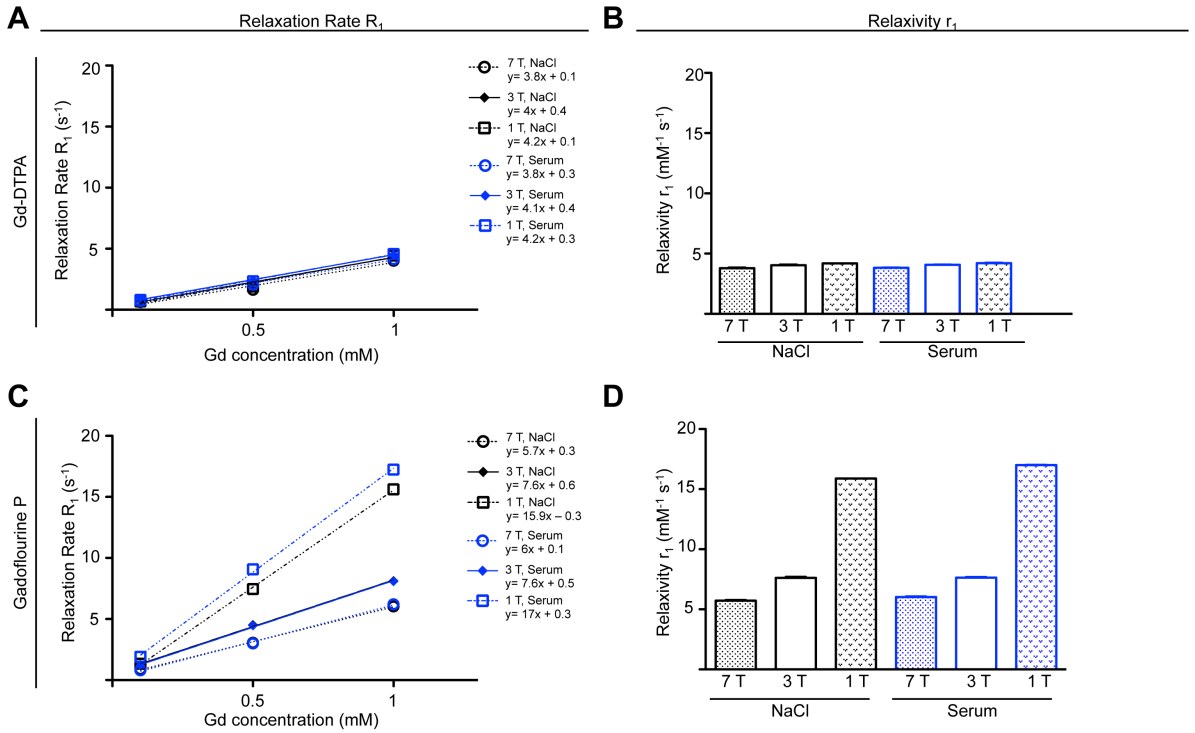

Figure 16 Determination of relaxivity in aqueous solution and human serum. (A, C) The relaxation rate R_1 at different gadolinium (Gd) concentrations was determined. The slope reflects the relaxivity r_1. Relaxivity values for Gd-DTPA and Gadofluorine P in different dissolving agents at different field strength are shown in (B) and (D).

The relaxivity is characteristic for each MR contrast agent. Gadofluorine P shows a higher field strength dependency compared to Gd-DTPA. To demonstrate if Gadofluorine P can be used as plaque-targeting contrast agent in vivo experiments are performed.

3.3.2 Kinetic Study of Gadofluorine P Accumulation in Atherosclerotic Plaques

A kinetic study of Gadofluorine P accumulating in atherosclerotic plaques was conducted to define the peak of enhancement as a function of time. *LDLR*$^{-/-}$ mice (n=3) were imaged after 20 weeks of HFD. An inversion recovery sequence was performed 1 min after intravenous injection of Gadofluorine P for anatomical depiction and to prove contrast agent circulation (Figure 17A). R_1 values were determined with T1 mapping techniques based on a Look Locker sequence for assessment of contrast enhancement. To localize aortic plaques on the T1 Map, the map was fused with the anatomical depiction.

The values of atherosclerotic plaques, located in aortic root and blood, were tracked over a timeframe of 6 h. Skeletal muscle was used as a reference of no contrast agent accumulation.

R_1 values in the blood reached a maximum after 15 to 30 min, and decreased to baseline values after 6 h. R_1 values of the plaque peaked 30 min after injection. The values returned to baseline after 6 h (Figure 17B), respectively. Due to albumin binding of Gadofluorine P highest R_1 values were acquired within the blood.

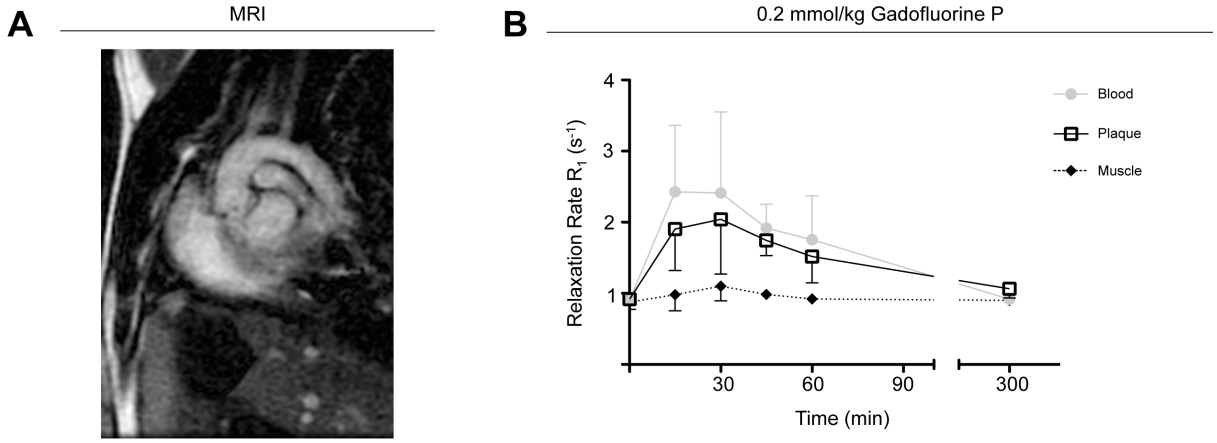

Figure 17 Kinetic study of contrast enhancement in atherosclerotic plaques. (A) Gadolinium enhancement represents contrast agent circulation after administration of Gadofluorine P (0.2 mmol/kg body weight) in the aortic arch. (B) In vivo MRI kinetic study of Gadofluorine P accumulation over a time period of 6h. R_1 values for atherosclerotic plaques, located in the aortic root, blood and skeletal muscle are presented (n=3; mean ± SD).

To proof accumulation of Gadofluorine P in plaques, MALDI-IMS was performed after MR imaging. All mice of the kinetic study developed severe atherosclerotic lesions shown as in EvG-stained sections (Figure 18 upper panel). Gadofluorine P accumulation was successfully detected by MALDI-IMS (Figure 18 middle Panel) and was mapped to corresponding EvG sections (Figure 18 lower panel). To quantify Gadofluorine P accumulation the ratio of plaque accumulation compared to healthy myocardium was calculated. The results are shown in Figure 18B. The accumulation of Gadofluorine P over a time period of 60 min is similar to the in vivo contrast enhancement. However, the highest Gadofluorine P accumulation was observed after 45 min due to prolongated dissection processes.

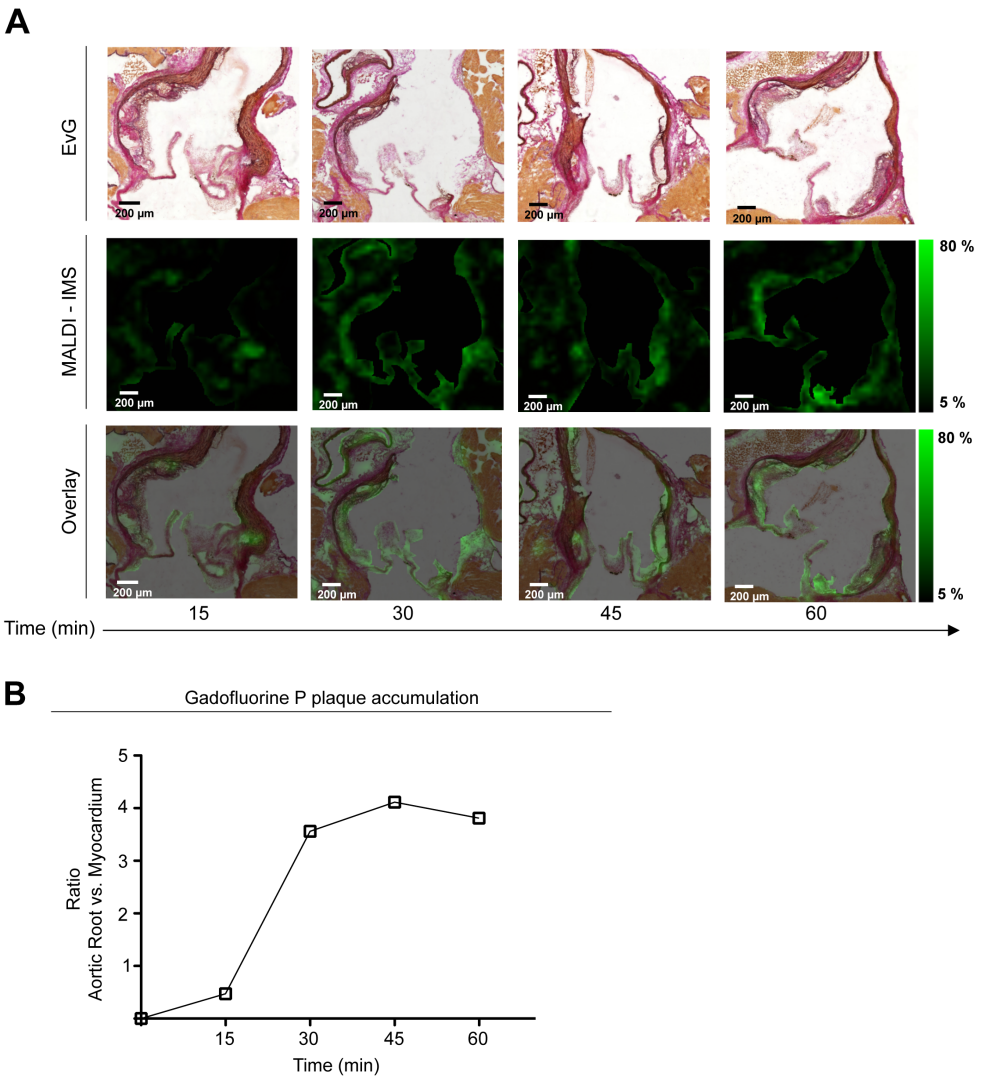

Figure 18 Kinetics of Gadofluorine P in atherosclerotic plaques. (A) EvG stains (upper panel), MALDI-IMS detection (middle panel) and fusion of EvG and MALDI-IMS (lower panel) are shown for each time point of the kinetic study. (B) A ratio was calculated for each time point to quantify Gadofluorine P accumulation with MALDI-IMS.

The kinetic study showed that Gadofluorine P accumulates in atherosclerotic plaques with peak enhancement after 30 min. Further experiments testing the contrast agent during the course of atherosclerosis are performed. The imaging time point after Gadofluorine P injection is set at 30 min.

3.3.3 Accumulation of Gadofluorine P during the Course of Atherosclerosis

To analyze the accumulation of the contrast agent during the course of atherosclerosis, imaging was performed after 4, 10, 15 and 20 weeks of HFD.

The ROIs were placed in plaques, located in the aortic root, which are highlighted in the image of Figure 19A. R_1 values in plaques of the aortic roots increased from 4 weeks to 10 weeks to 15 weeks of HFD (4 vs. 15 weeks of HFD p=0.0392). After 20 weeks of HFD no differences were seen compared to 15 weeks of HFD (Figure 19A).

To verify Gadofluorine P accumulation in the atherosclerotic plaques MALDI-IMS was performed. The accumulation over the course of atherosclerosis was successfully detected with MALDI-IMS. To quantify Gadofluorine P accumulation a ratio of Gadofluorine P accumulation compared to healthy myocardium was calculated. The increase of Gadofluorine P-enhanced MR signal was corroborated by increased quantification of Gadofluorine P with MALDI-IMS from 4 to 15 weeks of HFD. The slight decrease after 20 weeks of HFD was also detectable with MALDI-IMS (Figure 19B).

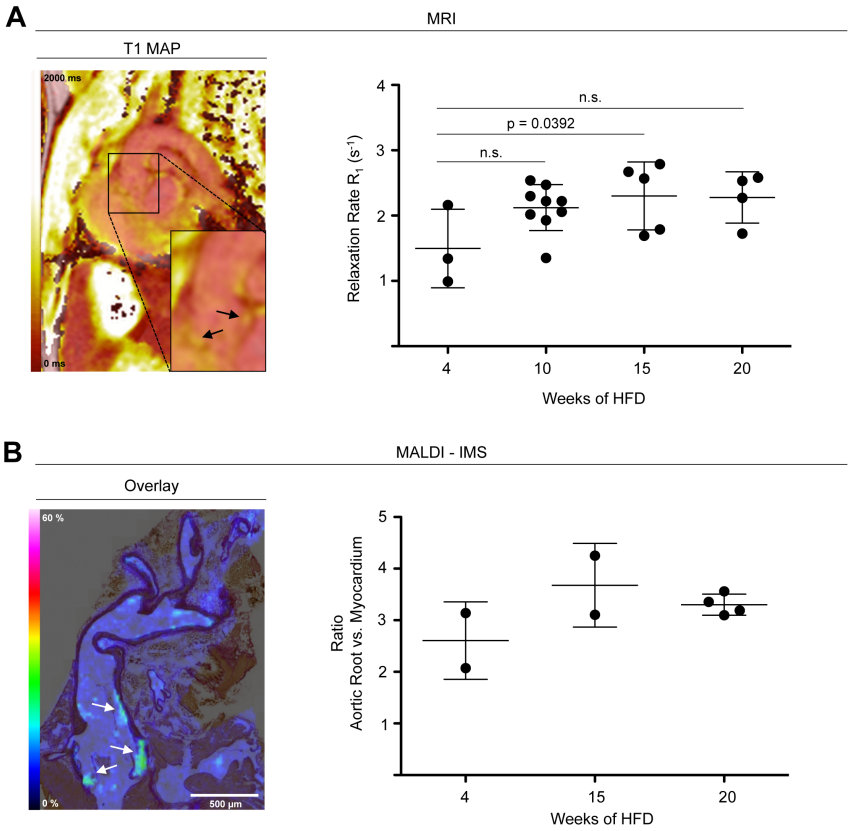

Figure 19 Accumulation of Gadofluorine P during the course of atherosclerosis. (A) Left panel shows T1 Map with highlighted Gadofluorine P contrast enhancement in plaques located in the aortic root. Right panel represents the change of relaxation rate R_1 after 4,10,15 and 20 weeks of HFD. (B) Contrast agent accumulation with MALDI-IMS was located in atherosclerotic plaques (left panel) and was quantified over the time of HFD (right panel).

Gadofluorine P contrast enhancement increased with more advanced inflammation and plaque development. This was in addition confirmed with MALDI-IMS. To elucidate if the plaque composition is responsible for Gadofluorine P accumulation further experiments are necessary.

The second imaging approach showed how MRI could be used to target atherosclerotic plaques. The contrast agent accumulation was confirmed with MALDI-IMS.

This imaging approach as well as the previous approach focused on the application of imaging modalities to address biological activity within plaques and to detect plaque localization. In the third approach imaging modalities are used to develop and support a workflow to create a 3D reconstruction of the murine aortic arch based on serial histological sections. This 3D representation can be used to visualize atherosclerosis for a better understanding of functional and spatial relationships.

3.4 Application of Imaging Modalities to Create a Three-Dimensional Histological Reconstruction of the Murine Aortic Arch

In the third approach imaging modalities are used to achieve the following aim: Creating a 3D reconstruction of the murine aortic arch based on serial histological sections.

Within this collaborative project image processing and reconstruction algorithms (data not published) were developed by our collaboration partner Moritz Thon (High Performance Computing Group – Prof. Dr.-Ing. Michael Gee, Technische Universität München) and are not part of this work.

3.4.1 Preparation of Serial Histological Sections and Digitizing

The 3D reconstruction is based on serial histological sections of the murine aortic arch. Therefore, serial histological sections of the murine aortic arch were be accomplished and digitized. The aortic arches of healthy *LDLR*$^{-/-}$ mice were fixed and harvested as described in chapter 2.4.4.1 followed by embedding in paraffin. The direction of embedding is illustrated in Figure 20A. With this embedding direction vessel cross sections were achieved in the part of the arch, not in the ascending and descending part. The ascending and descending part of the aortic arch are cut diagonally. Serial sections of the whole aortic arch were produced with a slice thickness of 5 µm.

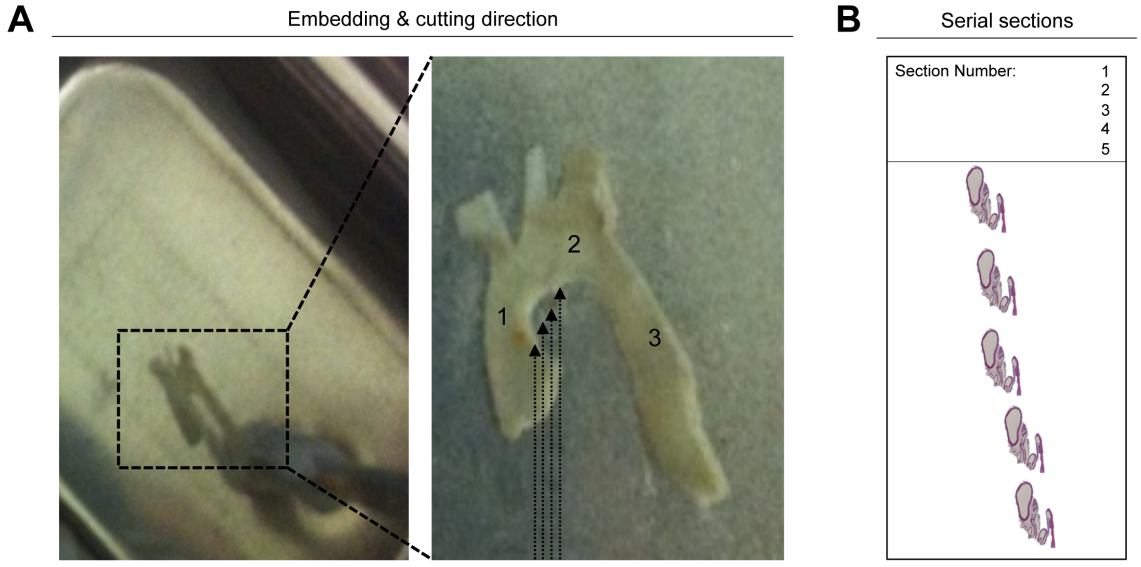

Figure 20 Overview about embedding direction and resulting sections. (A) The murine aortic arch was embedded in paraffin as shown on the picture. Narrows indicate the cutting direction. The ascending (1) and descending (3) part of the aortic arch were cut diagonally; cross sections were made in the area of the arch (2). (B) Exemplary illustration of serial sections of the vessel placed on glass slide approximately with the same orientation.

During the slicing process each slice was labeled with a consecutive number. If a slice was missing due to cutting problems it was documented in the cutting protocol. The sections were mounted on glass slides, 5 sections per slide, with approximately the same orientation of each section (Figure 20B). After cutting procedures an H&E stain was performed (Chapter 2.4.5.1). Each section was viewed and digitized with a 1.5x magnification and the image was saved in accordance with the cutting protocol. This histological imaging data set was transferred to the High Performance Computing Group for further processing to create a 3D reconstruction.

3.4.2 Rigid and Soft Registration of Histological Data Set

Image registration methods are applied to fulfill a reconstruction of the histological imaging data set. Therefore, all digitized images were post-processed by Moritz Thon using MATLAB© (The MathWorks, Natik, Massachusetts, USA). The results are shown to demonstrate the image registration work and thus reevaluation of the experimental workflow.

Images were pre-selected for image registration: Images of sections, which were folded during the movement from the microtome to the glass slide or sections, which partly detached during the staining process, were excluded.

Furthermore, for each histological image of the aortic arch the surrounding tissue (e.g. fatty tissue) had to be removed. This step was achieved by thresholding the gray-scale and creating a binary picture to exclude stained tissue, which does not belong to the vessel (Figure 21A).

After a section was made at the microtome, the 5 µm paraffin slice is transferred to the glass slide. Due to handling issues each slice cannot be orientated exactly in the same direction and position to the other ones. On account of this each image was disorientated. This problem is solved as follows: For two consecutive images the best translation and rotation is found that the pixel-wise image to image difference is minimal. The images were overlaid. This part is referred to as rigid registration (Figure 21B).

The distance between each section, hence between each image, was 5 µm, the slice thickness. To bridge the gap intermediate images must be generated. Each pair of images were interpolated to find the best deformation that one image matches the other. If slices are missing more interpolated images must be produced. The cutting

protocol elucidated missing images. This part is referred to as soft registration (Figure 21C).

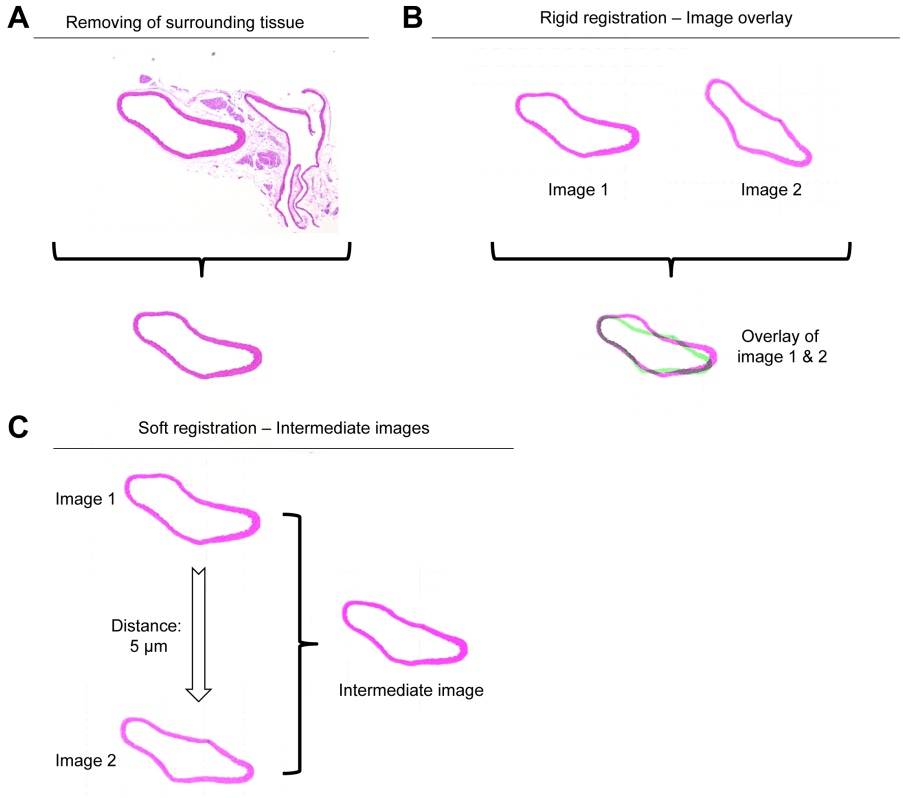

Figure 21 Image registration process. (A) Surrounding tissue, which does not belong to the vessel, was removed. (B) Rigid registration is able to overlay consecutive images. (C) Soft registration enables intermediate images.

With rigid and soft registration steps a 3D reconstruction can be made. An exemplary reconstruction of a selection of images is shown in Figure 22.

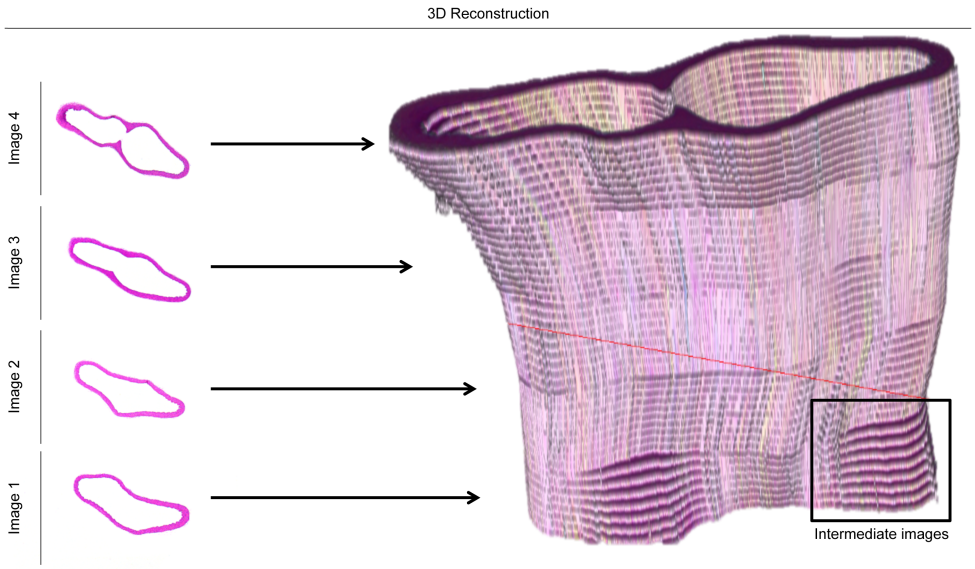

Figure 22 Reconstruction of histological sections using rigid and soft registration.

The 3D reconstruction represented a stack of images (Figure 22). The crucial step in this workflow was the missing information about the curvature of the aortic arch, which is illustrated in Figure 23.

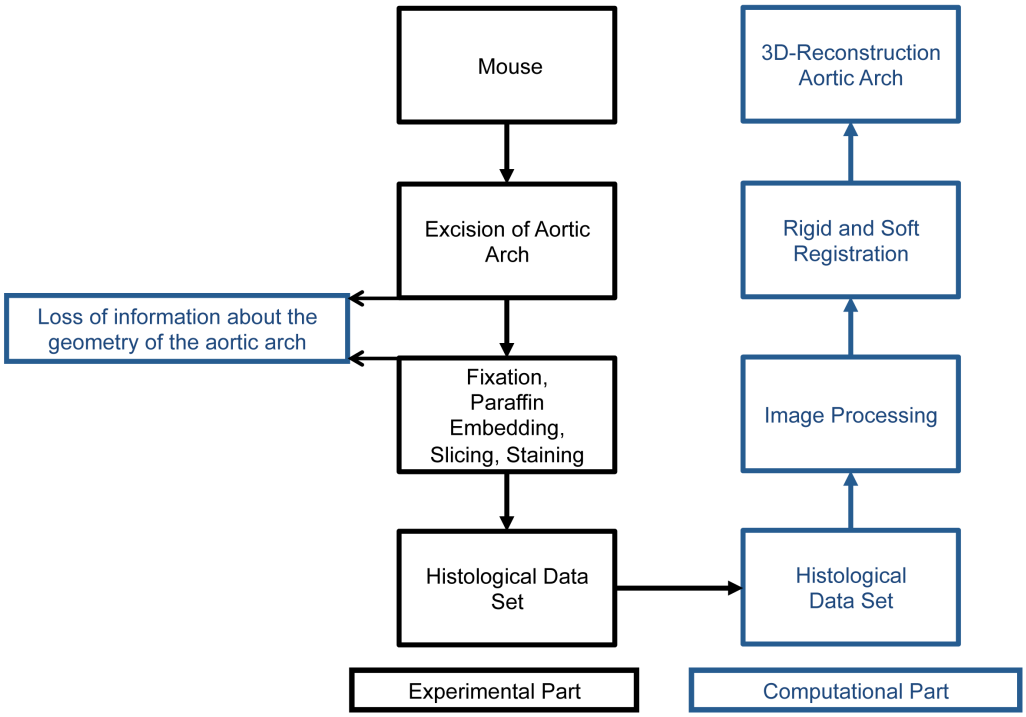

Figure 23 Workflow for creating a 3D reconstruction with serial histological sections. The workflow is separated in an experimental and computational part. After excising the aortic arch and serial sectioning information are lost about the geometry of the aortic arch. After H&E stain the image data set is processed with rigid and soft registration steps to generate a 3D reconstruction.

To gain information how this stack of images must be bended the workflow was adopted and optimized, which is described within the next chapter.

3.4.3 Protocol Optimization

The crucial part to accomplish a 3D reconstruction is the information about the shape and geometry of the aortic arch. Different approaches to optimize the protocol are described in this chapter.

3.4.3.1 Internal Reference Point

Including an internal reference point offers the possibility to adjust the stack of images to a fixed reference point. The internal reference point is always at the same position in the paraffin block and on the slide. The position of the aortic arch is changing due to the bending. With this idea a realistic geometry of the reconstructed aortic arch could be generated.

Therefore, a rectangular tissue piece of murine liver was included in the paraffin block (Figure 24A). After serial sectioning and staining the images were digitized (Figure 24B). On each image the vessel as well as the liver is seen. The histological image data set was processed with rigid registration and was adjusted to the position of the liver piece.

A 3D reconstruction is shown in Figure 24C. The stack of liver images is perfectly reconstructed, proving exactly the same position of the liver piece in the paraffin block. However, the adjustment of the aortic arch section to the internal reference point, piece of liver, did not succeed.

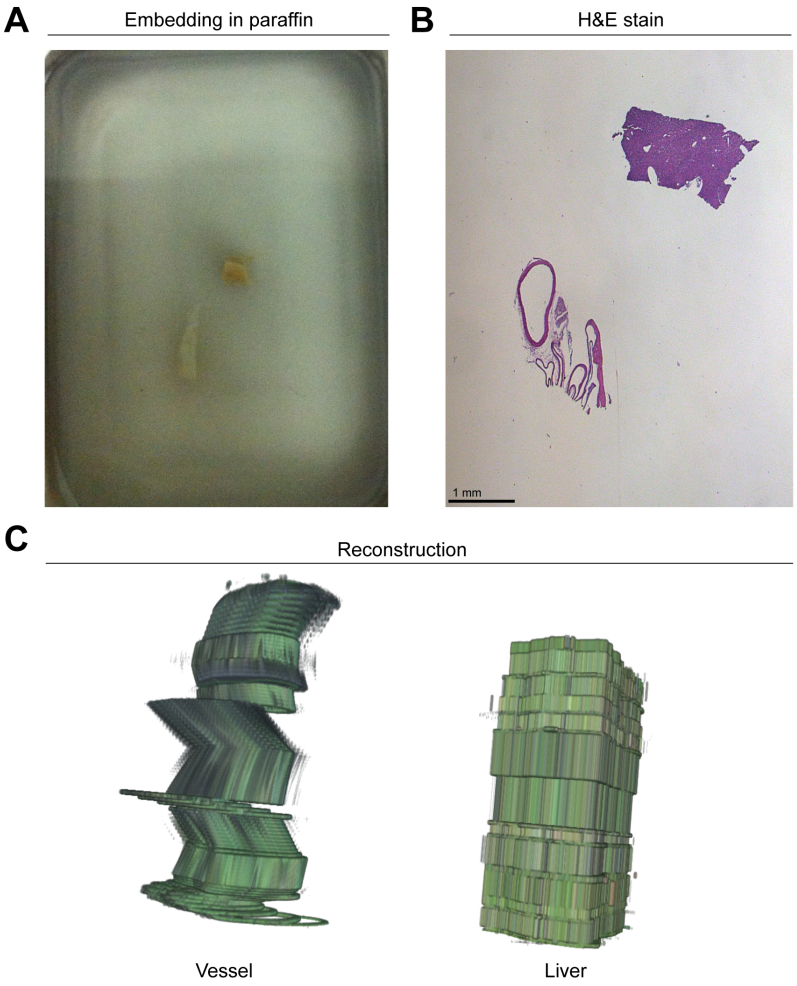

Figure 24 Internal reference point. (A) A piece of murine liver is included during embedding in paraffin. (B) Image of a histological section showing the vessel and the piece of liver. (C) Result after rigid registration followed by adjusting to the internal reference point.

3.4.3.2 Contrast Enhanced Imaging of the Murine Aortic Arch

The next approach to gain information about the curvature is based on the real anatomical shape of the aortic arch in vivo. Therefore, MR imaging is used to conduct contrast enhanced imaging of the murine aortic arch in order to perform centerline calculation. This centerline could serve as a reference for the curvature of the aortic arch.

Contrast enhanced MR imaging was performed in the area of the heart and the aortic arch (Figure 25A). MR images were acquired in axial slices as shown in Figure 25B. Afterwards, the MR data set was prepared for centerline calculation. The aortic arch was excised and processed as described above to generate a histological imaging data set. Pixel segmentation was performed on all MR images, which reflect the aortic arch. Pixels belonging to the aortic vessel lumen were segmented. Pixel segmentation and centerline calculation was conducted by Moritz Thon using Mimics® software (Materialise, Leuven, Belgium).

After pixel segmentation the software creates a 3D reconstruction based on the vessel lumen and the coordinate system of the MRI data set (Figure 25C). Based on this a centerline was calculated. The centerline shows several focal points of the vessel. An exemplary centerline is shown representing the aortic arch and the bifurcations (Figure 25D).

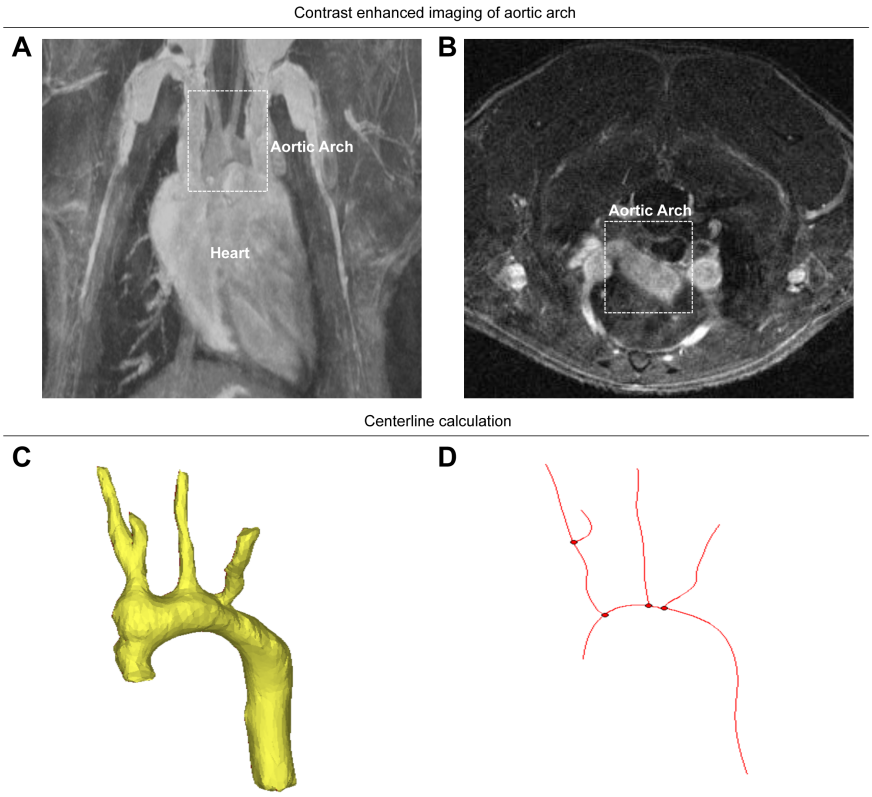

Figure 25 Contrast enhanced imaging and centerline calculation of murine aortic arch. (A) MRI image after contrast agent injection showing the heart and the aortic arch. (B) Axial view of the aortic arch. Pixels belonging to the vessel lumen are used for segmentation. (C) Reconstruction of aortic arch and bifurcations after pixel segmentation. (D) Corresponding centerline.

After centerline calculation the histological data set was registered to its centerline. Contrast enhanced imaging as well as centerline calculation, followed by preparation of histological imaging data set was applied for two murine aortic arches. Table 5 gives an overview about the number of histological images, how many images were excluded for registration and how many images including intermediate images were used in total for 3D reconstruction of two murine aortic arches.

Table 5 Number of images for 3D reconstruction. The resulting number of histological images after slicing and staining for each mouse are shown in the left column. In the middle column the reduced number of images is shown. Images were excluded due to secondary deformations. The gap between each image including missing images was filled with intermediate images resulting in high amount of images.

	Histological images	Reduced number of histological images	Total number of images
Mouse 1	402	355	1866
Mouse 2	493	455	2636

To achieve the curvature similar to the original in vivo curvature, the reconstructed stack of histological images was adjusted to each calculated centerline.

The results are shown in Figure 26. For both mice (Figure 26A-B) the 3D reconstruction succeeded in the area of the aortic arch. The representing areas of the ascending and descending part do not reflect cross sections due to the embedding direction in paraffin (Figure 26). The aortic arch consists of three bifurcations: the brachiocephalic trunk separating in right common carotid and right subclavian artery, the left common carotid artery and the left subclavian artery. The reconstruction of the bifurcations was challenging. The reconstruction of Mouse 1 indicates three bifurcations (Figure 26A); Mouse 2 only indicates two bifurcations (Figure 26B).

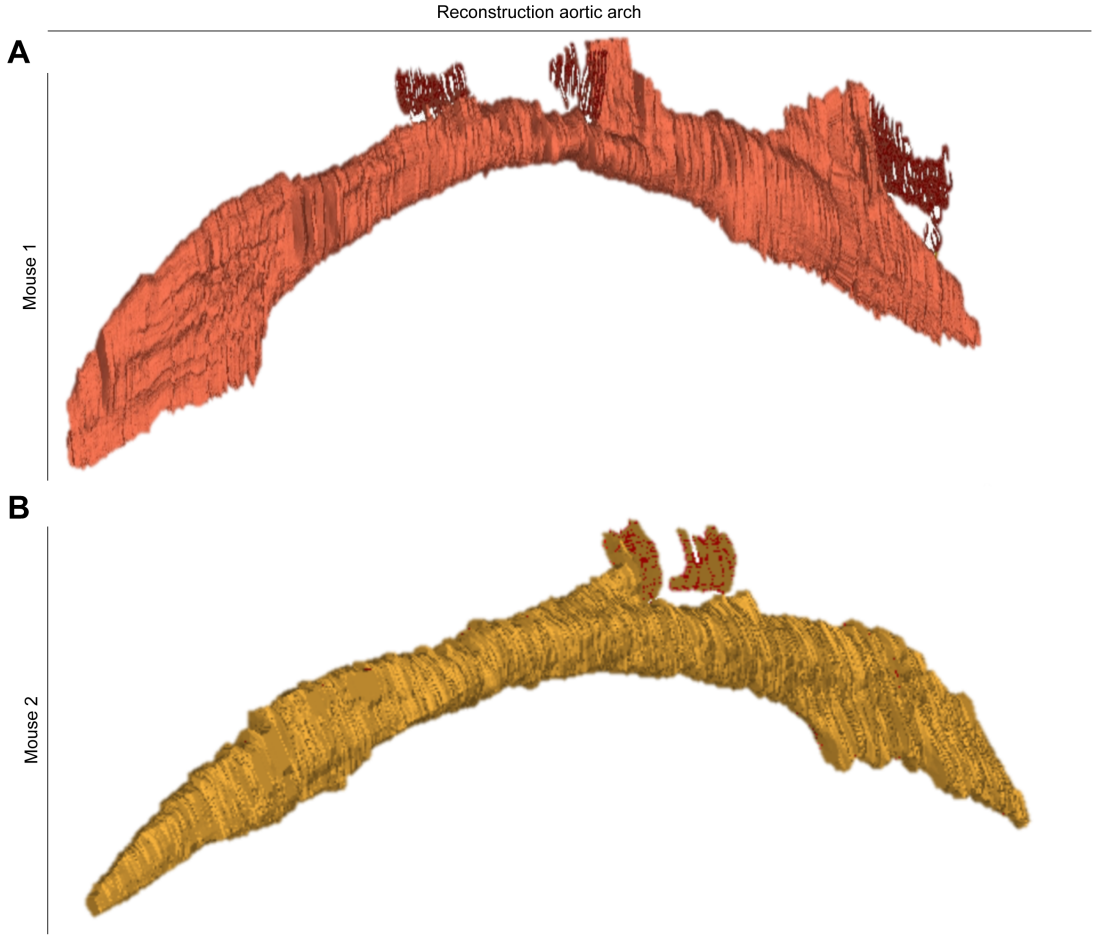

Figure 26 3D reconstructions of murine aortic arches. (A) Reconstruction aortic arch Mouse 1. (B) Reconstruction aortic arch Mouse 2.

The approach of including contrast enhanced imaging and centerline calculation improved the 3D reconstruction. Nevertheless, deformations and shrinkage occur during tissue preparation, which are not considered in the reconstruction. Therefore, a further imaging modality is introduced to correct this.

3.4.3.3 Micro-computed Tomography of Murine Aortic Arch Embedded in Paraffin

Especially during fixation and dissecting of the aortic arch deformations and shrinkages of the aortic arch take place. Imaging of the aortic arch embedded in paraffin with micro-computed tomography provides detailed information about the occurred deformations for precise 3D reconstruction of the aortic arch based on serial histological sections. µCT offers the feasibility to image internal structures in a spatial resolution of micrometers. Information about the precise arrangement in paraffin and the curvature of the aortic arch ex vivo would support an accurate reconstruction of the aortic arch.

After excision, fixation, and dehydration the aortic arch is embedded in paraffin. Before sectioning was performed, a µCT scan of the paraffin block was implemented. Therefore, the paraffin block is minimized in size to reduce the measurement time (Figure 27A). An overview scan was performed to localize the aortic arch in paraffin (Figure 27B). Afterwards, a high resolution scan was applied with a resolution of 2.3567 µm/pixel and was further processed for image analysis (Figure 27C). The vessel wall can clearly be distinguished from paraffin. Furthermore, deformations of the tissue are seen.

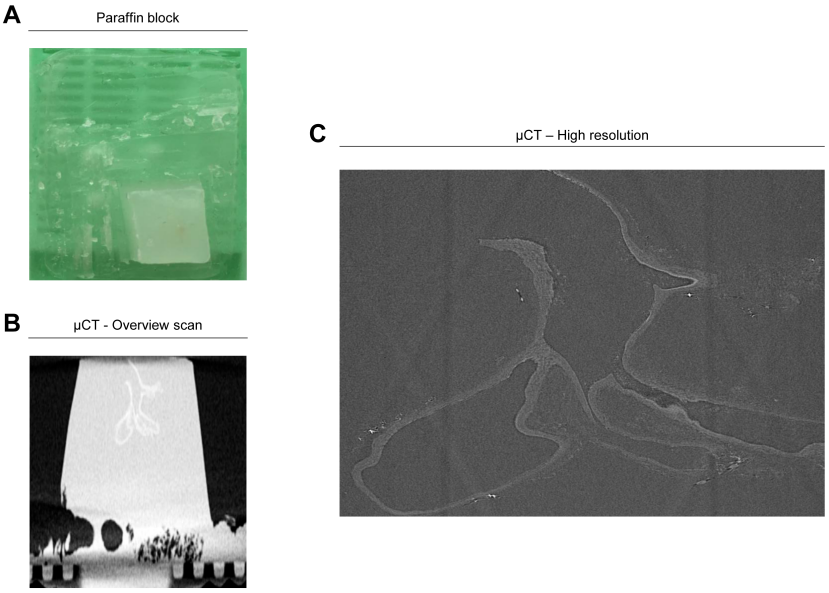

Figure 27 µCT of aortic arch in paraffin. (A) Excessive paraffin was removed to reduce scan time. (B) Overview scan of aorta in paraffin. (C) High resolution scan of aortic arch in paraffin.

The µCT data could be further processed for centerline segmentation representing ex vivo conditions. Thus, in vivo and ex vivo centerlines could be compared and applied for 3D reconstruction of the histological data set of the same mouse to minimize errors due to deformations and shrinkage.

A possible workflow how imaging modalities could be applied to create a realistic 3D reconstruction of the murine aortic arch is shown in Figure 28.

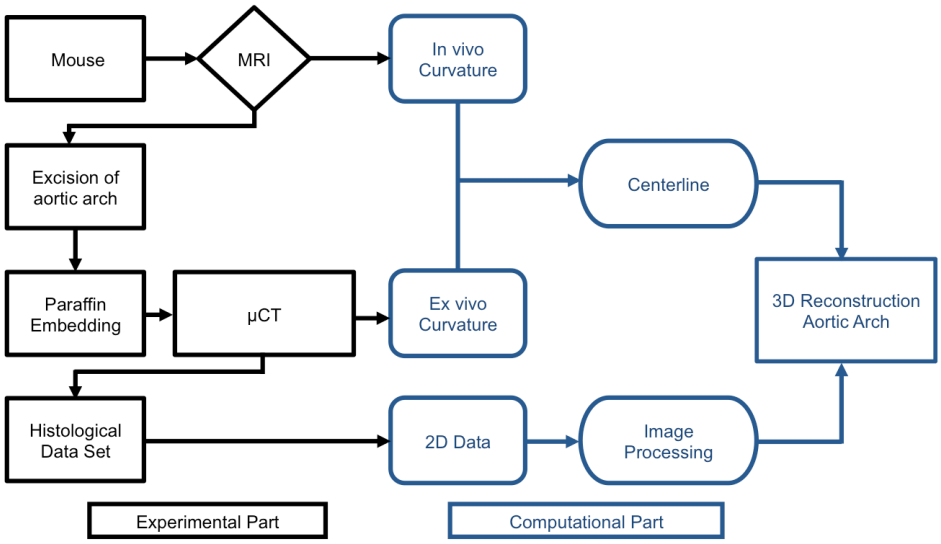

Figure 28 Optimized workflow for 3D reconstruction. The workflow represents the consideration of changes and deformations of the aortic arch from in vivo to ex vivo conditions. Imaging applications of MRI and µCT support the 3D reconstruction.

The workflow incorporates information about the original geometry of the aortic arch in vivo as well as considering shrinkage and deformation by displaying the ex vivo information.

The presented results show how imaging modalities are used to address different scientific questions. In the first approach FMT-XCT was applied for early detection of atherosclerotic lesions by targeting elastase activity. The second approach focused on MRI-targeted plaque imaging and ex vivo quantification of MR imaging agents. Within the third approach imaging modalities such as MRI and µCT were implemented into the workflow to create a realistic 3D reconstruction of the murine aortic arch.

4 DISCUSSION

4.1 Imaging of Elastase Activity in Murine Atherosclerotic Plaques

Imaging technologies can be applied to target biological activity in living animals. We therefore hypothesize with our first imaging approach that elastase-targeted imaging could be used for in vivo detection of neutrophil activity in the course of early atherosclerosis. Our results demonstrate that the evaluated NIRF imaging is specifically cleaved and activated by neutrophil content after lysis or cell stimulation. The in vivo fluorescent signal in the area of the aortic arch was highest after 4 weeks of high-fat diet feeding, indicating early atherosclerosis, and decreased at 8 and 12 weeks. Ex vivo whole-body cryoslicing confirmed the fluorescent signal to locate to the aortic arch and to originate from the atherosclerotic arterial wall. Histological analysis demonstrated the presence of neutrophils in atherosclerotic lesions.

Warnatsch et al. recently identified a complex interplay between macrophages and neutrophils based on the formation of NETs containing neutrophil elastase and myeloperoxidase in the early phase of plaque development in mice[72]. Thus, macrophages are primed for cytokine production and release supporting the inflammatory process[72]. Consequently, elastase is a promising target in atherosclerotic research to detect early stages of atherosclerosis, which was addressed in our approach. Non-invasive imaging modalities offer the opportunity for early detection and characterization of diseases. The outcome of atherosclerosis, myocardial infarction and stroke, are the leading causes of death in the western world indicating the need of such techniques to improve early detection of atherosclerotic plaques in order to prevent disease progression. Molecular imaging with FMT-XCT of atherosclerosis focused up to now mostly on tracking monocytes/macrophages and their corresponding proteases, such as cathepsins and MMPs.[91]. Nevertheless, no in vivo study of early stages of atherosclerosis was performed until now to detect neutrophil and elastase activity, respectively.

It has been shown by Kossodo et al. that the elastase-targeted NIRF imaging agent used in our approach is preferentially cleaved and rapidly activated by neutrophil elastase (both mice and human elastase) and is resistant to other serine proteases[140]. We have confirmed that the NIRF imaging agent showed a dose-

dependent activation by proteases secreted after isolation and stimulation of both murine and human neutrophils. To confirm specificity, that the amino acid sequence is preferentially cleaved by elastase, inhibition experiments were conducted. Sivelestat is a selective inhibitor of human elastase and is clinically used in acute lung injury[151]. Sivelestat belongs to the group of suicide inhibitors, which interact in a covalent manner with the enzyme's active site[152]. Our data proved the specificity of the probe for neutrophil elastase. Sivelestat inhibited human neutrophil elastase with an IC_{50} value comparable to previously published data[149]. Mouse elastase inhibition was more powerful compared to human elastase. In contrast to Kossodo et al. we additionally stimulated neutrophils after isolation to mimic the physiological process. Activation with two different stimulation agents, fMLP and PMA/Ionomycin, revealed similar effects of activity compared to lysis. Nevertheless, both stimulation agents pinpointed the efficiency of activation. PMA is a small organic compound, which diffuses into the cytoplasm and directly activates protein kinase C. Ionomycin, a calcium ionophor, triggers calcium influx, which is necessary for protein kinase C activation. The response of neutrophils to the chemoattractant fMLP is based on interaction with seven-transmembrane-spanning, G-Protein linked receptors resulting in activation of microtubule-associated protein kinase[153]. The higher extent of activation for PMA/Ionomycin is explicable because of direct activation of PMA combined with Ionomycin. Additionally, we noticed increasing fluorescent values for all human measurements. This can be explained by more efficiently cleavage of human elastase compared to mouse elastase. Work by Wiesner et al. supports our observation by highlighting differences of human and mouse elastase depending on the substrate[154].
In summary, the evaluation proved successfully the specificity of the probe in order to accomplish further experiments in vivo in a murine model of atherosclerosis.

The NIRF imaging agent was recently studied in a mouse model of acute lung injury[140], in a tumor mouse model[155], and in chlamydia-associated inflammation[156].
In our study, we measured the fluorescent signal in vivo by hybrid FMT-XCT, which enabled the anatomic localization of the targeted fluorescence to regions of the aortic root and arch of atherosclerotic mice. The signal increased between 0 to 4 weeks of HFD before it declined again after 8 and 12 weeks of HFD. Due to scattering in the biological tissue the imaging probe appeared large and diffuse, which exacerbated

the reconstruction of high-resolution images with FMT-XCT. These difficulties were already described in previously published reports[90, 157-159].

Ex vivo experiments of whole-body cryoslicing corroborated the in vivo results and confirmed increased fluorescence signals originating from the aortic wall, and quantification of cryoslicing results similarly showed an increased fluorescence signal at 4 and 8 weeks, thus, at early stages of lesion development. Fluorescence ratios were calculated to evaluate the fluorescence signal in cryosections in-between mice. Due to distinct integration times of the camera, due to slight changes of the laser light direction relative to the region of interest, and its distance to the camera there were differences in the dynamic range of fluorescence in each mouse, even after reducing background effects, so that the fluorescence ratio was calculated for quantitative comparison. Higher variability of the fluorescence ratio at 8 and 12 weeks was caused by difficulties of manual segmentation in the region of interest (close to the aorta) due to its small size and relative low signal intensity, while the same is not a problem with FMT-XCT data. FMT-XCT data offers a more accurate localization of the aorta due to better anatomical information of the XCT. Manual segmentation of the region of interest is also less difficult at 4 weeks of HFD, as the signal intensity in these mice is higher, associated with a much higher fluorescence ratio, hence enabling a more accurate segmentation with lesser variability. However, it has to be conceded that spatial resolution of FMT remains limited. Scattering of emitted fluorescence from deep tissue results in a diffuse FMT signal, which may appear to exceed the region of interest in the aortic arch, similar to previous findings[90, 157-159]. In addition, the fluorescence signal observed in FMT-XCT imaging contains fluorescence emitted from the target, but also background autofluorescence as well as fluorescence that may have been scattered from signals outside the blood vessel or adjacent mediastinal structures. Signals in the region of the aortic arch may thus not only originate from fluorescence emitted from plaque tissue but also from extravascular activation or trapping of the cleaved product. Those signals cannot be separated by FMT inversion. This may also be reflected by our FMT-XCT quantification results: at week 0, there is still a positive quantification value rather than zero, which may indicate the extent of autofluorescence and extravascular probe activation. However, signal intensities are much stronger in atherosclerotic mice at week 4, week 8 and week 12. This increase in fluorescence strongly

indicates that despite the limitations in spatial resolution, elastase-targeted FMT-XCT imaging can be used for in vivo detection of early atherosclerosis.
Fluorescence microscopy additionally verified the presence of emitted fluorescence from the elastase targeting NIRF agent in the atherosclerotic aorta and regions of plaque formation. A major contribution of plaque autofluorescence was ruled out by investigating atherosclerotic mice not injected with the NIRF probe, which did not show any fluorescence. These results thus demonstrate that the measured elastase activity is primarily associated with early stage atherosclerotic lesions.

Neutrophils are the source of elastase and therefore histological analyses were conducted. The plaque area over time increased as expected. The number of neutrophils per plaque area increased after 4 and 8 weeks of HFD and decreased thereafter. This is in accordance with previously described kinetics[46, 56]. It should be noted that the neutrophil counts within plaque tissue are low (~ 5-50 neutrophils per square millimeter of plaque).
The relative number of neutrophils was in accordance with the results of in vivo FMT-XCT measurements and ex vivo cryosection analyses. Nevertheless, a correlation between the relative number of cells and the FMT-XCT values did not reveal a significant correlation. Two near infrared imaging agents, cathepsin and $\alpha_V\beta_3$ integrin specific, were tested in atherosclerotic mice in a published study. The macrophage count correlated with the FMT signal, but a minimum number of 100 macrophages was observed[96].
This indicates that either the signal could be just generated by accumulating of the probe in the plaque or in addition other inflammatory cells must be responsible for the elastase fluorescent signal.
The life span of neutrophils is very short pointing out that the low number in histological sections must not reflect the original number of recruited neutrophils. As already described neutrophils form neutrophil extracellular traps, which contain neutrophil elastase in the extracellular space and are found in atherosclerotic plaques[72]. Furthermore neutrophil elastase is released and deposited within the arterial wall[67, 160] and may persist even after neutrophil cell death.
Another explanation for the detected fluorescent signal could be that neutrophil elastase may also be derived from alternative sources. Dollery et. al. showed that activated vascular endothelial cells, monocytes, and macrophages contain neutrophil

elastase mRNA and can produce neutrophil elastase[161]. Thus, endothelial cells and early infiltrating mononuclear phagocytes may in addition contribute to lesional neutrophil elastase activity.
In addition, it could also be possible that other enzymes contribute to the fluorescent signal by unspecific cleavage of the amino acid sequence of the NIRF agent. Potential protease substrate cleavage sites can be predicted using a published online tool[162]. This indicated potential substrate cleavage also by MMP 9 and Cathepsin G for the amino acid sequence of the assessed probe.
Further experiments are necessary to determine the origin of the measured fluorescence signal in vivo and ex vivo. Neutrophil elastase itself could be histologically localized and quantified. Afterwards a new correlation to in vivo data could reveal more information. In addition it should be reassessed if the NIRF imaging agent could be cleaved by MMP 9 and Cathepsin G in vivo.

The following aspects has not been taken into account: Besides scattering in the biological tissue we are not aware if the fluorescence derives maybe from lung tissue or any other surrounding tissue containing elastase. Adventitial derived neutrophils were seen in our analyzed histological sections. Infection of the mice could additionally falsify our results because neutrophils are recruited for first line defense in the event of infection.

Early stage atherosclerosis may still be reversible to a certain degree. Sivelastat, a synthetic neutrophil elastase inhibitor, effectively reduced inflammation in acute lung injury in animal models and clinical trials[151, 163]. However, Sivelestat has not been investigated in the context of atherosclerosis. Taking recent work by Warnatsch et al.[72] and our results into account, the presence of neutrophil elastase in early atherosclerotic lesions, may suggest its suitability for pharmacological intervention. In addition, established or new pharmacological interventions suppressing the early progression of atherosclerosis could potentially be monitored in vivo by detecting elastase activity.
Although fluorescence molecular imaging has long been restricted to preclinical setups, its clinical translation is within reach. Miniaturization of fluorescence detectors have enabled mounting the entire instrumentation of angiography catheters, already evaluated successfully in large animal models of atherosclerosis[164, 165]. Detection of

early atherosclerotic lesions in patients before calcifications occur is limited using current technologies of biomedical imaging. Detection of neutrophil elastase using catheter-based fluorescence imaging would enable to capture early lesion formation also in patients, thereby enabling tailored treatment approaches. Similarly, as elastase plays an import role during plaque rupture, catheter-guided detection of vulnerable atherosclerotic lesions might become feasible in the clinical setting.

In summary, the present imaging approach provides new insights into elastase-targeted imaging of early stages of atherosclerosis. The findings show that the assessed probe can be used as a fluorescent biomarker of elastase activity in atherosclerotic mouse models and that this imaging approach could be explored for application in clinical settings. Nevertheless, more experiments must be conducted to verify where elastase is specifically located and if other proteases may have contributed to the fluorescent signal[150].

This imaging approach was used to target biological activity in atherosclerotic plaques. The second imaging approach deals with the application of MR imaging to target more advanced atherosclerotic lesions in vivo, which will be discussed in the following chapter.

4.2 Combined Magnetic Resonance Imaging and Matrix-assisted Laser Desorption/Ionization Imaging Mass Spectrometry of Atherosclerotic Plaques

Besides FMT-XCT also MR imaging is an emerging tool to gain more insights about biological processes of atherosclerosis with high spatial resolution. The second imaging approach is based on the application of a plaque-targeting MR contrast agent.

We hypothesize that Gadofluorine P can be used as a plaque-targeting MR contrast agent to address extracellular matrix components, respectively plaque composition, during atheroprogression. Furthermore, we postulate that MALDI-IMS is a suitable method to quantify gadolinium chelates in atherosclerotic plaques ex vivo after in vivo imaging. Our results demonstrate that Gadofluorine P can be used to detect atherosclerotic plaques in vivo. Gadofluorine P accumulates with favorable kinetics in atherosclerotic plaques. A signal increase is seen during the progression of atherosclerosis presumably to changes in extracellular matrix composition. Accumulation of Gadofluorine P in atherosclerotic plaques located in the aortic root is confirmed with MALDI-IMS. Quantification of Gadofluorine P accumulation with MALDI-IMS corroborated the in vivo measured results.

MR imaging is dependent on specific contrast agents to enhance signal intensity. A number of gadolinium-based contrast agents have been developed and applied for preclinical and clinical imaging of atherosclerosis. Gadofluorine M was successfully used to visualize advanced atherosclerotic plaques in mice and rabbit as a result of extracellular matrix remodeling[117, 141, 166]. Due to disadvantages of prolonged blood and tissue half-life and thus delayed excretion, the precursor Gadofluorine M was further developed and chemically modified. This included replacing of the lysine backbone with a short ethylendiamin-linker as well as the piperazinsulfonamid through a methylen group. Instead of the sugar moiety a short polyethylenglycol unit has been added, leading to the generation of Gadofluorine P with favorable kinetics[142]. Taking this into account, we focused on the assessment of Gadofluorine P as a plaque-targeting MR imaging agent in our current imaging approach.

The performed relaxivity measurements showed field strength dependency for Gadofluorine P compared to Gd-DTPA. Decrease of relaxivity at higher field strength

for Gadofluorine P can be explained with changing motion frequency at higher field strength, which is commonly described[167]. Furthermore our results indicate high protein binding of Gadofluorine P, which supports field strength dependency[167].

Quantification of the in vivo imaging signal is a prerequisite for precise analysis of plaque-targeted imaging. In many cases of MR imaging of atherosclerotic plaque in preclinical studies the signal intensity was based on ROI calculation of signal-to-noise ratio or contrast-to-noise ratio rather than pixel-wise parametric maps. These measures are indirect and are determined by imaging parameters (e.g. inversion time, flip angle) and hardware settings (e.g. receiver gain). They are qualitative and do not represent a quantitative analysis. To ensure a semi-quantitative analysis of Gadofluorine P in plaques we applied a T_1-mapping sequence to assess signal enhancement by calculating the T_1 –value for each pixel in the aortic root followed by R_1 calculation[146, 168, 169]. Our results prove that T_1-mapping can be used to detect differences of contrast agent accumulation in our kinetic study as well as in the course of atherosclerosis, different time points of HFD respectively. However, also T_1-mapping is only an approach of quantification and does not correlate to the actual amount of Gadofluorine P contrast agent tissue concentrations because the in vivo signal is determined by the local chemical environment and compartmentalization of the agent. We decided to use atherosclerotic plaques in the aortic root for R_1 relaxation rate analysis because imaging planes, covering the aortic root, were easily positioned in our experimental setup. To select the aortic root, as ROI, is not in accordance with published data: regions of interests were mainly placed in the brachiocephalic artery in mice[111, 118] or the abdominal aorta in rabbits[117, 166]. However, the aortic root provides a reasonable plaque size for ex vivo analysis with MALDI-IMS and thus a comparison from in vivo to ex vivo contrast agent quantification.

Progressive accumulation of Gadofluorine P in atherosclerotic plaques was shown in our study during plaque progression. Due to the chosen ROI in the aortic root, no imaging data for mice without atherosclerosis were acquired. The vascular wall of healthy animals does not allow ROI placement because of its size. The measured increase of R_1 relaxation rate over time can be explained with the presence of lipid-laden foam cells within the plaque as well as continuous extracellular matrix synthesis. Most probably Gadofluorine P accumulates in plaques due to interaction

with lipophilic plaque components and due to adsorption to differently charged proteins or filaments.

Hence, it targets amphiphilic plaque components but not specific cellular structures or specific components. In our experimental setup we did not perform further experiments to elucidate interactions of Gadofluorine P with extracellular matrix components. As already stated in context of relaxivity, Gadofluorine P shows plasma protein binding of more than 90%[142], which supported the described field strength dependency. Gadofluorine M enters plaques bound to albumin[117] concluding possible similar distribution and accumulation of Gadofluorine P.

A challenging task of MRI contrast agents is the precise and quantitative assessment ex vivo following in vivo application. So far either correlations of contrast agent enhancement to plaque size and composition were made or complex technical approaches were used to approve the in vivo signal[116, 117, 141, 166, 170, 171]. A drawback of techniques such as confocal or fluorescence microscopy or radio-active labeled MR agents is the obligatory modification of contrast agents for detection ex vivo, which is challenging as well as labor-intensive and costly. The approach of MALDI-IMS to detect and quantify contrast agents after in vivo MRI offers a solution to these disadvantages. We show for the first time that Gadofluorine P is detected and quantified ex vivo in atherosclerotic plaques with MALDI-IMS following in vivo administration. Our MALDI-IMS quantification is based on calculating a ratio compared to the adjacent myocardium as lesion size was rather small in our study. A minimum size of the analyzed region is necessary because of the resolution of MALDI-IMS (up to 30 µm). Depending on the plaque size a precise quantification is difficult. Nevertheless, the same trend of Gadofluorine P accumulation in atherosclerotic plaques was revealed in our data compared to T_1 shortening observed in vivo by MRI. A correlation between R_1 values of atherosclerotic plaques and Gadofluorine P quantification is furthermore challenging. The slide thickness during MR imaging was 1 mm compared to 12 µm thickness of the slices for MALDI-IMS, which explains that we cannot have a correlation in our study. The actual concentration in vivo is influenced by the biological surrounding, but the quantification ex vivo is based on the plaque in the tissue section. The feasibility of MALDI-IMS to prove contrast agent accumulation was demonstrated, but further improvement is necessary to assess the actual contrast agent concentration.

Barkhausen et al. were the first who quantified gadolinium concentrations in atherosclerotic plaques with inductively coupled plasma mass spectroscopy[122]. Nevertheless, this technique provides no spatial information about contrast agent accumulation due to the fact that vessels with plaques are digested containing gadolinium-based contrast agents[111, 118, 122]. The advantage of our MALDI-IMS approach is the spatially detection of contrast agent accumulation in atherosclerotic plaque. The application of laser ablation-ICP-MS (LA-ICP-MS) is used for quantitative distribution analysis of metals with resolutions up to 5 µm and low limits of detection. This sensitive technology was used to analyze gadolinium concentrations in tumor tissue and brain, for cell tracking experiments[172, 173] as well as manganese accumulation in rat brain[147].
Both quantification methods, LA-ICP-MS and MALDI-IMS, are based on matrix-matched standards or external calibration. An advantage of MALDI-IMS over LA-ICP-IMS is the possibility of spatially quantification of several large biomolecules and not only distribution analysis of elements[123].

In conclusion we describe a non-invasive preclinical imaging approach of atherosclerotic plaques with Gadofluorine P. This contrast agent can be used for imaging and detection of plaques. Tracking of pharmacological interventions to reduce atherosclerosis are therefore possible. In addition, a new ex vivo assessment of MR imaging agent accumulation was applied for the first time in the context of atherosclerosis. MALDI-IMS is feasible to confirm the accumulation of gadolinium-based molecular MR contrast agents in atherosclerotic plaques. Nevertheless, this approach must be further developed to improve the sensitivity for quantification of atherosclerotic plaques by imaging mass spectrometry.

The first and second imaging approach was applied to address biological activity or plaque composition in vivo. The third imaging approach is focused on the application of imaging modalities to create a 3D reconstruction of the murine aortic arch in order to visualize regions of plaque development. The first results of this approach are discussed within the next chapter.

4.3 Application of Imaging Modalities to Create a Three-Dimensional Histological Reconstruction of the Murine Aortic Arch

The application of imaging modalities was used in this third approach to achieve a 3D reconstruction of the murine aortic arch based on serial histological sections. We developed a technical workflow, which considers information about the original geometry of the aortic arch in vivo by adjusting the histological data set to a centerline, which was created after contrast enhanced MR imaging. The achieved 3D reconstructions show similarity to the original shape of the aortic arch, but are limited in regions of bifurcations. Furthermore, µCT was implemented into the development of the workflow to consider shrinkage and deformations, which occur during tissue preparation.

The development of a 3D reconstruction of the murine aortic arch is based on serial histological sections, respectively images. The quality of the vessel on each image is influenced by several factors during the working process as described earlier. We therefore integrated a protocol for standardization and documentation for cutting in our workflow to assure that as many sections as possible are included in the reconstruction process, respectively images. Painstaking standardization and documentation is also described in the literature to achieve 3D reconstruction based on histological images[174]. To reduce data acquisition time at the microscope and for further processing, sections were orientated similarly on the slide as described and discussed by Manconi et al.[129]. Histological reconstruction is based on the alignment of 2D images into a 3D reconstruction. Bussolati et al. described the alignment step as the major problem of reconstruction[135], which we realized in the early phase of our protocol development by creating a reconstructed stack of histological sections. The curvature of the aortic arch is the sticking point for our 3D reconstruction.

To improve alignment we introduced fiducial tissue markers into the paraffin block as described by Bussolati et al.[135]. A possible application in our laboratory was to embed a piece of murine liver close to the aorta in the paraffin block. The liver would serve as reference point for correct alignment. Our approach did not succeed due to the difficulty to section two different kinds of tissue. Furthermore, the presented reconstruction adjusted to the liver did not support reconstruction of the original aortic arch curvature.

A similarity of imaging methods, such as MRI or CT, and histology is that slices are generated with information about anatomy or morphology in the same orientation (transverse plane). A number of published reconstructions included the use of imaging modalities to register histological section to imaging data[130, 131, 136, 138, 139, 175].
In our workflow we decided to conduct contrast enhanced imaging of the aortic arch with MRI to gather information about the vessel geometry. After imaging, segmentation of the vessel lumen was possible to calculate a centerline. Centerline segmentation and calculation is important in clinical applications. The luminal centerline represents the focal point of the vessel, which can be used to quantify length and abnormalities in vessels[176-178].
The centerline matches the curvature of the aortic arch and thus the histological data set can be aligned to it. We applied contrast enhanced imaging of the aortic arch as followed by centerline calculations for two mice. Each histological data set of each murine aortic arch was then registered to the centerline and the 3D reconstruction succeeded. The reconstructed shape is similar to the original shape in vivo. Nevertheless, the reconstruction of the bifurcations showed limitations. Due to the cutting direction in the area of the bifurcations longitudinal sections were generated. In addition, one needs to consider that the bifurcations originate not in the same plane of the aortic arch. In fact, the reconstruction of each bifurcation is even more challenging. As stated earlier correction of primary and secondary deformations is very important to accomplish a realistic reconstruction and reduce inaccuracies. In our protocol the centerline approach is used to correct primary deformations. To gather information about secondary deformations we implemented µCT imaging into our workflow. Micro-CT is a technology, which enables imaging with high resolution and is widely used in tissue engineering to quantify structure-function relationships[179]. This imaging tool produces 2D images, which can be transformed in 3D representations. In a pilot study we imaged successfully paraffin blocks containing the aortic arch by µCT with a high resolution of 2.35 µm/Pixel and reflected information about deformations. This technology would support our workflow by correction of secondary deformations occurring during the sectioning process. In addition a second centerline could be calculated and used for our alignment and 3D reconstruction. Using µCT to gain further information about tissue changes during the histological process for reconstructions were recently published.

They present that reconstructions errors are successfully corrected with supportive µCT data[175, 179, 180].

So far, a reconstruction based on µCT data of the paraffin block to corresponding histological data of the aortic arch was not yet realized, but is likely to succeed.

The integration of imaging modalities supported our protocol development considerable. Further application and implementation is needed to evaluate the workflow with a high number of specimens to identify accuracy and reproducibility.

A limitation of our current workflow is that the development is based on aortic arches of healthy mice. The translation of the protocol to atherosclerotic mice is the next step to fulfill the aim of creating a 3D representation of the aortic arch based on reconstructed histological images to visualize regions of plaque development and regional distribution of different cell types.

5 CONCLUSION

Different approaches of imaging modalities were presented in this work to enhance knowledge about atherosclerosis. The first imaging approach demonstrated tracking of elastase activity in murine atherosclerotic plaques using FMT-XCT to detect early stages of atherosclerosis at a time where the disease is potentially reversible. The second imaging approach investigated the application of Gadofluorine P as plaque-targeting MRI contrast agent. Accumulation of Gadofluorine P within plaques was proven as confirmed with MALDI-IMS ex vivo. Within the third approach two imaging modalities, namely MRI and µCT, supported the development of a workflow for 3D reconstruction of the murine aortic arch based on serial histological sections.

This work highlights that different imaging modalities can be applied to target atherosclerotic lesions in vivo. In addition, targeting specific biological activities or plaque structures may also be amenable for the development of pharmacological interventions. Furthermore, the application of imaging modalities is not only limited to target biological activity. Implementing imaging modalities significantly supported the development of a workflow for a 3D reconstruction of the murine aortic arch.
The combination of targeting pathophysiological processes with high spatial resolution in vivo and the application of 3D histological reconstruction will enable more insights about site-specific development of atherosclerosis, which could be included in a multiscale model of atherosclerosis. This model could be based on computational simulation and modeling of atherosclerosis. Biological information, assessed with imaging modalities, can be implemented and 3D histological reconstruction can be used as confirmation.

6 REFERENCES

1. Cannon B. Cardiovascular disease: Biochemistry to behaviour. *Nature*. 2013;493:S2-S3
2. Hansson GK. Inflammation, atherosclerosis, and coronary artery disease. *New England Journal of Medicine*. 2005;352:1685-1695
3. Dahlöf B. Cardiovascular disease risk factors: Epidemiology and risk assessment. *The American Journal of Cardiology*. 2010;105:3A-9A
4. Mayerl C, Lukasser M, Sedivy R, Niederegger H, Seiler R, Wick G. Atherosclerosis research from past to present--on the track of two pathologists with opposing views, carl von rokitansky and rudolf virchow. *Virchows Arch*. 2006;449:96-103
5. Finking G, Hanke H. Nikolaj nikolajewitsch anitschkow (1885-1964) established the cholesterol-fed rabbit as a model for atherosclerosis research. *Atherosclerosis*. 1997;135:1-7
6. Ross R, Glomset JA. Atherosclerosis and the arterial smooth muscle cell: Proliferation of smooth muscle is a key event in the genesis of the lesions of atherosclerosis. *Science*. 1973;180:1332-1339
7. Ross R, Glomset JA. The pathogenesis of atherosclerosis (first of two parts). *N Engl J Med*. 1976;295:369-377
8. Ross R, Glomset JA. The pathogenesis of atherosclerosis (second of two parts). *N Engl J Med*. 1976;295:420-425
9. Witztum JL, Steinberg D. Role of oxidized low density lipoprotein in atherogenesis. *J Clin Invest*. 1991;88:1785-1792
10. Weber C, Zernecke A, Libby P. The multifaceted contributions of leukocyte subsets to atherosclerosis: Lessons from mouse models. *Nat Rev Immunol*. 2008;8:802-815
11. Fishman AP. Endothelium: A distributed organ of diverse capabilities. *Ann N Y Acad Sci*. 1982;401:1-8
12. Gimbrone MA, Jr. Culture of vascular endothelium. *Prog Hemost Thromb*. 1976;3:1-28
13. Vane JR, Anggard EE, Botting RM. Regulatory functions of the vascular endothelium. *N Engl J Med*. 1990;323:27-36
14. Topper JN, Gimbrone MA, Jr. Blood flow and vascular gene expression: Fluid shear stress as a modulator of endothelial phenotype. *Mol Med Today*. 1999;5:40-46
15. Li YS, Haga JH, Chien S. Molecular basis of the effects of shear stress on vascular endothelial cells. *J Biomech*. 2005;38:1949-1971
16. Orr AW, Helmke BP, Blackman BR, Schwartz MA. Mechanisms of mechanotransduction. *Dev Cell*. 2006;10:11-20
17. Hahn C, Schwartz MA. Mechanotransduction in vascular physiology and atherogenesis. *Nat Rev Mol Cell Biol*. 2009;10:53-62
18. Glagov S, Zarins C, Giddens DP, Ku DN. Hemodynamics and atherosclerosis. Insights and perspectives gained from studies of human arteries. *Arch Pathol Lab Med*. 1988;112:1018-1031
19. Cornhill JF, Roach MR. A quantitative study of the localization of atherosclerotic lesions in the rabbit aorta. *Atherosclerosis*. 1976;23:489-501
20. Chappell DC, Varner SE, Nerem RM, Medford RM, Alexander RW. Oscillatory shear stress stimulates adhesion molecule expression in cultured human endothelium. *Circ Res*. 1998;82:532-539

21. Cunningham KS, Gotlieb AI. The role of shear stress in the pathogenesis of atherosclerosis. *Lab Invest*. 2005;85:9-23
22. Ross R. Atherosclerosis is an inflammatory disease. *Am Heart J*. 1999;138:S419-420
23. Elshourbagy NA, Meyers HV, Abdel-Meguid SS. Cholesterol: The good, the bad, and the ugly - therapeutic targets for the treatment of dyslipidemia. *Med Princ Pract*. 2014;23:99-111
24. Mahley RW, Huang Y. Apolipoprotein e: From atherosclerosis to alzheimer's disease and beyond. *Curr Opin Lipidol*. 1999;10:207-217
25. Navab M, Berliner JA, Watson AD, Hama SY, Territo MC, Lusis AJ, Shih DM, Van Lenten BJ, Frank JS, Demer LL, Edwards PA, Fogelman AM. The yin and yang of oxidation in the development of the fatty streak. A review based on the 1994 george lyman duff memorial lecture. *Arterioscler Thromb Vasc Biol*. 1996;16:831-842
26. Weber C, Noels H. Atherosclerosis: Current pathogenesis and therapeutic options. *Nat Med*. 2011;17:1410-1422
27. Ait-Oufella H, Sage AP, Mallat Z, Tedgui A. Adaptive (t and b cells) immunity and control by dendritic cells in atherosclerosis. *Circ Res*. 2014;114:1640-1660
28. Hansson GK, Libby P, Schonbeck U, Yan ZQ. Innate and adaptive immunity in the pathogenesis of atherosclerosis. *Circ Res*. 2002;91:281-291
29. Hilgendorf I, Swirski FK, Robbins CS. Monocyte fate in atherosclerosis. *Arterioscler Thromb Vasc Biol*. 2015;35:272-279
30. Jonasson L, Holm J, Skalli O, Bondjers G, Hansson GK. Regional accumulations of t cells, macrophages, and smooth muscle cells in the human atherosclerotic plaque. *Arteriosclerosis*. 1986;6:131-138
31. Hansson GK, Libby P. The immune response in atherosclerosis: A double-edged sword. *Nat Rev Immunol*. 2006;6:508-519
32. Yona S, Jung S. Monocytes: Subsets, origins, fates and functions. *Curr Opin Hematol*. 2010;17:53-59
33. Watanabe T, Hirata M, Yoshikawa Y, Nagafuchi Y, Toyoshima H, Watanabe T. Role of macrophages in atherosclerosis. Sequential observations of cholesterol-induced rabbit aortic lesion by the immunoperoxidase technique using monoclonal antimacrophage antibody. *Lab Invest*. 1985;53:80-90
34. Gown AM, Tsukada T, Ross R. Human atherosclerosis. Ii. Immunocytochemical analysis of the cellular composition of human atherosclerotic lesions. *Am J Pathol*. 1986;125:191-207
35. Averill LE, Meagher RC, Gerrity RG. Enhanced monocyte progenitor cell proliferation in bone marrow of hyperlipemic swine. *Am J Pathol*. 1989;135:369-377
36. Murphy AJ, Akhtari M, Tolani S, Pagler T, Bijl N, Kuo CL, Wang M, Sanson M, Abramowicz S, Welch C, Bochem AE, Kuivenhoven JA, Yvan-Charvet L, Tall AR. Apoe regulates hematopoietic stem cell proliferation, monocytosis, and monocyte accumulation in atherosclerotic lesions in mice. *J Clin Invest*. 2011;121:4138-4149
37. Swirski FK, Nahrendorf M, Etzrodt M, Wildgruber M, Cortez-Retamozo V, Panizzi P, Figueiredo JL, Kohler RH, Chudnovskiy A, Waterman P, Aikawa E, Mempel TR, Libby P, Weissleder R, Pittet MJ. Identification of splenic reservoir monocytes and their deployment to inflammatory sites. *Science*. 2009;325:612-616

38. Nakashima Y, Raines EW, Plump AS, Breslow JL, Ross R. Upregulation of vcam-1 and icam-1 at atherosclerosis-prone sites on the endothelium in the apoe-deficient mouse. *Arterioscler Thromb Vasc Biol*. 1998;18:842-851
39. Collins RG, Velji R, Guevara NV, Hicks MJ, Chan L, Beaudet AL. P-selectin or intercellular adhesion molecule (icam)-1 deficiency substantially protects against atherosclerosis in apolipoprotein e-deficient mice. *J Exp Med*. 2000;191:189-194
40. Gerhardt T, Ley K. Monocyte trafficking across the vessel wall. *Cardiovasc Res*. 2015;107:321-330
41. Soehnlein O, Drechsler M, Doring Y, Lievens D, Hartwig H, Kemmerich K, Ortega-Gomez A, Mandl M, Vijayan S, Projahn D, Garlichs CD, Koenen RR, Hristov M, Lutgens E, Zernecke A, Weber C. Distinct functions of chemokine receptor axes in the atherogenic mobilization and recruitment of classical monocytes. *EMBO Mol Med*. 2013;5:471-481
42. Hansson GK. Immune mechanisms in atherosclerosis. *Arterioscler Thromb Vasc Biol*. 2001;21:1876-1890
43. Libby P. Collagenases and cracks in the plaque. *J Clin Invest*. 2013;123:3201-3203
44. Zernecke A, Shagdarsuren E, Weber C. Chemokines in atherosclerosis: An update. *Arterioscler Thromb Vasc Biol*. 2008;28:1897-1908
45. Zernecke A, Weber C. Inflammatory mediators in atherosclerotic vascular disease. *Basic Res Cardiol*. 2005;100:93-101
46. van Leeuwen M, Gijbels MJJ, Duijvestijn A, Smook M, van de Gaar MJ, Heeringa P, de Winther MPJ, Tervaert JWC. Accumulation of myeloperoxidase-positive neutrophils in atherosclerotic lesions in ldlr−/− mice. *Arteriosclerosis, Thrombosis, and Vascular Biology*. 2008;28:84-89
47. Zernecke A, Bot I, Djalali-Talab Y, Shagdarsuren E, Bidzhekov K, Meiler S, Krohn R, Schober A, Sperandio M, Soehnlein O, Bornemann J, Tacke F, Biessen EA, Weber C. Protective role of cxc receptor 4/cxc ligand 12 unveils the importance of neutrophils in atherosclerosis. *Circulation Research*. 2008;102:209-217
48. Naruko T, Ueda M, Haze K, van der Wal AC, van der Loos CM, Itoh A, Komatsu R, Ikura Y, Ogami M, Shimada Y, Ehara S, Yoshiyama M, Takeuchi K, Yoshikawa J, Becker AE. Neutrophil infiltration of culprit lesions in acute coronary syndromes. *Circulation*. 2002;106:2894-2900
49. Rotzius P, Thams S, Soehnlein O, Kenne E, Tseng C-N, Björkström NK, Malmberg K-J, Lindbom L, Eriksson EE. Distinct infiltration of neutrophils in lesion shoulders in apoe−/− mice. *The American Journal of Pathology*. 2010;177:493-500
50. Nathan C. Neutrophils and immunity: Challenges and opportunities. *Nat Rev Immunol*. 2006;6:173-182
51. Eades-Perner A-M, Thompson J, van der Putten H, Zimmermann W. Mice transgenic for the human cgm6 gene express its product, the granulocyte marker cd66b, exclusively in granulocytes. *Blood*. 1998;91:663-672
52. Ionita MG, van den Borne P, Catanzariti LM, Moll FL, de Vries J-PPM, Pasterkamp G, Vink A, de Kleijn DPV. High neutrophil numbers in human carotid atherosclerotic plaques are associated with characteristics of rupture-prone lesions. *Arteriosclerosis, Thrombosis, and Vascular Biology*. 2010;30:1842-1848

53. Daley JM, Thomay AA, Connolly MD, Reichner JS, Albina JE. Use of ly6g-specific monoclonal antibody to deplete neutrophils in mice. *Journal of Leukocyte Biology*. 2008;83:64-70
54. Galli SJ, Borregaard N, Wynn TA. Phenotypic and functional plasticity of cells of innate immunity: Macrophages, mast cells and neutrophils. *Nat Immunol*. 2011;12:1035-1044
55. Soehnlein O, Zernecke A, Eriksson EE, Rothfuchs AG, Pham CT, Herwald H, Bidzhekov K, Rottenberg ME, Weber C, Lindbom L. Neutrophil secretion products pave the way for inflammatory monocytes. *Blood*. 2008;112:1461-1471
56. Drechsler M, Megens RTA, van Zandvoort M, Weber C, Soehnlein O. Hyperlipidemia-triggered neutrophilia promotes early atherosclerosis. *Circulation*. 2010;122:1837-1845
57. o Hartaigh B, Bosch JA, Thomas GN, Lord JM, Pilz S, Loerbroks A, Kleber ME, Grammer TB, Fischer JE, Boehm BO, Marz W. Which leukocyte subsets predict cardiovascular mortality? From the ludwigshafen risk and cardiovascular health (luric) study. *Atherosclerosis*. 2012;224:161-169
58. Hartwig H, Silvestre Roig C, Daemen M, Lutgens E, Soehnlein O. Neutrophils in atherosclerosis. A brief overview. *Hämostaseologie*. 2015;35:121-127
59. Drechsler M, Doring Y, Megens RT, Soehnlein O. Neutrophilic granulocytes - promiscuous accelerators of atherosclerosis. *Thromb Haemost*. 2011;106:839-848
60. Drechsler M, Soehnlein O. The complexity of arterial classical monocyte recruitment. *J Innate Immun*. 2013;5:358-366
61. Pham CTN. Neutrophil serine proteases: Specific regulators of inflammation. *Nat Rev Immunol*. 2006;6:541-550
62. Soehnlein O, Weber C, Lindbom L. Neutrophil granule proteins tune monocytic cell function. *Trends Immunol*. 2009;30:538-546
63. Lee TD, Gonzalez ML, Kumar P, Chary-Reddy S, Grammas P, Pereira HA. Cap37, a novel inflammatory mediator: Its expression in endothelial cells and localization to atherosclerotic lesions. *Am J Pathol*. 2002;160:841-848
64. Barnathan ES, Raghunath PN, Tomaszewski JE, Ganz T, Cines DB, Higazi Aa-R. Immunohistochemical localization of defensin in human coronary vessels. *Am J Pathol*. 1997;150:1009-1020
65. Edfeldt K, Agerberth B, Rottenberg ME, Gudmundsson GH, Wang XB, Mandal K, Xu Q, Yan ZQ. Involvement of the antimicrobial peptide ll-37 in human atherosclerosis. *Arterioscler Thromb Vasc Biol*. 2006;26:1551-1557
66. Hemdahl AL, Gabrielsen A, Zhu C, Eriksson P, Hedin U, Kastrup J, Thoren P, Hansson GK. Expression of neutrophil gelatinase-associated lipocalin in atherosclerosis and myocardial infarction. *Arterioscler Thromb Vasc Biol*. 2006;26:136-142
67. Soehnlein O. Multiple roles for neutrophils in atherosclerosis. *Circulation Research*. 2012;110:875-888
68. Papayannopoulos V, Metzler KD, Hakkim A, Zychlinsky A. Neutrophil elastase and myeloperoxidase regulate the formation of neutrophil extracellular traps. *The Journal of Cell Biology*. 2010;191:677-691
69. Kolaczkowska E, Kubes P. Neutrophil recruitment and function in health and inflammation. *Nat Rev Immunol*. 2013;13:159-175
70. Megens RTA, Vijayan S, Lievens D, Dˆring Y, van Zandvoort MAMJ, Grommes J, Weber C, Soehnlein O. Presence of luminal neutrophil

extracellular traps in atherosclerosis. *Thrombosis and Haemostasis*. 2012;107:597-598
71. Doring Y, Manthey HD, Drechsler M, Lievens D, Megens RT, Soehnlein O, Busch M, Manca M, Koenen RR, Pelisek J, Daemen MJ, Lutgens E, Zenke M, Binder CJ, Weber C, Zernecke A. Auto-antigenic protein-DNA complexes stimulate plasmacytoid dendritic cells to promote atherosclerosis. *Circulation*. 2012;125:1673-1683
72. Warnatsch A, Ioannou M, Wang Q, Papayannopoulos V. Neutrophil extracellular traps license macrophages for cytokine production in atherosclerosis. *Science*. 2015;349:316-320
73. Quillard T, Araujo HA, Franck G, Shvartz E, Sukhova G, Libby P. Tlr2 and neutrophils potentiate endothelial stress, apoptosis and detachment: Implications for superficial erosion. *Eur Heart J*. 2015;36:1394-1404
74. Nahrendorf M, Swirski FK. Neutrophil-macrophage communication in inflammation and atherosclerosis. *Science*. 2015;349:237-238
75. Bocan TM. Animal models of atherosclerosis and interpretation of drug intervention studies. *Curr Pharm Des*. 1998;4:37-52
76. Zhang SH, Reddick RL, Piedrahita JA, Maeda N. Spontaneous hypercholesterolemia and arterial lesions in mice lacking apolipoprotein e. *Science*. 1992;258:468-471
77. Plump AS, Smith JD, Hayek T, Aalto-Setala K, Walsh A, Verstuyft JG, Rubin EM, Breslow JL. Severe hypercholesterolemia and atherosclerosis in apolipoprotein e-deficient mice created by homologous recombination in es cells. *Cell*. 1992;71:343-353
78. Ishibashi S, Goldstein JL, Brown MS, Herz J, Burns DK. Massive xanthomatosis and atherosclerosis in cholesterol-fed low density lipoprotein receptor-negative mice. *J Clin Invest*. 1994;93:1885-1893
79. Getz GS, Reardon CA. Use of mouse models in atherosclerosis research. In: Andrés V, Dorado B, eds. *Methods in mouse atherosclerosis*. New York, NY: Springer New York; 2015:1-16.
80. Paigen B, Morrow A, Brandon C, Mitchell D, Holmes P. Variation in susceptibility to atherosclerosis among inbred strains of mice. *Atherosclerosis*.57:65-73
81. Suo J, Ferrara DE, Sorescu D, Guldberg RE, Taylor WR, Giddens DP. Hemodynamic shear stresses in mouse aortas: Implications for atherogenesis. *Arterioscler Thromb Vasc Biol*. 2007;27:346-351
82. Rosenfeld ME, Carson KG, Johnson JL, Williams H, Jackson CL, Schwartz SM. Animal models of spontaneous plaque rupture: The holy grail of experimental atherosclerosis research. *Curr Atheroscler Rep*. 2002;4:238-242
83. Hermann S, Kuhlmann MT, Starsichova A, Eligehausen S, Schafers K, Stypmann J, Tiemann K, Levkau B, Schafers M. Imaging reveals the connection between spontaneous coronary plaque ruptures, atherothrombosis, and myocardial infarctions in hypoe/srbi-/- mice. *J Nucl Med*. 2016;57:1420-1427
84. Wouters K, Shiri-Sverdlov R, van Gorp PJ, van Bilsen M, Hofker MH. Understanding hyperlipidemia and atherosclerosis: Lessons from genetically modified apoe and ldlr mice. *Clin Chem Lab Med*. 2005;43:470-479
85. James ML, Gambhir SS. A molecular imaging primer: Modalities, imaging agents, and applications. *Physiol Rev*. 2012;92:897-965
86. Wildgruber M, Swirski FK, Zernecke A. Molecular imaging of inflammation in atherosclerosis. *Theranostics*. 2013;3:865-884

87. Quillard T, Libby P. Molecular imaging of atherosclerosis for improving diagnostic and therapeutic development. *Circ Res*. 2012;111:231-244
88. Hyafil F, Cornily JC, Feig JE, Gordon R, Vucic E, Amirbekian V, Fisher EA, Fuster V, Feldman LJ, Fayad ZA. Noninvasive detection of macrophages using a nanoparticulate contrast agent for computed tomography. *Nat Med*. 2007;13:636-641
89. Ntziachristos V, Bremer C, Weissleder R. Fluorescence imaging with near-infrared light: New technological advances that enable in vivo molecular imaging. *Eur Radiol*. 2003;13:195-208
90. Ale A, Ermolayev V, Herzog E, Cohrs C, de Angelis MH, Ntziachristos V. Fmt-xct: In vivo animal studies with hybrid fluorescence molecular tomography-x-ray computed tomography. *Nat Meth*. 2012;9:615-620
91. Nahrendorf M, Waterman P, Thurber G, Groves K, Rajopadhye M, Panizzi P, Marinelli B, Aikawa E, Pittet MJ, Swirski FK, Weissleder R. Hybrid in vivo fmt-ct imaging of protease activity in atherosclerosis with customized nanosensors. *Arteriosclerosis, Thrombosis, and Vascular Biology*. 2009;29:1444-1451
92. Ale A, Schulz RB, Sarantopoulos A, Ntziachristos V. Imaging performance of a hybrid x-ray computed tomography-fluorescence molecular tomography system using priors. *Med Phys*. 2010;37:1976-1986
93. Schulz RB, Ale A, Sarantopoulos A, Freyer M, Soehngen E, Zientkowska M, Ntziachristos V. Hybrid system for simultaneous fluorescence and x-ray computed tomography. *IEEE Trans Med Imaging*. 2010;29:465-473
94. Ntziachristos V. Fluorescence molecular imaging. *Annu Rev Biomed Eng*. 2006;8:1-33
95. Neefjes J, Dantuma NP. Fluorescent probes for proteolysis: Tools for drug discovery. *Nat Rev Drug Discov*. 2004;3:58-69
96. Lin S-A, Patel M, Suresch D, Connolly B, Bao B, Groves K, Rajopadhye M, Peterson JD, Klimas M, Sur C, Bednar B. Quantitative longitudinal imaging of vascular inflammation and treatment by ezetimibe in apoe mice by fmt using new optical imaging biomarkers of cathepsin activity and α(v)β(3) integrin. *International Journal of Molecular Imaging*. 2012;2012:189254
97. Nahrendorf M, Sosnovik DE, Waterman P, Swirski FK, Pande AN, Aikawa E, Figueiredo J-L, Pittet MJ, Weissleder R. Dual channel optical tomographic imaging of leukocyte recruitment and protease activity in the healing myocardial infarct. *Circulation Research*. 2007;100:1218-1225
98. Panizzi P, Swirski FK, Figueiredo JL, Waterman P, Sosnovik DE, Aikawa E, Libby P, Pittet M, Weissleder R, Nahrendorf M. Impaired infarct healing in atherosclerotic mice with ly-6c(hi) monocytosis. *J Am Coll Cardiol*. 2010;55:1629-1638
99. Deguchi JO, Aikawa M, Tung CH, Aikawa E, Kim DE, Ntziachristos V, Weissleder R, Libby P. Inflammation in atherosclerosis: Visualizing matrix metalloproteinase action in macrophages in vivo. *Circulation*. 2006;114:55-62
100. Chen J, Tung CH, Mahmood U, Ntziachristos V, Gyurko R, Fishman MC, Huang PL, Weissleder R. In vivo imaging of proteolytic activity in atherosclerosis. *Circulation*. 2002;105:2766-2771
101. Kim DE, Kim JY, Schellingerhout D, Shon SM, Jeong SW, Kim EJ, Kim WK. Molecular imaging of cathepsin b proteolytic enzyme activity reflects the inflammatory component of atherosclerotic pathology and can quantitatively demonstrate the antiatherosclerotic therapeutic effects of atorvastatin and glucosamine. *Mol Imaging*. 2009;8:291-301

102. Jaffer FA, Kim DE, Quinti L, Tung CH, Aikawa E, Pande AN, Kohler RH, Shi GP, Libby P, Weissleder R. Optical visualization of cathepsin k activity in atherosclerosis with a novel, protease-activatable fluorescence sensor. *Circulation*. 2007;115:2292-2298
103. Wallis de Vries BM, Hillebrands JL, van Dam GM, Tio RA, de Jong JS, Slart RH, Zeebregts CJ. Images in cardiovascular medicine. Multispectral near-infrared fluorescence molecular imaging of matrix metalloproteinases in a human carotid plaque using a matrix-degrading metalloproteinase-sensitive activatable fluorescent probe. *Circulation*. 2009;119:e534-536
104. Sarantopoulos A, Themelis G, Ntziachristos V. Imaging the bio-distribution of fluorescent probes using multispectral epi-illumination cryoslicing imaging. *Mol Imaging Biol*. 2011;13:874-885
105. Sosnovik DE, Weissleder R. Emerging concepts in molecular mri. *Curr Opin Biotechnol*. 2007;18:4-10
106. Phinikaridou A, Andia M, Lacerda S, Lorrio S, Makowski M, Botnar R. Molecular mri of atherosclerosis. *Molecules*. 2013;18:14042
107. Caravan P, Ellison JJ, McMurry TJ, Lauffer RB. Gadolinium(iii) chelates as mri contrast agents: Structure, dynamics, and applications. *Chem Rev*. 1999;99:2293-2352
108. Weissleder R, Elizondo G, Wittenberg J, Rabito CA, Bengele HH, Josephson L. Ultrasmall superparamagnetic iron oxide: Characterization of a new class of contrast agents for mr imaging. *Radiology*. 1990;175:489-493
109. Small WC, Nelson RC, Bernardino ME. Dual contrast enhancement of both t1- and t2-weighted sequences using ultrasmall superparamagnetic iron oxide. *Magn Reson Imaging*. 1993;11:645-654
110. McAteer MA, Schneider JE, Ali ZA, Warrick N, Bursill CA, von zur Muhlen C, Greaves DR, Neubauer S, Channon KM, Choudhury RP. Magnetic resonance imaging of endothelial adhesion molecules in mouse atherosclerosis using dual-targeted microparticles of iron oxide. *Arterioscler Thromb Vasc Biol*. 2008;28:77-83
111. Phinikaridou A, Andia ME, Protti A, Indermuehle A, Shah A, Smith A, Warley A, Botnar RM. Noninvasive magnetic resonance imaging evaluation of endothelial permeability in murine atherosclerosis using an albumin-binding contrast agent. *Circulation*. 2012;126:707-719
112. Lobbes MB, Heeneman S, Passos VL, Welten R, Kwee RM, van der Geest RJ, Wiethoff AJ, Caravan P, Misselwitz B, Daemen MJ, van Engelshoven JM, Leiner T, Kooi ME. Gadofosveset-enhanced magnetic resonance imaging of human carotid atherosclerotic plaques: A proof-of-concept study. *Invest Radiol*. 2010;45:275-281
113. Kooi ME, Cappendijk VC, Cleutjens KB, Kessels AG, Kitslaar PJ, Borgers M, Frederik PM, Daemen MJ, van Engelshoven JM. Accumulation of ultrasmall superparamagnetic particles of iron oxide in human atherosclerotic plaques can be detected by in vivo magnetic resonance imaging. *Circulation*. 2003;107:2453-2458
114. Ruehm SG, Corot C, Vogt P, Kolb S, Debatin JF. Magnetic resonance imaging of atherosclerotic plaque with ultrasmall superparamagnetic particles of iron oxide in hyperlipidemic rabbits. *Circulation*. 2001;103:415-422
115. Amirbekian V, Lipinski MJ, Briley-Saebo KC, Amirbekian S, Aguinaldo JG, Weinreb DB, Vucic E, Frias JC, Hyafil F, Mani V, Fisher EA, Fayad ZA. Detecting and assessing macrophages in vivo to evaluate atherosclerosis

noninvasively using molecular mri. *Proc Natl Acad Sci U S A*. 2007;104:961-966
116. Sirol M, Itskovich VV, Mani V, Aguinaldo JG, Fallon JT, Misselwitz B, Weinmann HJ, Fuster V, Toussaint JF, Fayad ZA. Lipid-rich atherosclerotic plaques detected by gadofluorine-enhanced in vivo magnetic resonance imaging. *Circulation*. 2004;109:2890-2896
117. Meding J, Urich M, Licha K, Reinhardt M, Misselwitz B, Fayad ZA, Weinmann H-J. Magnetic resonance imaging of atherosclerosis by targeting extracellular matrix deposition with gadofluorine m. *Contrast Media & Molecular Imaging*. 2007;2:120-129
118. Makowski MR, Wiethoff AJ, Blume U, Cuello F, Warley A, Jansen CHP, Nagel E, Razavi R, Onthank DC, Cesati RR, Marber MS, Schaeffter T, Smith A, Robinson SP, Botnar RM. Assessment of atherosclerotic plaque burden with an elastin-specific magnetic resonance contrast agent. *Nat Med*. 2011;17:383-388
119. Lancelot E, Amirbekian V, Brigger I, Raynaud JS, Ballet S, David C, Rousseaux O, Le Greneur S, Port M, Lijnen HR, Bruneval P, Michel JB, Ouimet T, Roques B, Amirbekian S, Hyafil F, Vucic E, Aguinaldo JG, Corot C, Fayad ZA. Evaluation of matrix metalloproteinases in atherosclerosis using a novel noninvasive imaging approach. *Arterioscler Thromb Vasc Biol*. 2008;28:425-432
120. Hyafil F, Vucic E, Cornily JC, Sharma R, Amirbekian V, Blackwell F, Lancelot E, Corot C, Fuster V, Galis ZS, Feldman LJ, Fayad ZA. Monitoring of arterial wall remodelling in atherosclerotic rabbits with a magnetic resonance imaging contrast agent binding to matrix metalloproteinases. *Eur Heart J*. 2011;32:1561-1571
121. Aichler M, Huber K, Schilling F, Lohofer F, Kosanke K, Meier R, Rummeny EJ, Walch A, Wildgruber M. Spatially resolved quantification of gadolinium(iii)-based magnetic resonance agents in tissue by maldi imaging mass spectrometry after in vivo mri. *Angew Chem Int Ed Engl*. 2015;54:4279-4283
122. Barkhausen J, Ebert W, Heyer C, Debatin JF, Weinmann HJ. Detection of atherosclerotic plaque with gadofluorine-enhanced magnetic resonance imaging. *Circulation*. 2003;108:605-609
123. Becker JS, Zoriy M, Matusch A, Wu B, Salber D, Palm C, Becker JS. Bioimaging of metals by laser ablation inductively coupled plasma mass spectrometry (la-icp-ms). *Mass Spectrom Rev*. 2010;29:156-175
124. Norris JL, Caprioli RM. Imaging mass spectrometry: A new tool for pathology in a molecular age. *Proteomics Clin Appl*. 2013;7:733-738
125. Acquadro E, Cabella C, Ghiani S, Miragoli L, Bucci EM, Corpillo D. Matrix-assisted laser desorption ionization imaging mass spectrometry detection of a magnetic resonance imaging contrast agent in mouse liver. *Anal Chem*. 2009;81:2779-2784
126. Follain G, Mercier L, Osmani N, Harlepp S, Goetz JG. Seeing is believing: Multi-scale spatio-temporal imaging towards in vivo cell biology. *J Cell Sci*. 2016
127. Wang Y, Xu R, Luo G, Wu J. Three-dimensional reconstruction of light microscopy image sections: Present and future. *Front Med*. 2015;9:30-45
128. Roberts N, Magee D, Song Y, Brabazon K, Shires M, Crellin D, Orsi NM, Quirke R, Quirke P, Treanor D. Toward routine use of 3d histopathology as a research tool. *The American Journal of Pathology*. 2012;180:1835-1842

129. Manconi F, Markham R, Cox G, Kable E, Fraser IS. Computer-generated, three-dimensional reconstruction of histological parallel serial sections displaying microvascular and glandular structures in human endometrium. *Micron*. 2001;32:449-453
130. Dauguet J, Delzescaux T, Condé F, Mangin J-F, Ayache N, Hantraye P, Frouin V. Three-dimensional reconstruction of stained histological slices and 3d non-linear registration with in-vivo mri for whole baboon brain. *Journal of Neuroscience Methods*. 2007;164:191-204
131. Malandain G, Bardinet E, Nelissen K, Vanduffel W. Fusion of autoradiographs with an mr volume using 2-d and 3-d linear transformations. *Neuroimage*. 2004;23:111-127
132. Cifor A, Bai L, Pitiot A. Smoothness-guided 3-d reconstruction of 2-d histological images. *NeuroImage*. 2011;56:197-211
133. Feuerstein M, Heibel H, Gardiazabal J, Navab N, Groher M. Reconstruction of 3-d histology images by simultaneous deformable registration. In: Fichtinger G, Martel A, Peters T, eds. *Medical image computing and computer-assisted intervention – miccai 2011: 14th international conference, toronto, canada, september 18-22, 2011, proceedings, part ii*. Berlin, Heidelberg: Springer Berlin Heidelberg; 2011:582-589.
134. Ourselin S, Roche A, Subsol G, Pennec X, Ayache N. Reconstructing a 3d structure from serial histological sections. *Image and Vision Computing*. 2001;19:25-31
135. Bussolati G, Marchiò C, Volante M. Tissue arrays as fiducial markers for section alignment in 3-d reconstruction technology. *Journal of Cellular and Molecular Medicine*. 2005;9:438-445
136. Yelnik J, Bardinet E, Dormont D, Malandain G, Ourselin S, Tande D, Karachi C, Ayache N, Cornu P, Agid Y. A three-dimensional, histological and deformable atlas of the human basal ganglia. I. Atlas construction based on immunohistochemical and mri data. *Neuroimage*. 2007;34:618-638
137. Gefen S, Kiryati N, Nissanov J. Atlas-based indexing of brain sections via 2-d to 3-d image registration. *IEEE Trans Biomed Eng*. 2008;55:147-156
138. Stille M, Smith EJ, Crum WR, Modo M. 3d reconstruction of 2d fluorescence histology images and registration with in vivo mr images: Application in a rodent stroke model. *Journal of Neuroscience Methods*. 2013;219:27-40
139. Groen HC, van Walsum T, Rozie S, Klein S, van Gaalen K, Gijsen FJH, Wielopolski PA, van Beusekom HMM, de Crom R, Verhagen HJM, van der Steen AFW, van der Lugt A, Wentzel JJ, Niessen WJ. Three-dimensional registration of histology of human atherosclerotic carotid plaques to in-vivo imaging. *Journal of Biomechanics*. 2010;43:2087-2092
140. Kossodo S, Zhang J, Groves K, Cuneo GJ, Handy E, Morin J, Delaney J, Yared W, Rajopadhye M, Peterson JD. Noninvasive in vivo quantification of neutrophil elastase activity in acute experimental mouse lung injury. *Int J Mol Imaging*. 2011;2011:581406
141. Ronald JA, Chen Y, Belisle AJ-L, Hamilton AM, Rogers KA, Hegele RA, Misselwitz B, Rutt BK. Comparison of gadofluorine-m and gd-dtpa for noninvasive staging of atherosclerotic plaque stability using mri. *Circulation: Cardiovascular Imaging*. 2009;2:226-234
142. Sheng F, Inoue Y, Kiryu S, Watanabe M, Ohtomo K. Long-term assessment of contrast effects of gadofluorine m and gadofluorine p in magnetic resonance imaging of mice. *Japanese Journal of Radiology*. 2012;30:86-91

143. Messroghli DR, Rudolph A, Abdel-Aty H, Wassmuth R, Kuhne T, Dietz R, Schulz-Menger J. An open-source software tool for the generation of relaxation time maps in magnetic resonance imaging. *BMC Med Imaging*. 2010;10:16
144. Deichmann R, Hahn D, Haase A. Fast t1 mapping on a whole-body scanner. *Magn Reson Med*. 1999;42:206-209
145. Paige CC, Saunders MA. Lsqr: An algorithm for sparse linear equations and sparse least squares. *ACM Trans. Math. Softw.* 1982;8:43-71
146. Baxa J, Ferda J, Hromadka M. T1 mapping of the ischemic myocardium: Review of potential clinical use. *Eur J Radiol*. 2016
147. Huber K, Aichler M, Sun N, Buck A, Li Z, Fernandez IE, Hauck SM, Zitzelsberger H, Eickelberg O, Janssen KP, Keller U, Walch A. A rapid ex vivo tissue model for optimising drug detection and ionisation in maldi imaging studies. *Histochem Cell Biol*. 2014;142:361-371
148. Schneider CA, Rasband WS, Eliceiri KW. Nih image to imagej: 25 years of image analysis. *Nat Methods*. 2012;9:671-675
149. Kawabata K, Suzuki M, Sugitani M, Imaki K, Toda M, Miyamoto T. Ono-5046, a novel inhibitor of human neutrophil elastase. *Biochemical and Biophysical Research Communications*. 1991;177:814-820
150. Glinzer A, Ma X, Prakash J, Kimm MA, Lohofer F, Kosanke K, Pelisek J, Thon MP, Vorlova S, Heinze KG, Eckstein HH, Gee MW, Ntziachristos V, Zernecke A, Wildgruber M. Targeting elastase for molecular imaging of early atherosclerotic lesions. *Arterioscler Thromb Vasc Biol*. 2017;37:525-533
151. Zeiher BG, Matsuoka S, Kawabata K, Repine JE. Neutrophil elastase and acute lung injury: Prospects for sivelestat and other neutrophil elastase inhibitors as therapeutics. *Crit Care Med*. 2002;30:S281-287
152. von Nussbaum F, Li VM. Neutrophil elastase inhibitors for the treatment of (cardio)pulmonary diseases: Into clinical testing with pre-adaptive pharmacophores. *Bioorg Med Chem Lett*. 2015;25:4370-4381
153. Worthen GS, Avdi N, Buhl AM, Suzuki N, Johnson GL. Fmlp activates ras and raf in human neutrophils. Potential role in activation of map kinase. *J Clin Invest*. 1994;94:815-823
154. Wiesner O, Litwiller RD, Hummel AM, Viss MA, McDonald CJ, Jenne DE, Fass DN, Specks U. Differences between human proteinase 3 and neutrophil elastase and their murine homologues are relevant for murine model experiments. *FEBS Lett*. 2005;579:5305-5312
155. Mitra S, Modi KD, Foster TH. Enzyme-activatable imaging probe reveals enhanced neutrophil elastase activity in tumors following photodynamic therapy. *BIOMEDO*. 2013;18:101314-101314
156. Patel M, Lin S-A, Boddicker MA, DeMaula C, Connolly B, Bednar B, Heinrichs JH, Smith JG. Quantitative in vivo detection of chlamydia muridarum associated inflammation in a mouse model using optical imaging. *Mediators of Inflammation*. 2015;2015:264897
157. Simon RA, John CS. Optical tomography: Forward and inverse problems. *Inverse Problems*. 2009;25:123010
158. Zhang G, Liu F, Zhang B, He Y, Luo J, Bai J. Imaging of pharmacokinetic rates of indocyanine green in mouse liver with a hybrid fluorescence molecular tomography/x-ray computed tomography system. *J Biomed Opt*. 2013;18:040505

159. Haller J, Hyde D, Deliolanis N, de Kleine R, Niedre M, Ntziachristos V. Visualization of pulmonary inflammation using noninvasive fluorescence molecular imaging. *J Appl Physiol (1985)*. 2008;104:795-802
160. Alfaidi M, Wilson H, Daigneault M, Burnett A, Ridger V, Chamberlain J, Francis S. Neutrophil elastase promotes interleukin-1beta secretion from human coronary endothelium. *J Biol Chem*. 2015;290:24067-24078
161. Dollery CM, Owen CA, Sukhova GK, Krettek A, Shapiro SD, Libby P. Neutrophil elastase in human atherosclerotic plaques: Production by macrophages. *Circulation*. 2003;107:2829-2836
162. Song J, Tan H, Perry AJ, Akutsu T, Webb GI, Whisstock JC, Pike RN. Prosper: An integrated feature-based tool for predicting protease substrate cleavage sites. *PLoS ONE*. 2012;7:e50300
163. Zeiher BG, Artigas A, Vincent JL, Dmitrienko A, Jackson K, Thompson BT, Bernard G, Group SS. Neutrophil elastase inhibition in acute lung injury: Results of the strive study. *Crit Care Med*. 2004;32:1695-1702
164. Jaffer FA, Calfon MA, Rosenthal A, Mallas G, Razansky RN, Mauskapf A, Weissleder R, Libby P, Ntziachristos V. Two-dimensional intravascular near-infrared fluorescence molecular imaging of inflammation in atherosclerosis and stent-induced vascular injury. *Journal of the American College of Cardiology*. 2011;57:2516-2526
165. Yoo H, Kim JW, Shishkov M, Namati E, Morse T, Shubochkin R, McCarthy JR, Ntziachristos V, Bouma BE, Jaffer FA, Tearney GJ. Intra-arterial catheter for simultaneous microstructural and molecular imaging in vivo. *Nat Med*. 2011;17:1680-1684
166. Sirol M, Moreno PR, Purushothaman K-R, Vucic E, Amirbekian V, Weinmann H-J, Muntner P, Fuster V, Fayad ZA. Increased neovascularization in advanced lipid-rich atherosclerotic lesions detected by gadofluorine-m-enhanced mri: Implications for plaque vulnerability. *Circulation: Cardiovascular Imaging*. 2009;2:391-396
167. Rohrer M, Bauer H, Mintorovitch J, Requardt M, Weinmann HJ. Comparison of magnetic properties of mri contrast media solutions at different magnetic field strengths. *Invest Radiol*. 2005;40:715-724
168. h-Ici DO, Jeuthe S, Al-Wakeel N, Berger F, Kuehne T, Kozerke S, Messroghli DR. T1 mapping in ischaemic heart disease. *Eur Heart J Cardiovasc Imaging*. 2014;15:597-602
169. Kellman P, Hansen MS. T1-mapping in the heart: Accuracy and precision. *J Cardiovasc Magn Reson*. 2014;16:2
170. Chaabane L, Pellet N, Bourdillon MC, Desbleds Mansard C, Sulaiman A, Hadour G, Thivolet-Bejui F, Roy P, Briguet A, Douek P, Canet Soulas E. Contrast enhancement in atherosclerosis development in a mouse model: In vivo results at 2 tesla. *MAGMA*. 2004;17:188-195
171. Koktzoglou I, Harris KR, Tang R, Kane BJ, Misselwitz B, Weinmann HJ, Lu B, Nagaraj A, Roth SI, Carroll TJ, McPherson DD, Li D. Gadofluorine-enhanced magnetic resonance imaging of carotid atherosclerosis in yucatan miniswine. *Invest Radiol*. 2006;41:299-304
172. Schmidt R, Nippe N, Strobel K, Masthoff M, Reifschneider O, Castelli DD, Holtke C, Aime S, Karst U, Sunderkotter C, Bremer C, Faber C. Highly shifted proton mr imaging: Cell tracking by using direct detection of paramagnetic compounds. *Radiology*. 2014;272:785-795
173. Reifschneider O, Wentker KS, Strobel K, Schmidt R, Masthoff M, Sperling M, Faber C, Karst U. Elemental bioimaging of thulium in mouse tissues by laser

ablation-icpms as a complementary method to heteronuclear proton magnetic resonance imaging for cell tracking experiments. *Anal Chem*. 2015;87:4225-4230
174. Deverell MH, Bailey N, Whimster WF. Tissue distortion in three-dimensional reconstruction of wax or plastic embedded microscopic structures. *Pathol Res Pract*. 1989;185:598-601
175. Schürmann C, Gremse F, Jo H, Kiessling F, Brandes RP. Micro-ct technique is well suited for documentation of remodeling processes in murine carotid arteries. *PLoS ONE*. 2015;10:e0130374
176. Kang DG, Suh DC, Ra JB. Three-dimensional blood vessel quantification via centerline deformation. *IEEE Trans Med Imaging*. 2009;28:405-414
177. Tillich M, Hill BB, Paik DS, Petz K, Napel S, Zarins CK, Rubin GD. Prediction of aortoiliac stent-graft length: Comparison of measurement methods. *Radiology*. 2001;220:475-483
178. Soleimanifard S, Schar M, Hays AG, Weiss RG, Stuber M, Prince JL. Vessel centerline tracking and boundary segmentation in coronary mra with minimal manual interaction. *Proc IEEE Int Symp Biomed Imaging*. 2012:1417-1420
179. Boerckel JD, Mason DE, McDermott AM, Alsberg E. Microcomputed tomography: Approaches and applications in bioengineering. *Stem Cell Res Ther*. 2014;5:144
180. Scott AE, Vasilescu DM, Seal KA, Keyes SD, Mavrogordato MN, Hogg JC, Sinclair I, Warner JA, Hackett TL, Lackie PM. Three dimensional imaging of paraffin embedded human lung tissue samples by micro-computed tomography. *PLoS One*. 2015;10:e0126230

7 ACKNOWLEDGEMENTS

First of all my thanks go to Alma Zernecke, Moritz Wildgruber and Michael Gee for providing me with the opportunity to contribute to this inspiring project. Then I would like to thank Hans-Henning Eckstein for taking over the duty as first advisor and being part in his laboratory of Vascular Biology, at the Department of Vascular and Endovascular Surgery, Klinikum rechts der Isar, Technische Universität München. Also a warm thank you to Hendrik Dietz, my second advisor, who took time and provided my with helpful input throughout my thesis, in particular in our Biomaterials Workshops.

Alma Zernecke – I am very grateful for being your PhD student. Thank you for believing in me and supporting me with constructive comments and advice.

Moritz Wildgruber – thank you for being part of this interdisciplinary project. Your wide knowledge and financial support greatly contributed to my thesis, not to forget your help during my final steps by proof reading.

Jaroslav Pelisek – thank you for discussing data and helping me with trouble shootings. Special thanks go to Renate Hegenloh for her technical assistance along the way and her support.

Fabian Löhofer, Katja Kosanke, Melanie Kimm, Laura Hoffmann and Katharina Huber thank you so much for supporting the MRI imaging project.

To my collaborators, Moritz Thon and Michael Gee, from Mechanics and High Performance Computing Group, thank you for working with me and being an important part of this work.

I would also like to thank Xiaopeng Ma and Java Prakash from Institute of Biological and Medical Imaging for our successful FMT-XCT project.

Last but not least – a warm thank you to Lara Kuntz, Christina Dargel, and Fabian Lohöfer for their help in the final stage by proof reading my thesis.

8 Appendix

8.1 List of Figures

8.2 List of Tables

8.3 List of Publications

Targeting elastase for molecular imaging of early atherosclerotic lesions

Glinzer A, Ma X, Prakash J, Kimm MA, Lohöfer F, Kosanke K, Pelisek J, Thon MP, Vorlova S, Heinze KG, Eckstein HH, Gee MW, Nitziachristos V, Zernecke A, Wildgruber M - Arterioscler Thromb Vasc Biol. 2017 Mar; 37(3):525-533

The "Intermediate" $CD14^{++}CD16^{+}$ monocyte subset increases in severe peripheral artery disease in humans

Wildgruber M, Aschenbrenner T, Wendorff H, Czubba M, **Glinzer A**, Haller B, Schiemann M, Zimmermann A, Berger H, Eckstein HH, Meier R, Wohlgemuth WA, Libby P, Zernecke A - Sci Rep. 2016 Dec 19; 6:39483

Increased intermediate $CD14^{++}CD16^{++}$ monocyte subset levels associate with restenosis after peripheral percutaneous transluminal angioplasty

Wildgruber M, Czubba M, Aschenbrenner T, Wendorff H, Hapfelmeier A, **Glinzer A**, Schiemann M, Zimmermann A, Eckstein HH, Berger H, Wohlgemuth WA, Meier R, Libby P, Zernecke A - Atherosclerosis. 2016 Oct;253:128-134

Multiscale imaging of myocardial remodeling using a combined MR and MALDI imaging approach

Lohoefer F, Hoffmann L, Huber K, **Glinzer A**, Kosanke K, Feuchtinger A, Aichler M, Feuerecker B, Kaissis G, Rummeny EJ, Hoeltke C, Faber C, Schilling F, Botnar R, Walch AK, Wildgruber M - Theranostics, in revision since December 2016

8.4 Poster/Oral Presentations

Etablierung eines 3D-Modells des Aortenbogens der Maus

Glinzer A, Thon M, Pelisek J, Wildgruber M, Eckstein HH, Gee MW, Zernecke A
Poster presentation
30. Jahrestagung der Deutschen Gesellschaft für Gefäßchirurgie und Gefäßmedizin, Hamburg, Germany
24–27. September 2014

Establishment of a 3D model of the murine aortic arch

Glinzer A, Thon M, Pelisek J, Wildgruber M, Eckstein HH, Gee MW, Zernecke A
Poster presentation
4th Munich Aortic and Carotid Conference, Munich, Germany
5–6. December 2014

Development of a 3D-Model of the murine aortic arch

Glinzer A, Thon M, Pelisek J, Wildgruber M, Eckstein HH, Gee MW, Zernecke A
Poster presentation
83rd European Atherosclerosis Society Congress, Glasgow, UK
22–25. March 2015

Molecular imaging of atherosclerosis using the novel magnetic resonance contrast agent Gadofluorine P and T1 mapping techniques

Glinzer A, Lohoefer F, Hoffmann L, Kosanke K, Rummeny EJ, Zernecke A, Schilling F, Wildgruber M
Poster presentation
World Molecular Imaging Congress 2015, Honolulu, USA
2–5. September 2015

Method development of a 3D reconstruction of the murine aortic arch

Glinzer A, Thon M, Lohoefer F, Eckstein HH, Rummeny EJ, Gee MW, Wildgruber M, Zernecke A
Poster presentation
World Molecular Imaging Congress 2015, Honolulu, USA
2–5. September 2015